Measuring and Modeling of Grinding Wheel Topography

by

Abdalslam Darafon

Submitted in partial fulfilment of the requirements
for the degree of Doctor of Philosophy

at

Dalhousie University
Halifax, Nova Scotia
April 2013

DALHOUSIE UNIVERSITY

DEPARTMENT OF MECHANICAL ENGINEERING

The undersigned hereby certify that they have read and recommend to the Faculty of Graduate Studies for acceptance a thesis entitled “Measuring and Modeling of Grinding Wheel Topography” by Abdalslam Darafon in partial fulfilment of the requirements for the degree of Doctor of Philosophy.

Dated: April 1, 2013

External Examiner: _____

Research Supervisor: _____

Examining Committee: _____

_____

Departmental Representative: _____

DALHOUSIE UNIVERSITY

DATE: April 1, 2013

AUTHOR: Abdalslam Darafon

TITLE: Measuring and Modeling of Grinding Wheel Topography

DEPARTMENT OR SCHOOL: Department of Mechanical Engineering

DEGREE: PhD CONVOCATION: May YEAR: 2013

Permission is herewith granted to Dalhousie University to circulate and to have copied for non-commercial purposes, at its discretion, the above title upon the request of individuals or institutions. I understand that my thesis will be electronically available to the public.

The author reserves other publication rights, and neither the thesis nor extensive extracts from it may be printed or otherwise reproduced without the author's written permission.

The author attests that permission has been obtained for the use of any copyrighted material appearing in the thesis (other than the brief excerpts requiring only proper acknowledgement in scholarly writing), and that all such use is clearly acknowledged.

_____

Signature of Author

Commitment, effort, and devotion were fundamental elements for the completion of my doctoral dissertation, but even more was the support of my family. I dedicate my dissertation to:

My mother Amina and my late father Tejane, who still lives in my heart. They have been a source of encouragement and inspiration to me throughout my life.

My wife Fadea Alarbi for her unconditional and endless support and compassion in every moment during my studies over twelve years.

My darling children Amal, Eman, Anas and Ehab.

All my brothers, sisters and friends.

Table of contents

List of Tables

List of Figures

Abstract

In this work, measurements and simulations were used to investigate the effects of grinding wheel topography on the geometric aspects of the grinding process. Since existing methods for measuring the grinding wheels were either not accurate enough or could only measure a small portion of a grinding wheel, a novel grinding wheel measurement system was developed. This system consists of a white light chromatic sensor, a custom designed positioning system and software. The resulting wheel scanning system was capable of measuring an entire grinding wheel with micron level accuracy. The system was used to investigate the effects of fine, medium and course dressing on grinding wheel surface topology and the resulting workpiece surface. New techniques were also developed to simulate metal removal in grinding. The simulation software consisted of a stochastic wheel model, dressing model and metal removal model. The resulting software could determine the uncut chip thickness, contact length for every cutting edge on a grinding wheel as well as the resulting surface roughness of the grinding wheel. The simulation was validated by comparing the wheel model used in the simulation to grinding wheel measurements and by comparing the simulated surface finish to the measured surface finish. There was excellent agreement between the predicted and experimentally measured surface topology of the workpiece. The results suggested that only 22 to 30% of the cutting edges exposed on the grinding wheel are active and that the average grinding chip is as much as 10 times thicker and 5 times shorter than would be produced by a grinding wheel with a regular arrangement of cutting edges as assumed by existing analytical approaches.

List of Abbreviations and Symbols Used

Abbreviations

1D	1 Dimension
2D	2 Dimension
3D	3 Dimension
ACEnet	Atlantic Computational Excellence Network
AE	Acoustic Emission
ANSI	American National Standards Institute
CBN	Cubic Boron Nitride
CMM	Coordinates Measuring Machine
CPU	Central processing unit
DC	Depth of Cut
GS	Grain Size
HPC	high-performance computing
MRR	material removal rate
ORAN's	Optical Regional Advanced Networks
RMS	Root Mean Square
SC	Simple Cubic
SEM	Scanning Electron Microscopes
SF	cutting edge Shape Factor
SR	Speed Ratio

Symbols

a	Grinding depth of cut
A	Amplitude
A_2	Empirical constant
A_3	Empirical constant
A_4	Empirical constant
a_d	Dressing depth
A_{gw}	Cutting edge shape constant
A_{int}	Intersection area between the dressing tool path and the grain
a_r	Dressing depth per wheel revolution
$\hat{\alpha}_x$	Random number
$\hat{\alpha}_y$	Random number
$\overline{b_c}$	Average cutting edge width
b_d	Dressing active width
b_p	Pulse width

C	Cutting edge density
C_A	Cutting edge density per unit area
C_{st}	Volumetric static cutting edge density
C_{gr}	Grain concentration
D	Fractal dimension
d_{eq}	Equivalent grain diameter
d_g	Average grain diameter
d_{g_max}	Maximum grains size
d_{g_min}	Minimum grains size
d_{g_mean}	Mean grain diameter
d_h	Height of dressing tool profile
d_s	Grinding wheel diameter
dt_f	Time step factor
d_w	Width of dressing tool profile
f	Length parameter
f_d	Dressing lead
$f(x)$	Grain surface resulting from the diamond dressing path
$P(x)$	Probability of value x
h	Amplitude
H	Minimum surface height
H_b	Bond surface height
h_{dg}	Instantaneous dressing depth of cut
h_i	Protrusion height
H_g	Protrusion height
h_m	Uncut chip thickness
h_{mv}	Vertical uncut chip thickness
i	Index
i	number of exposed grains
j	index
k	Fitted parameter
l	Length
L_p	Profile length
l_c	Contact length
L_{cell}	Length of unit cell
L_r	Arc length
L	Grain inter-spacing
l_k	Kinematic contact length
l_{wp}	Workpiece length

M	Mash number
n	number of grains
N	Number of self-similarity objects
n_1	Fitted parameter
n_2	Fitted parameter
N_a	Number of grains per unit area
N_{av}^{p}	Number of the grains that protrude above the bond level
N_l	Number of the grains per unit length
N_{ls}	Number of line segment
N_{kin}	Kinematic cutting edge density
n_p	Number of samples per pulse
N_p	Number of pulses per wheel revolution
N_{st}	Static cutting edge density
r_p	Scale length
R	Circle radius
r_g	Grain radius
R_g	Distance between the grain center and the wheel center
$\bar{r}_g$	Average of the grain radius
r_g^x	X-component of grain base radius of an ellipsoidal grain
r_g^y	Y-component of grain base radius of an ellipsoidal grain
r_g^z	Z-component of grain base radius of an ellipsoidal grain
r_{p_0}	Mean radius of the grinding wheel
R_p	Polar coordinate component (victor)
R_x	Random number
R_y	Random number
R_z	Random number
q	Speed ratio
P_h	Protrusion height
$P(p)$	probability of the active grains
S	Structure number
s_d	Dressing lead
t	Time
v_a	Dressing cross-feed velocity
V_g	Grain volume fraction or packing density
$V_{g,SC}^{cub}$	Grains volume in one cell of SC
v_i	Dressing feed velocity
v_r	Diamond rotary roll velocity

v_s	Cutting speed
V_t	Volume of the torus
v_w	Workpiece velocity
U_d	Overlap ration
x	Cartesian coordinate x-component
x_c	Grain center x-component
x_w	Grinding wheel center x-component
y	Cartesian coordinate y-component
y_c	Grain center y-component
y_w	Grinding wheel center y-component
$z(x)$	Grain fracture profile
z_c	Grain center z-component
$z_d(x)$	Dressing tool profile
$z_g(x)$	Fractured grain profile
z^{gr}	Grain profile
$z_t(x)$	Dressing tool trace
$z^{fr}(x, y)$	Stochastic periodic function
z_w	Grinding wheel center z-component
α	Random phase angle
β	Grain angle
Δ	Range of grain size
Δ_{ind}	Wheel indentation (depth of cut)
δ_p	Sampling interval per pulse
δt	Time step
δ_y	Depth in y-direction
θ	Angle
θ_p	Polar coordinate component (angular)
ω	Random frequency
$\widehat{\omega}_x$	Random number
$\widehat{\omega}_y$	Random number
ρ	Packing density
σ	Standard deviation
σ_d	Standard deviation of the grain diameter
σ_{ls}	Line segment density
σ_r	Standard deviation of the grain radius
φ	Angle
$\emptyset$	Phase angle
∂	Random value

Acknowledgement

Over the past five years I have received support and encouragement from a great number of individuals. Foremost, I would like to express my sincere gratitude to my advisor **Dr. Andrew Warkentin** for the continuous support of my PhD study and research, for his patience, motivation, enthusiasm, and immense knowledge. His guidance helped me in all the time of research and writing of this thesis. I could not have imagined having a better advisor and mentor for my PhD study. I would also like to thank my supervisory committee **Dr. Robert Bauer** and **Dr. Zoheir Farhat** for their encouragement, guidance, insightful comments and advice. I must thank the Atlantic Computational Excellence Network ACEnet, the regional high performance computing consortium for universities in Atlantic Canada, for providing the computational facilities necessary for this work.

Many thanks go to my colleague **Al-Mokhtar Mohamed** for his experience and help during the experimental work. I also thank my friend **Fozi Alsagheer** for his great help and advices during my first days in Canada and Dalhousie. Thanks and respects should also be given to my best friend **Tareg Naser** for his encouragement, trust, support, and prayer during my study.

I must acknowledge the financial support provided from the Libyan Ministry of Higher Education and Scientific Research over five years, and I am looking forward to pay the price by contributing in the building of the new free Libya. I also appreciate the CBIE (Canadian Bureau of International Education) for their perfect work in managing and administrating my scholar program, and facilitating the difficulties especially during the conflict period in Libya (2011).

Last but not the least, I would like to thank my family, my parents, my sisters and brothers, and my friends for the support and encouragement.

CHAPTER 1. INTRODUCTION

1.1 Introduction

The grinding operation is a key manufacturing step for the production of components requiring smooth surfaces and for tight tolerances on flat and cylindrical surfaces [1, 2]. The grinding operation at the macro-scale has been extensively studied in areas such as normal and tangential forces, power consumption, workpiece surface finish, and heat transfer. There is, however, still a lack of clear understanding at the micro-scale. The fundamentals of chip formation, grinding wheel topography and un-deformed chip geometry need more investigation. Thus, the topic of this thesis is the measurement and the modeling of grinding wheel surface topography as well as the modeling of the removal process in grinding. Better understanding of the aspects of the grinding wheel topography and the wheel/workpiece interaction at the micro-scale leads to better designs of grinding wheels and grinding processes.

1.2 Objectives

The objectives of this work were to:

- Develop a method to accurately measure the entire surface of a grinding wheel in 3D.

- Develop a method to model the surface topology of grinding wheel in 3D with and without dressing.
- Develop a metal removal model to determine the uncut chip geometry for each cutting edges on the grinding wheel surface and to predict the surface finish of the workpiece.
- Study the effects of dressing on the surface topography of grinding wheels, uncut chip geometry and workpiece surface finish.

1.3 Organization of thesis

This work is organized into eight chapters. In the following chapter the grinding process is introduced. The grinding wheel composition, grinding mechanics, grinding kinematics and the dressing operation will be briefly reviewed. In chapter 3, grinding wheel topography models and grinding wheel topography measurement will be reviewed. Chapter 4 will present the 2D metal removal simulation for grinding which was used to calculate the uncut chip thickness and contact length, and to study the effect of the distribution of grain size, spacing and protrusion height on the chip geometry. Chapter 5 will discuss the 3D model of the metal removal for grinding. The roughness of the ground surface will then be predicted and compared with experimental results. Chapter 6 will present the development of the grinding wheel topography measurement system. The effect of the dressing conditions on the grinding wheel topography will be investigated. In Chapter 7, a new dressing model will be presented. The model will be assessed by comparing the characteristic of the simulated dressed wheel and workpiece surfaces with the measured wheel surfaces. Subsequently, the dressed wheel model will be used to determine the uncut chip thickness and contact length. Finally Chapter 8 will present the conclusions drawn from the work carried out in this thesis, followed by the contributions and recommendations.

CHAPTER 2. GRINDING PROCESS

2.1 Introduction

A grinding operation is a process in which unwanted material is removed from a workpiece by hard abrasive particles. In fact, the grinding process is an ancient practice; it is probably the oldest machining process in existence. Prehistoric man found that he could sharpen his cutting tools by rubbing them against hard gritty rocks. In the present, using a suitable bond material, the small abrasive particles are formed into the shape of a wheel. The abrasive grains on the grinding wheel act as cutting tools. In the grinding process the rotating grinding wheel is brought into contact with the workpiece surface. The exposed abrasive grains remove tiny chips of metal from the workpiece, as shown in Figure 2.1. This chapter briefly introduces the grinding wheel fabrication, dressing operation and the mechanics of grinding.

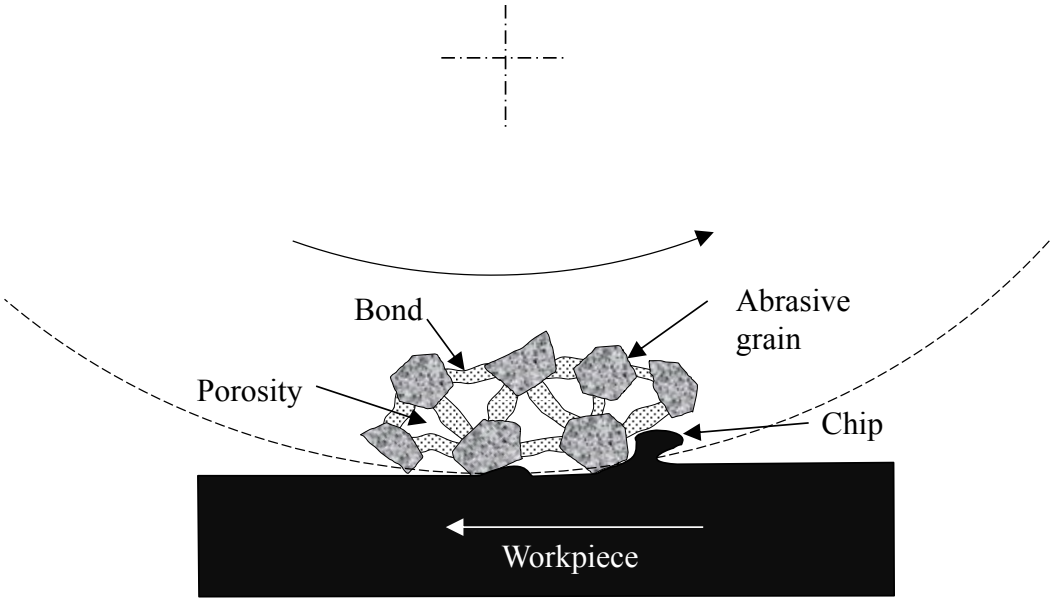

Figure 2.1 Illustration of grinding wheel components and the chip formation.

2.2 Grinding wheel composition

The grinding wheel consists of the abrasive grains, bond material and porosity. Figure 2.2 shows a Scanning Electron Microscope (SEM) micrograph of a typical grinding wheel, where the grains, bonding material and porosity (voids) are clearly visible. The abrasives commonly used are aluminum oxide, silicon carbide, cubic boron nitride (CBN) and diamond. CBN and diamond are the hardest materials known, hence, they are known as super-abrasives. The abrasive grains have irregular shape and size; a grain may have more than one cutting edge [3].

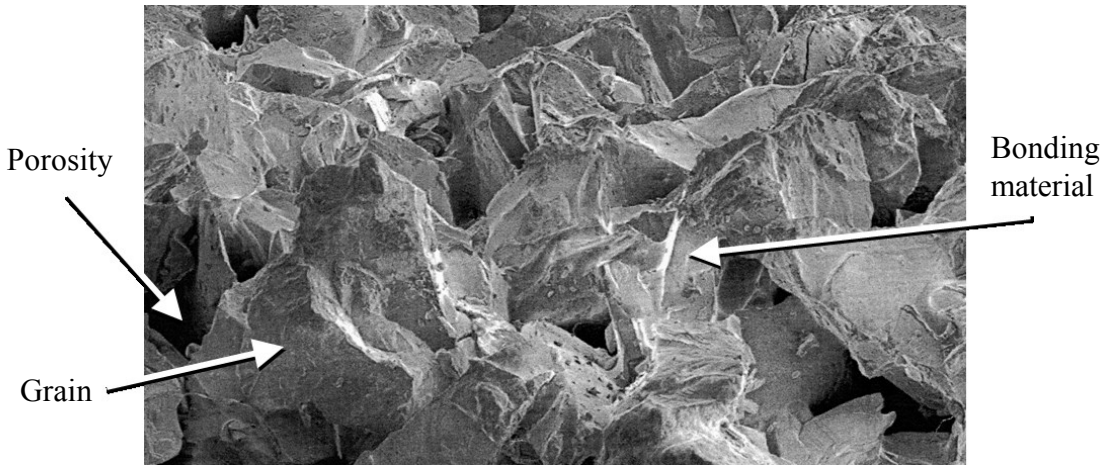

Figure 2.2 SEM micrograph of a grinding wheel.

2.3 Grinding wheel standard marking system

The grinding wheel standard marking system provides the user with key information regarding the construction of the grinding wheel including the following information:

1. The type of abrasive grains
2. The size of abrasive grains
3. The hardness of the grinding wheel
4. The wheel structure number
5. The bond type

Figure 2.3 illustrates the marking system for conventional grinding wheels containing aluminum oxide and silicon carbide abrasive, which is defined by the American National Standards Institute (ANSI) by Standard B74.13-1977 [4]. It starts with a prefix for the manufacture's symbol, which indicates the exact kind of abrasive, followed by the possible parameters for the wheel specification as mentioned above, and ends with a manufacturer's record, which is to identify the wheel.

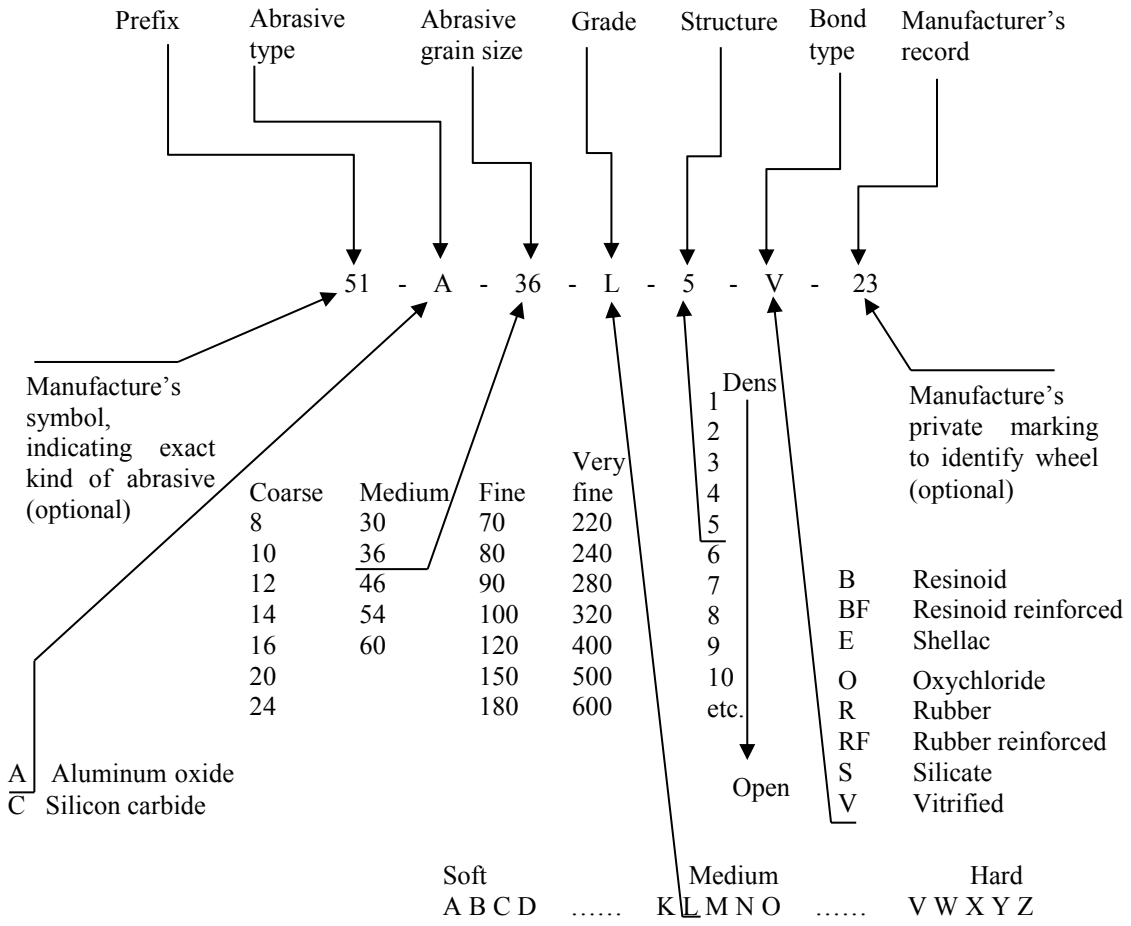

Figure 2.3 Standard marking system for aluminum-oxide and silicon-carbide bonded abrasives.

The conventional grinding wheel consists of either aluminum oxide or silicon carbide abrasives, which are indicated in the wheel marking system by the letter A or C respectively. The size of an abrasive grain is identified by a grit number, which is related to the screen used to sort the grains. A larger grit number indicates a smaller grain size.

The sieving process consists of passing the abrasive grains through a stack of standard sieves from the coarser meshes in the top to the finer meshes in the bottom. Coarse grains are collected from sieves with grit number from 8 to 24, medium grains are collected from sieves with grit number from 30 to 60, fine grains are collected from sieves with

grit number from 70 to 180 and very fine grains are collected from sieves with grit number from 220 to 600.

Given the standard grit number M the abrasive grain size d_g can be estimated from the following relationship [2]:

$$d_g = 15.2\, M^{-1}\ [mm] \tag{2.1}$$

The wheel grade or hardness in the wheel marking system is identified by a letter from A (soft) to Z (hard). Regardless of the abrasive and bond material type, harder wheels contain less porosity and more bond material. For example wheel with grade Z contains 2% porosity and wheel with grade A contains 52% porosity [5]. The next number in the wheel marking system is the structure number, which indicates the volume fraction of the abrasives in the grinding wheel. A small structure number indicates more abrasive grains or more packing density. The relationship between the grain volume fraction V_g and the structure number S is shown in the following equation [2]:

$$V_g = 0.02(32 - S) \tag{2.2}$$

The abrasive grains are held together using a bond. In the wheel marking system the bond material is specified by the first letter of the material type, for example V for vitrified. In general, the bond must be strong enough to withstand against grinding forces, high temperature, and centrifugal forces without disintegrating. Some porosity is essentially integrated into grinding wheels to provide clearance for the tiny chips being formed and to carry the coolant to the cutting zone.

2.4 Grinding mechanics

Like all other machining methods, the material removal by grinding is accomplished by a chip formation process, however, in much finer scale. The cutting-tool geometry and its interaction with the workpiece in the grinding are not as well defined as in other

machining process such as turning and milling. There are major factors that differentiate the action of the abrasive grains from the other single-point tools:

1. There is a significant variation in the abrasive geometry along the circumference of the grinding wheel.
2. The abrasive grains are stochastically distributed and oriented.
3. The radial position of the abrasive grains in the grinding wheel varies, which means the cutting edges' protrusion height from the grinding wheel working surface varies and each abrasive grain has different depth of cut.
4. The majority of the abrasive grains have a highly negative rake angle; the average is -60^o, which results in a very low shear angle (see Figure 2.4).
5. The cutting speed in grinding is very high, the typical cutting speed is 20-30 m/s, and in extreme cases the cutting speed can rise up to 120 m/s.

There are three phases of grain/workpiece interaction. These include rubbing, plowing and cutting [2, 6] as shown in Figure 2.4. In the beginning of the grain/workpiece interaction the cutting depth is very small which results in sliding the grain over the workpiece with high friction resulting in elastic deformation in the workpiece. This phase is named rubbing. The second phase, called plowing, occurs when the depth of cut increases to the point where plastic deformation occurs on the workpiece surface and the material flows around the cutting edges. The last phase is cutting when the depth of cut increases to the point where the chip is formed. These mechanisms make the cutting action of individual grains inefficient in comparison to a conventional cutting tool. It is one reason why the energy generated per volume of material removed in grinding is far greater than in other machining processes.

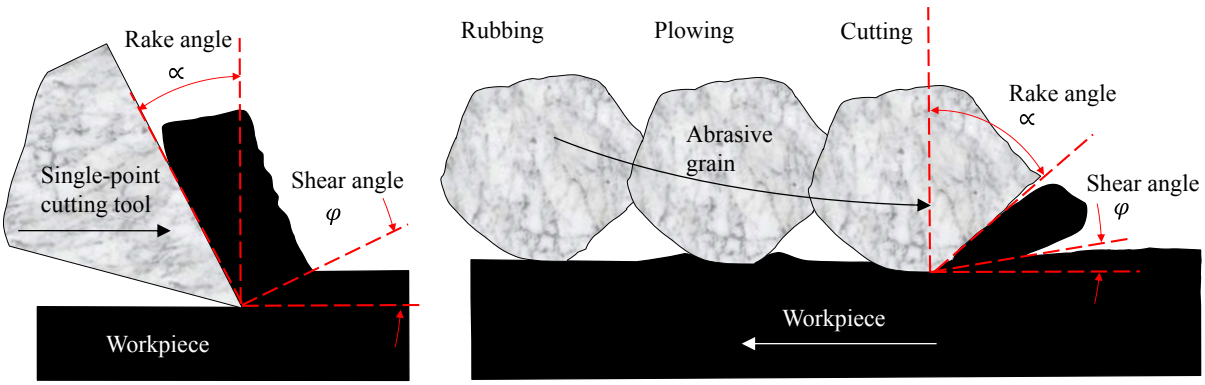

Figure 2.4 Rake angle and shear angle in abrasive grain and single-point cutting tool.

2.5 Grinding kinematics and the un-deformed chip geometry

Figure 2.5 illustrates the kinematics of the surface grinding operation. A grinding wheel with diameter of d_s removes material from the workpiece with grinding depth of cut of a. An individual abrasive grain on the wheel peripheral is moving at a tangential velocity of v_s, while the workpiece is translating at a velocity of v_w. Penetration of the grinding wheel into the workpiece results in an apparent area of contact where the material removal action occurs. The active grains, which participate in the material removal process, are assumed to be in contact with the workpiece along this area. The produced chips will have an un-deformed length, named the contact length l_c. The un-deformed chip also has a thickness, named the uncut chip thickness $h_{m,}$ which gradually increases as the chip is being cut. The maximum uncut chip thickness h_m and contact length l_c are the two most important geometric parameters in grinding mechanics.

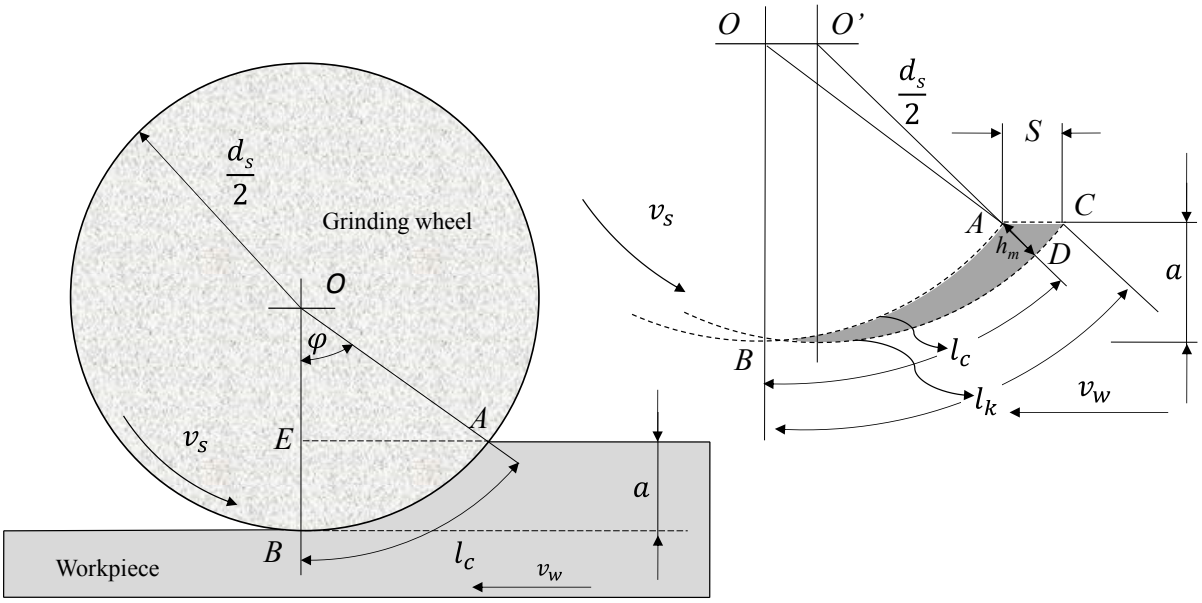

Figure 2.5 Surface grinding.

Neglecting the motions and the deformations of the grinding wheel and workpiece, the arc length of contact can be generally expressed as [2]:

$$l_c = BA = \frac{d_s \varphi}{2} \tag{2.3}$$

From Figure 2.5, it can be readily shown that [2]:

$$cos\,\varphi = \frac{OE}{OA} = \frac{\frac{d_s}{2} - a}{\frac{d_s}{2}} = 1 - \frac{2a}{d_s} \tag{2.4}$$

Since $2a \ll d_s$ the small angle approximation would apply [2].

$$cos\,\varphi = 1 - \frac{\varphi^2}{2} \tag{2.5}$$

Combining Equation (2.5) with Equation (2.3) and (2.4) leads to the result [2]:

$$l_c = \sqrt{ad_s} \tag{2.6}$$

This expression for the contact length l_c can be shown to be identical to the chord length AB. Therefore, the contact length l_c is considered to be a static approximation of the cutting-path length or the un-deformed chip length [2]. The cutting path length l_k as given by Equation (2.7) can be considered as a kinematic correction to the static contact length l_c, and is known as a kinematic contact length [2].

$$l_k = \left(1 + \frac{v_w}{v_s}\right) l_s + \frac{s}{2} \tag{2.7}$$

In order to derive Equation (2.7) the abrasive grains are assumed to be points that are evenly distributed around the circumference of the grinding wheel and evenly protruded from the grinding wheel working surface; moreover, the abrasive begins its contact with the workpiece at point B and follows the curved path to point A in a circular trajectory (see Figure 2.5). This assumption implies an intermittent motion in which the workpiece remains stationary during an individual cut, and then moves suddenly from point O to point O' by the distance S before the next cutting point engages. The distance S is defined as the feed per cutting edge, which is influenced by the wheel tangential speed v_s, the workpiece translation speed v_w and the distance between adjacent abrasives L known as grain space, and can be calculated using the following equation [2]:

$$s = \frac{L\, v_w}{v_s} \tag{2.8}$$

In Figure 2.5 the maximum uncut chip thickness h_m is the distance from A to D. Based on Figure 2.5 and using mathematical derivation the maximum uncut chip thickness h_m can be calculated using the following equation [2]:

$$h_m = 2L \left(\frac{v_w}{v_s}\right) \left(\frac{a}{d_s}\right)^{\frac{1}{2}} \tag{2.9}$$

The mathematical derivation of Equation (2.9) can be found in [2]. The grain spacing can be approximated as follows: if the grains in the grinding wheel are assumed to have a simple cubic packing structure, then the grain volume fraction V_g of the unit cell must be [6]:

$$V_g = \frac{\pi {d_g}^3}{6{L_{cell}}^3} \tag{2.10}$$

where L_{cell} is the length of the unit cell and each unit cell contains one grain. Combining Equations (2.8) and (2.9) results in the following equation [6]:

$$L_{cell} = \left(\frac{\pi {d_g}^3}{0.12(32 - s)}\right)^{\frac{1}{3}} \tag{2.11}$$

The cutting edge density is the number of cutting edges per unit area. Since there is a total of one complete cutting edge on the face of each unit cell the cutting edge density for simple cubic packing, therefore, is [6]:

$$C_A = \frac{1}{{L_{cell}}^2} \tag{2.12}$$

If the average cutting edge is assumed to be $k\, d_g$ wide, then the spacing between the cutting edges is [6]:

$$L = \frac{1}{k\, C_A d_g} \tag{2.13}$$

where $0 \leq k \leq 1$ is the ratio of cutting edge width to grain diameter.

2.6 The dressing operation

The dressing operation is the process of conditioning the grinding wheel working surface to achieve a desired grinding behavior. Even a newly mounted grinding wheel should be

dressed prior to the first operation in order to generate a satisfactory grinding wheel topography, which has significant impact on the workpiece surface roughness, grinding force, power and temperature.

Many procedures have been developed to dress grinding wheels. These procedures are generally based on one of two general methods. These methods are single-point dressing and rotary dressing. Figure 2.6 illustrates the dressing operation by a single-point dressing tool, which is accomplished by feeding the dressing tool with a cross-feed velocity of v_a across the rotating wheel surface with a tangential velocity of v_s and with a dressing depth of a_d. This kind of dressing motion is analogous to the turning operation on a lathe.

The axial feed of the dressing tool per wheel revolution is called the dressing lead s_d, which can be calculated by the following equation [2]:

$$s_d = \frac{\pi\, d_s\, v_d}{v_s} \tag{2.14}$$

The overlap ratio U_d is the ratio of the active width b_d of the single-point diamond tip to the dressing lead s_d [6].

$$U_d = \frac{b_d}{s_d} \tag{2.15}$$

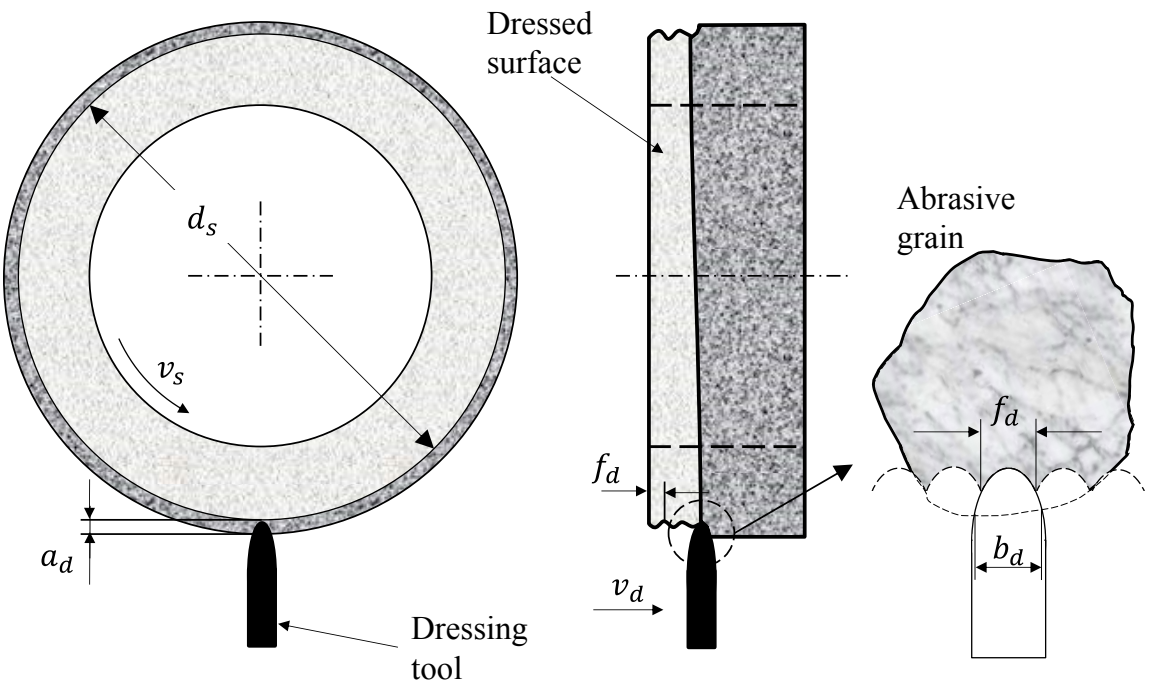

Figure 2.6 Single-point dressing of grinding wheel.

Another dressing method uses a roll covered in diamonds. One of the advantages of this kind of dressing is the relatively quick dressing for complex wheel profiles [7]. In this method the grinding wheel with peripheral velocity of v_s is fed radially into the rotating roll with a peripheral velocity of v_r at a feed velocity of v_i, which is corresponding to a depth per wheel revolution a_r, see Figure 2.7. Dressing in-feed velocity is a dressing condition used to represent the amount of removed wheel per revolution [8]. The dressing ratio, which is the ratio of the dresser peripheral velocity to the wheel peripheral velocity, is also used to identify the dressing condition. When the dressing ratio approaches 1.0, which is called crush dressing, the abrasive grains and the bonding material in the area of the contact may be destroyed by the high compressive stress [8, 9].

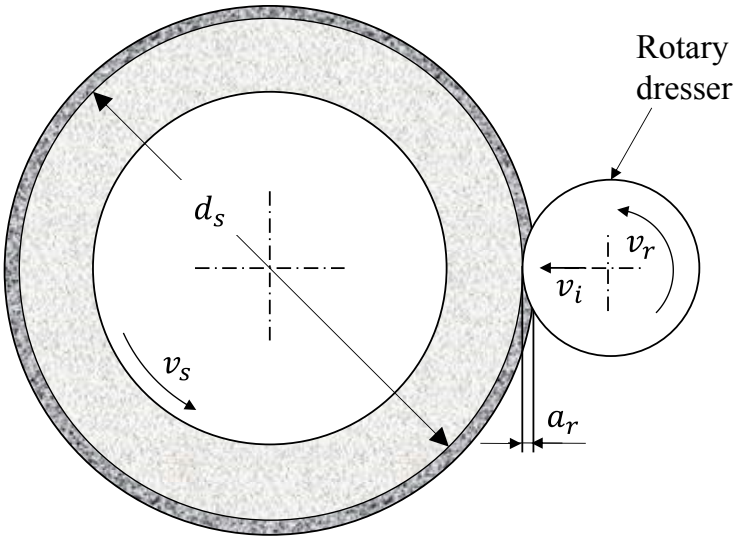

Figure 2.7 Rotary dressing of grinding wheel.

2.7 Summary

In this chapter the grinding process was briefly introduced. It was shown that, despite the fact that grinding wheels are carefully classified using the marking wheel standard, each grinding wheel has a different topography. The stochastic grain size, grain shape, grain orientation and grain spatial distribution on the grinding wheel working surface play a pivotal role in the topography of the grinding wheel. This fact makes it extremely difficult to accurately model the un-deformed chip geometry (uncut chip thickness and contact length) and workpiece surface quality. The standard analytical approach for calculating the uncut chip thickness and contact length, which is based on some problematic assumptions, was also reviewed in this chapter. The analytical approach will be compared with an experimental validated simulation technique in Chapter 5 and Chapter 7.

CHAPTER 3. GRINDING WHEEL TOPOGRAPHY MODELS

3.1 Introduction

The grinding process has been known for thousands of years; however, it was not scientifically examined until the middle of the 1940's [1]. In the years that followed, much research has been focused on this field. These days, grinding operations are a vital economic constituent in many industrialized countries [10]. Modeling of grinding operations requires the consideration of the grinding wheel topography. Understanding the geometry of the cutting edges, which are stochastically distributed and oriented on the grinding wheel circumference, and understanding the mechanism of chip formation leads to a better understanding of the grinding process.

There are two principle strategies to obtain a topography model for a grinding wheel: using scanned information from a real grinding wheel surface topography, or modeling the surface topography. In this chapter grinding wheel models will be reviewed followed by grinding wheel measurement techniques.

3.2 Grinding wheel models

Doman *et al.* [10] has classified the grinding wheel topography models into three types: one dimension (1D), two dimensions (2D) and three dimensions (3D). The definition of 1D is that the model is unable to provide topographical details of the wheel surface. In other word, the wheel surface is characterized by parameters such as surface roughness and the number of cutting edges that are exposed on the wheel surface. In 2D model, the grains are described geometrically rather than empirically. Subsequently, the grain size distribution, location, protrusion height and the dressing effect are investigated [11-13]. In 3D models, not only the grain position and shape are described as three-dimensional object, but the 3D surface is simulated [14] or measured [15] to describe the wheel surface topography in three dimensions.

3.3 One dimensional topography models

One dimensional grinding wheel topography models were constructed to define grinding wheel characteristics, such as wheel surface roughness and number of cutting edges [10]. Peklenik [3] has concluded that any given abrasive grain might have multiple cutting edges. Later Verkerk *et. al* [16] reported that the cutting edges that belong to the same grain or to adjacent grains might be considered as a single cutting edge, because they do not have the chip clearance needed for chip formation. These conclusions were used as guides to classify the abrasive grains into two types: static and kinematic cutting edges. The number of static cutting edges is the summation of all the cutting edges. Whereas, the number of kinematic cutting edges refers to the sum of only the cutting edges that contribute in the chip formation process. The kinematic cutting edges are also known as the active cutting edges.

In 1952 Backer *et al*. [17] rolled a grinding wheel under its own weight on a glass plate covered by carbon powder. The resulting image was enlarged and projected on a screen in order to count the spots on the projected picture that indicate the number of cutting points. It can be noted that the obtained result was actually an estimation of the number of peaks on the abrasive grain that protrude from the grinding wheel surface and have

penetrated in the carbon film, not necessarily the number of actual active cutting edges. This technique and its similarities are classified as static methods of determining the number of cutting edges.

3.3.1 Basic topography model by Tonshoff

In 1992 Tonshoff [18] made a survey of topography models prevalent in European grinding research. Most of these models [19-24] focused on the development of empirical formulas, which define the static and kinematic number of the cutting edges for a given grinding wheel. The estimated kinematic cutting edge density was defined as a function of four factors, including the cutting edge shape (SF), the speed ratio (SR), which is the peripheral velocity of the grinding wheel to the workpiece speed, the depth of cut (DC) and the grain size (GS). The basic formula of the kinematic cutting edge density was [18]:

$$N_{kin} = (SF)(SR)(DC)(GS) \tag{3.1}$$

The static grain density was quantified experimentally, using various techniques such as profilometry or the stylus method. Tonshoff [18] proposed basic models in Equation (3.2) and (3.3) that define the static and kinematic cutting edges, respectively, in order to compare different models in the grinding wheel topography, which had been developed prior to 1992.

$$N_{st} = C_{st}\, z^{A_3} \tag{3.2}$$

$$N_{kin} = A_{gw}\left(\frac{a}{q^2 d_{eq}}\right)^{\frac{A_2}{2}} \tag{3.3}$$

In Equation (3.2) and Equation (3.3) N_{st} and N_{kin} are the number of static and kinematic cutting edges, respectively, C_{st} is the volumetric static cutting edge density (grain per unit

volume), a is the depth of cut, d_{eq} is the equivalent grain diameter, q is the speed ratio, A_{gw} is the cutting edge shape constant, and A_2 and A_3 are empirical constants.

3.3.2 Fractal theory and Warren Liao model

The fractal theory was originated in 1975 by Mandelbrot [25]. Fractals are typically self-similar patterns that make an object. The self-similarity means that objects are the same from near as from far. The object that is generated by the fractal theory can be split into parts; each part is a copy of the object. Figure 3.1 illustrates an example of fractal objects called "Sierpinski triangle". In the figure self-similar triangles are arranged to make triangular object.

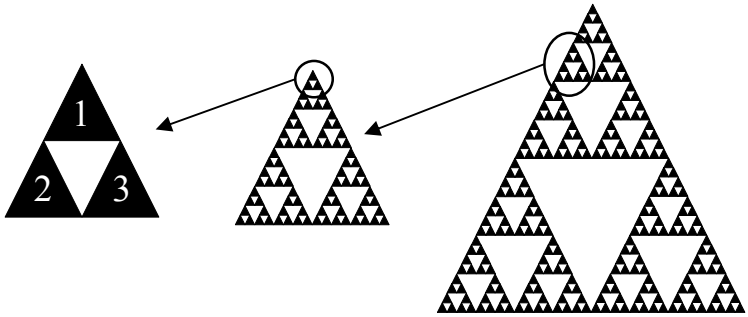

Figure 3.1 Sierpinski triangle.

The fractal dimension indicates details in a pattern. Given self-similarity objects of N parts scaled by size r_p from the whole, the fractal dimension D is defined by [10]:

$$D = \frac{\log(N)}{\log\left(\frac{1}{r_p}\right)} \tag{3.4}$$

For example in the fractal shown in Figure 3.1, there are three self-similar triangles making an object in which a single triangle is scaled by half of the entire fractal object. Thus fractal dimension is:

$$D = \frac{\log(3)}{\log\left(\frac{1}{0.5}\right)} = 1.585 \tag{3.5}$$

The fractal theory has been used to characterize a ground workpiece, paper-ground and grinding wheel topographies [26-28], because the abrasive grains have quite similar geometry. Warren [29] used the fractal dimension to characterize a diamond grinding wheel. The fractal dimension of the grinding wheel profile was determined for different scale lengths, as illustrated in Figure 3.2. From the figure, it can be noticed that the scale length controls the profile shape. When the scale length decreases, more of the profile detail is gained and the profile length becomes longer. Warren [29] used the following equation to calculate the fractal dimension.

$$D = 1 - \frac{\log(L_p)}{\log(r_p)} \tag{3.6}$$

where L_p is the total profile length and r_p is the scale length. Warren [29] concluded that a finer wheel requires a shorter scale length (or sampling interval) to estimate the surface roughness of the grinding wheel.

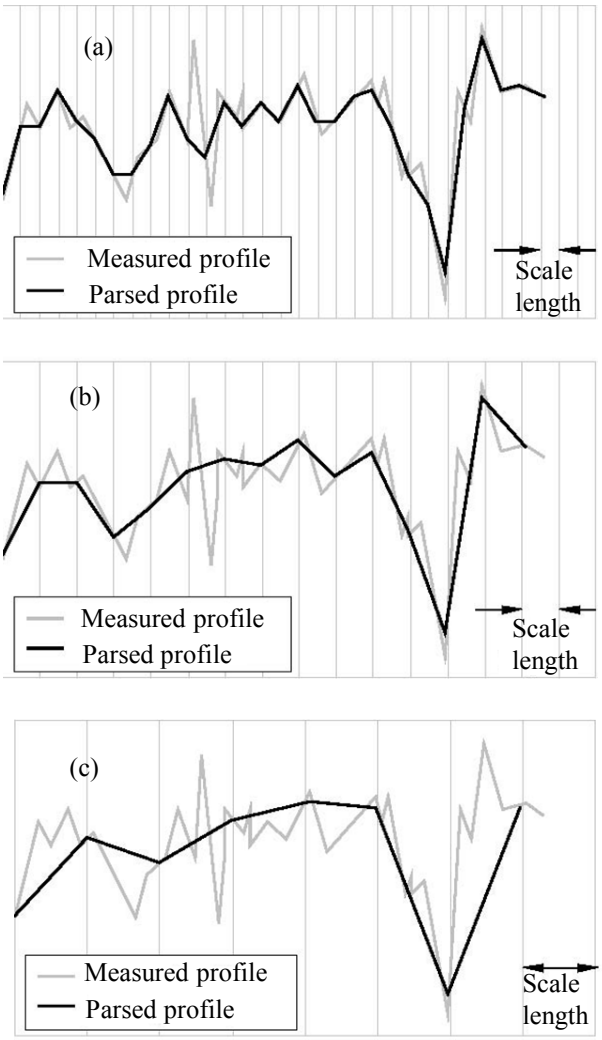

Figure 3.2 Schematic of grinding wheel profile with (a) fine, (b) medium, and (c) coarse scale length [29].

3.3.3 Hou and Komanduri model

In 2003 Hou and Komanduri [30] provided a grinding wheel topography model based on stochastic approaches. The model determined the number and the probability of a certain grain size within the grinding wheel volume. Figure 3.3 plots of the mean grain diameter d_{g_mean} versus the grain size d_g, which can be obtained from the grinding wheel marking system, from which the following best-fit relation was obtained [30]:

$$d_{mean} = 28.9\, {d_g}^{-1.18} \tag{3.7}$$

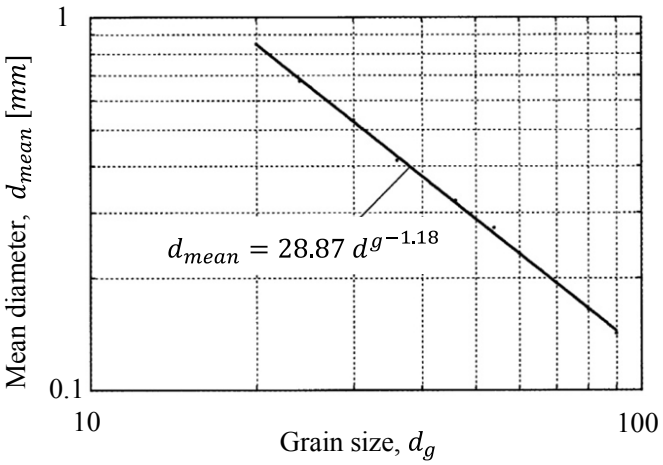

Figure 3.3 Plot of the mean grain diameter versus the abrasive grain size [30].

Hou and Komanduri [30] determined the average number of the grains per unit length on the surface of the grinding wheel N_l by using the following equation:

$$N_l = \frac{10}{d_{mean}}\, {V_g}^{1/3} \tag{3.8}$$

In the above equation V_g represents the abrasive grains volume fraction. Therefore, the average number of the grain per unit area N_a is given by [30]:

$$N_a = {N_l}^2 = \left(\frac{10}{d_{mean}}\, {V_g}^{1/3}\right)^2 \tag{3.9}$$

Hou and Komanduri [30] assumed that the abrasive grain size on the grinding wheel surface conforms to a normal distribution. The normal distribution function is mathematically expressed by the following equation [30]:

$$P(x) = \frac{1}{\sqrt{2\pi}} e^{(-0.5x^2)} \tag{3.10}$$

where $P(x)$ is the probability of value x. Figure 3.4 plots the probability versus the grain size. The probability of a range of grain size (from $d_g = a$ to b) could be defined by integrating the probability carve from the lower integration limit of a to the upper integration limit of b, see Equation (3.11), which determines the area between the limits and the curve.

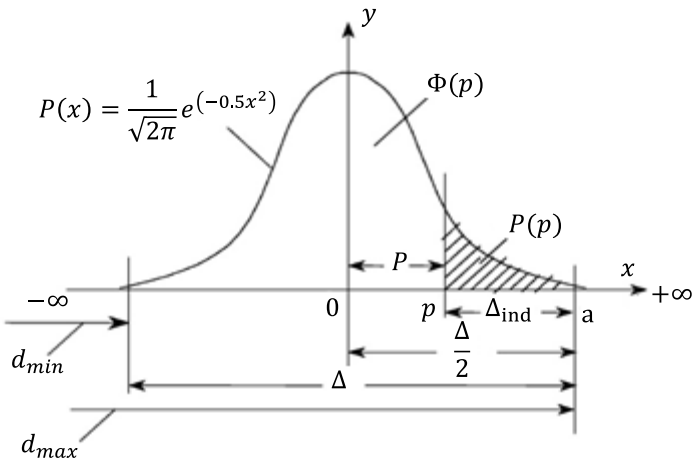

Figure 3.4 Normal distribution plot of the frequency versus the grain diameter [30].

$$P(d_g) = \frac{1}{\sqrt{2\pi}} \int_b^a e^{(-0.5{d_g}^2)} \, d(d_g) \tag{3.11}$$

Figure 3.5 illustrates a schematic of grains with various sizes which are aligned to the top. Hou and Komanduri [30] assumed that the grains with size from $d_g = p$ to $d_g = d_{max}$ are active grains. Thus, Equation (3.11) was used with upper lower limit of p and

upper limit of $+\infty$ to calculate the probability of the active grains, area $P(p)$ in Figure 3.4. The lower limit of active grain was defined by the following equation [30]:

$$p = \left(\frac{\Delta}{2} - \Delta_{\text{ind}}\right) \frac{4.4}{\frac{\Delta}{2}} \tag{3.12}$$

where δ is the range of grain size and Δ_{ind} is the depth of cut.

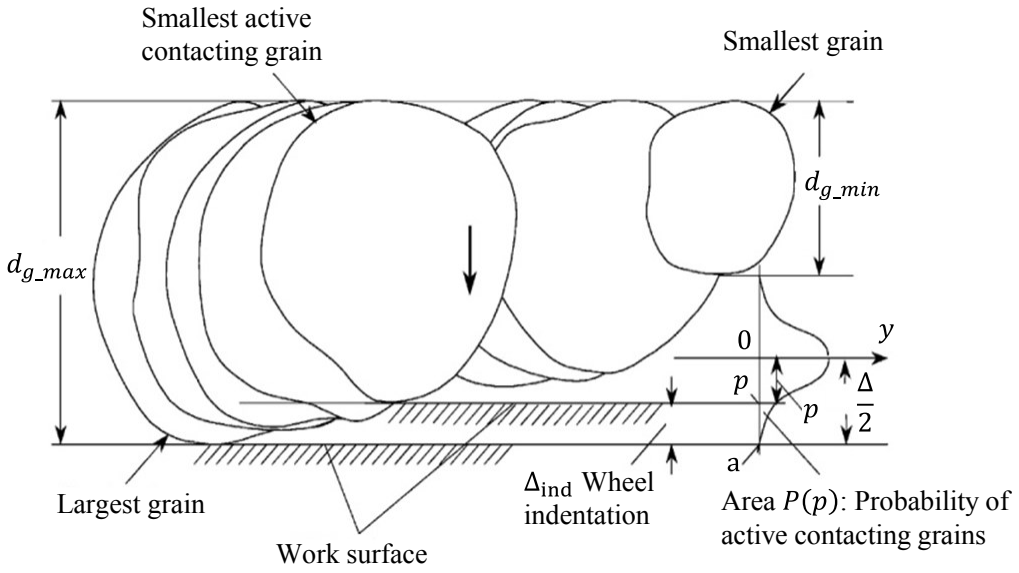

Figure 3.5 Grain size distribution and the probability of active grains [30].

3.3.4 Koshy *et al*. model (1)

Koshy *et al*. [12] developed a topography model of a freshly dressed resin/metal bonded diamond grinding wheel. The formulated mathematical model estimates the planer grain density, the percentage area due to the abrasives on the wheel surface and the abrasive protrusion height distribution.

The grains were assumed to be spherical in shape with a radius distribution that conforms to a symmetric truncated normal distribution as shown in Figure 3.6. The probability density function of grain radius r_g is given by the following equation [12]:

$$f_R(r_g) = \frac{A_4}{\sigma_r\sqrt{2\pi}}\, e^{\left[-0.5\left(\frac{r_g-\bar{r}_g}{\sigma_r}\right)^2\right]}, \quad r_{g_1} \le r_g \le r_{g_2} \tag{3.13}$$

where $\bar{r}_g$ is the average of the grain radius and σ_r is the standard deviation of the grain radius, which was given by the following equation [12]:

$$\sigma_r = \frac{r_{g_2} - r_{g_1}}{6} \tag{3.14}$$

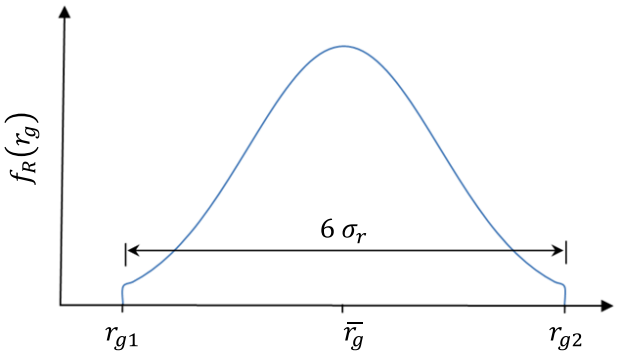

Figure 3.6 Distribution the grain radius [12].

The term A_4 in Equation (3.13) is an empirical constant. Koshy *et al*. [12] considered a cube of volume l^3 units of the wheel material for modeling as shown in Figure 3.7. Equation (3.13) was used to define the probability of the protrusion height of the grains that exists between two arbitrary heights a and b (see Figure 3.7) as follows [12]:

$$P(a \le r_g + y \le b) = \frac{1}{l + 0.4\bar{r}_g} \int_{-0.2\bar{r}_g}^{l+0.2\bar{r}_g} \left(\int_{l+a-y}^{l+b-y} f_R(r)\, dr \right) dy \tag{3.15}$$

where l is the length of the cubic of the wheel material and y is the coordinate of the grain center as shown in Figure 3.7.

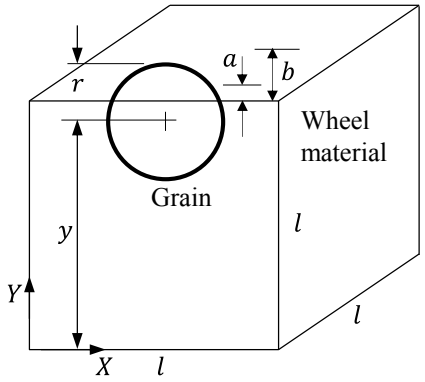

Figure 3.7 Parameters of the mathematical model.

Koshy *et al.* [12] estimated the average number of the grains that protruded above the bond level using the following equation:

$$N_{av}^{p} = \frac{V_g}{0.75\,\pi\,\bar{r}_g^{\,3}}\,P(a \le r_g + y \le b) \tag{3.16}$$

where V_g is the volume of the abrasives. Figure 3.8 shows the distribution of protrusion heights for various grinding wheels with different mesh numbers for cube size $l = 10\ mm$. Koshy *et al.* [12] compared the result using Equation (3.15) with experimental data reported by Yuhta *et al*. [31] and Syoji *et al.* [32]. It was found that Equation (3.15) predicted a maximum protrusion height of 34 μm for mesh number 270/325, and 65 μm for mesh number 140/170. While the experimental data reported by Yuhta *et al.* [31] and Syoji *et al.* [32] predicted the maximum protrusion height of 30 μm and 67 μm for these grain sizes, respectively.

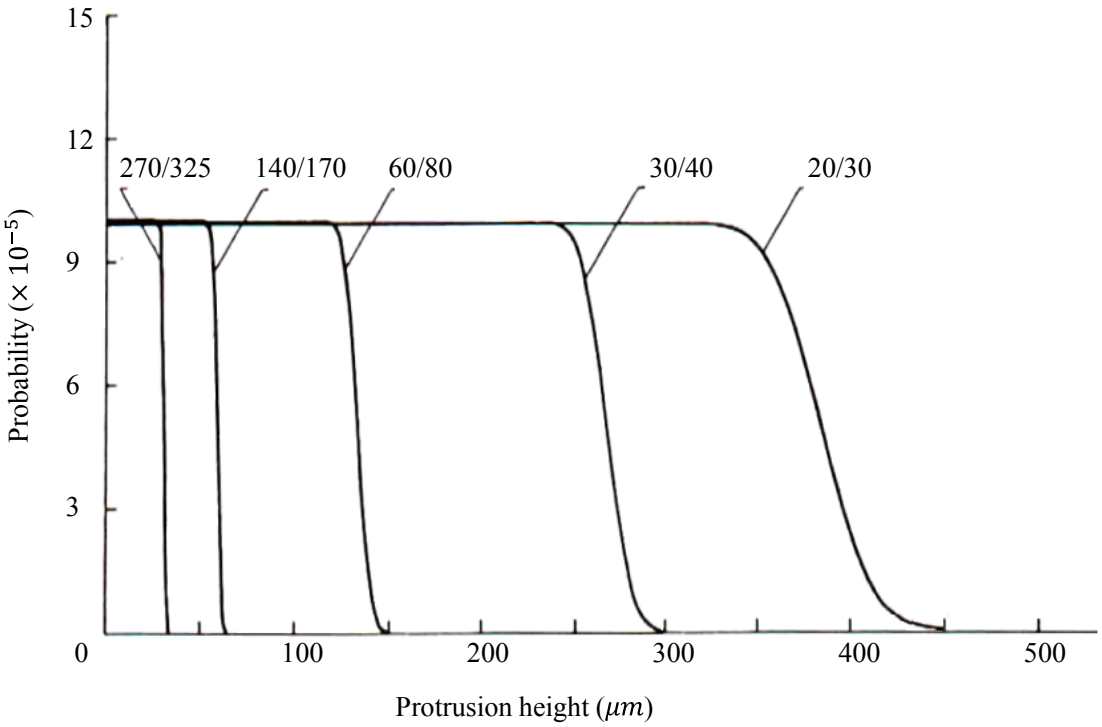

Figure 3.8 Protrusion height distribution for various grit size [12].

3.4 Two dimensional topography models

3.4.1 Koshy *et al.* model (2)

In 1997 Koshy *et al.* [13] expanded their 1D model [12] to 2D model, which presented a stochastic simulation of metal/resin-bonded diamond grinding wheels. Diamond abrasive grains were stochastically distributed in a volume of a cube of side l. The grain size was assumed to conform to normal and symmetrically distributed about the mean grain diameter. The standard deviation of the grain diameter σ_d was given in Equation (3.17) [13].

$$\sigma_d = \frac{d_{g\_max} - d_{g\_min}}{6} \tag{3.17}$$

Since the model was related to the topography of a resin/metal bonded diamond grinding wheel, it was assumed that the dressing operation does not act on the abrasive grains but the bond material. Under appropriate conditions some dressing techniques may dress the diamond wheel with little or no damage to the diamond abrasives including electrochemical [33], electrical discharge [34], and rotary wire brush [35].

The dressing operation gradually removes the bond material around the diamond abrasives. As a result, the protrusion heights of the abrasives are increased. Eventually, the abrasives that are not rooted deep enough in the bond material cannot withstand the dressing load; hence, these grains are dislodged from the bond material. In Figure 3.9 the dislodgement of a grain with a diameter of d_g occurs when the relation (3.18) is satisfied [31, 36, 37].

$$\frac{x}{d_g} \geq 0.1 \tag{3.18}$$

The abrasive grains were stochastically sized and distributed in the bond material. The bond material was represented as a cubic with a side of l. The x, y, and z coordinates of the center of each grain was uniformly distributed between $(-0.1\mathrm{d_g})$ and $(\mathrm{l} + 0.1\mathrm{d_g})$. The distribution of grain location had to pass the condition shown in Equation (3.19) [13]. This condition ensures no overlapping between the grains.

$$\sqrt{\left(x_i - x_j\right)^2 + \left(y_i - y_j\right)^2 + \left(z_i - z_j\right)^2} \geq \frac{d_{gi} + d_{gj}}{2} \tag{3.19}$$

where j from 1 to $i - 1$.

In Figure 3.9 the exposed grains can be identified by satisfying the following condition [13]:

$$Abs(H - z_i) < \frac{d_g}{2} \tag{3.20}$$

The protrusion height P_h of a given exposed grain, as shown in Figure 3.9, was defined by the following equation [13]:

$$P_h = z_i + \frac{d_g}{2} - H_b \tag{3.21}$$

where H_b is the bond surface height.

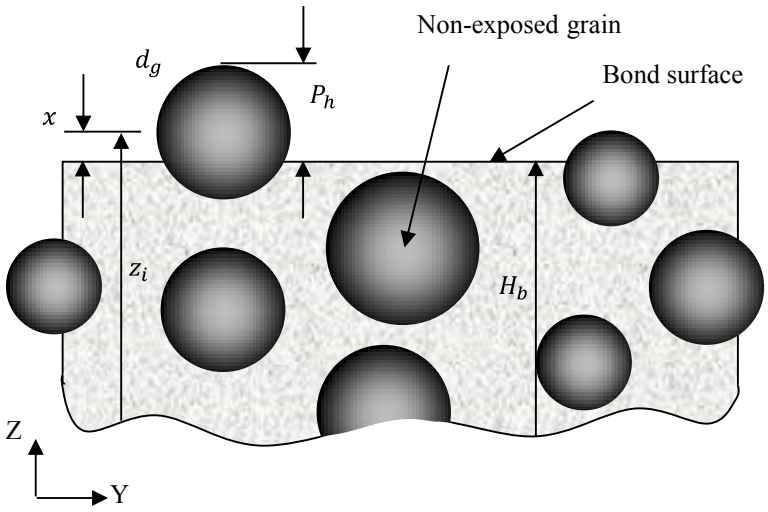

Figure 3.9 Scheme for identifying protruding abrasive grain [13].

Koshy *et al.* [13] concluded that the distribution of the grains' protrusion height in freshly dressed diamond wheel was uniform, whereas, inter-grain spacing between exposed grains conformed to a gamma distribution. The percentage of the projected area due to the protruding grains was found to be independent of the abrasive grit size.

3.4.2 Chen and Rowe model

Chen and Rowe [11] developed a model that took the dressing process into account. The topography model is influenced by the characteristics of the grinding wheel, the dressing diamond shape and the dressing conditions. Figure 3.10 shows the relationship between the input and the output of the dressing process.

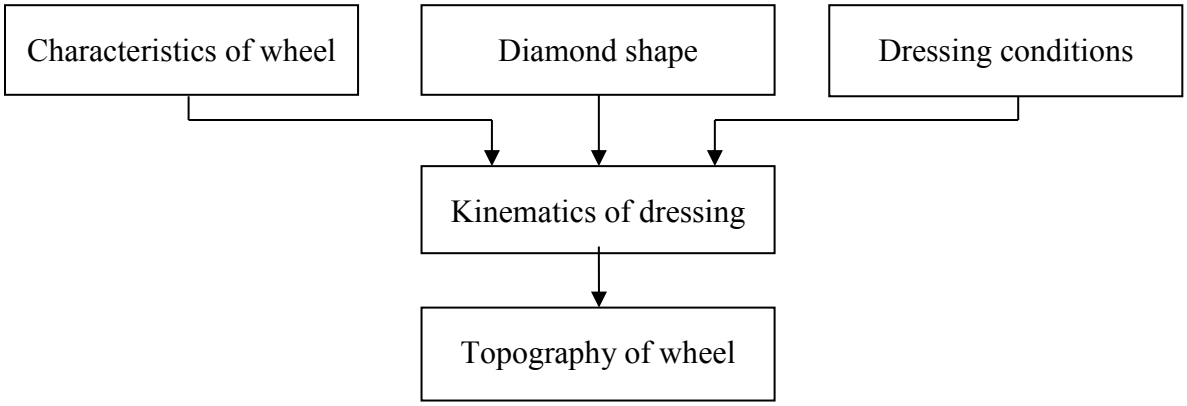

Figure 3.10 Relationships in a dressing process [11].

The grain size, the packing density of the grains in the grinding wheel and other parameters represent the grinding wheel characteristics. Chen and Rowe [11] assumed that the grinding wheel is composed of spherical grains with diameter of d_g, which are evenly sized and randomly distributed throughout the wheel volume. The grains are initially arranged using a simple cubic unit cell (SC). Subsequently, they are randomly rearranged. Each individual grain is located in the grinding wheel by the following matrix [11]:

$$[G_{i,j,k}] = \begin{bmatrix} G^x_{i,j,k} \\ G^y_{i,j,k} \\ G^z_{i,j,k} \end{bmatrix} = \begin{bmatrix} G^x_{0,0,0} + i\,\Delta x + R_x \\ G^y_{0,0,0} + j\,\Delta y + R_y \\ G^z_{0,0,0} + k\,\Delta z + R_z \end{bmatrix} \tag{3.22}$$

where the average spacing in x, y, and z directions are equals, i.e. $\Delta x = \Delta y = \Delta z = L$, since the spatial probability is assumed to be uniform. The total volume of the grains in one cell of SC is calculated by [11]:

$$V^{cub}_{g,SC} = \frac{1}{6}\pi {d_g}^3 \tag{3.23}$$

where M is the mesh size. The grain packing density V_g, determined by Equation (3.26) [2], is the ratio of the total volume of the grains in one cell to the whole volume of the cell, therefore [11]:

$$V_g = \frac{V_{g,SC}^{cub}}{V_{cell}^{cub}} = \frac{\pi \, {d_g}^3}{6 \, L^3} \tag{3.24}$$

$$L = \left(\frac{\pi {d_g}^3}{6V_g}\right)^{\frac{1}{3}} \tag{3.25}$$

$$V_g = 2(32 - S) \tag{3.26}$$

where S is the structure number of the grinding wheel and L is the inter-grain spacing (the space between the centers of adjacent grains). In Equation (3.22) R_x, R_y and R_z are random numbers which are generated between 0 and L by a computer program. The inter-grain spacing must be always greater than the grain diameter d_g, otherwise the grains will interfere with each other. Therefore, Chen and Rowe [11] made a rule for the rearrangement of the grains location process, which is the satisfaction of the following relation:

$$d\left(G_{i,j,k}, G_{i',j',k'}\right) > d_g \tag{3.27}$$

where $d(G_{i,j,k}, G_{i',j',k'})$ is the distance between the centers of adjacent grains.

Since grinding wheels are modified by the dressing process, Chen and Rowe [11] performed the dressing process on the grains after the randomization process to get a more realistic wheel topography model. A single point diamond dresser was used to cut the grinding wheel working surface. The dressing tool tip shape was assumed to be parabolic. The dressing tool passes helically over the surface of the grinding wheel. Chen and Rowe [11] considered two main mechanisms in the dressing operation, the ductile cutting and the grain fracture. Figure 3.11 shows that one grain may have several dressing

trace lines. In practice, these trace lines does not conform precisely the grain cutting surface after the dressing operation due to the fracture of the grains on grinding wheel, thus, Equation (3.28) represents the modified cutting surface of the grain [11].

$$z_g(x) = f(x) + h[\sin(\omega x + \alpha) + 1] \tag{3.28}$$

where $f(x)$ is the grain surface resulting from the diamond dressing path, ω is a random frequency, α is a random initial angle, and h is the amplitude value of the sine wave.

As shown in Figure 3.11, the amplitude value h controls the fracture size and it proportional to the intersection area between the diamond dressing path and the grain A_{int}, as well as the overlap ratio U_d. Therefore, the amplitude value of sine wave was defined as [11]:

$$h = k\frac{A_{int}U_d}{f_d} \tag{3.29}$$

where k is proportionality factor, which was set to 0.25 to give reasonable simulation results, and f_d is dressing lead as shown in Figure 3.11. In this model the intersection area A_{int} was calculated numerically.

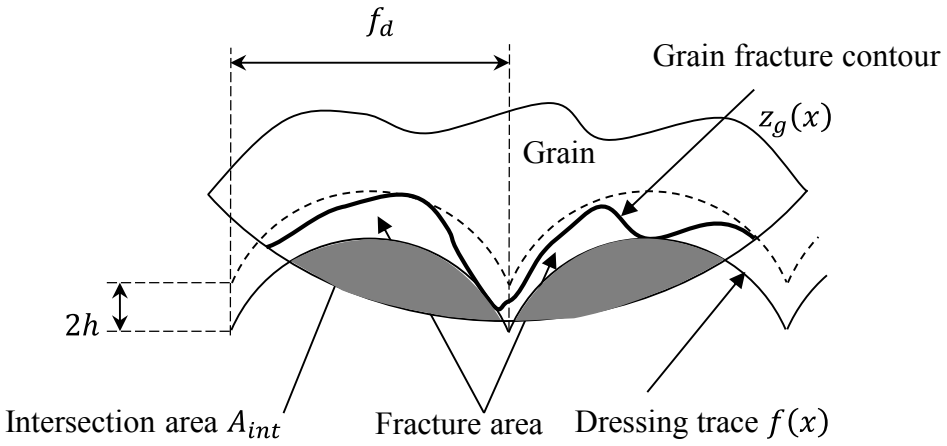

Figure 3.11 Cutting edges generated by dressing fracture [11].

3.5 Three dimensional topography models

In the 3D grinding wheel topography models the grinding wheel working surface is either experimentally or statistically characterized in detail to be employed in simulation of the effect of the dressing process of the grinding wheel topography, or to generate a simulated ground surface of the workpiece.

3.5.1 Hegeman model

Hegeman [14] has proposed a three-dimensional topography model that assumes the grains have an ellipsoidal shape. The ellipsoidal grain size and orientation are randomly changed. The grain shape function in the wheel global coordinate system is [14]:

$$z^{gr}(x,y) = r_g^z \sqrt{1 - \left(\frac{x - x_g^c}{r_g^x}\right)^2 - \left(\frac{y - y_g^c}{r_g^y}\right)^2} \tag{3.30}$$

where $\left(x_g^c, y_g^c, z_g^c = 0\right)$ is the location of the grain center, and r_g^x, r_g^y and r_g^z are the grain axis radii in x, y and z directions, respectively.

Hegeman [14] applied a dressing function to his model by generating a non-smooth surface on the grains. Since Equation (3.30) generates smooth ellipsoidal surfaces, Hegeman [14] defined a stochastic periodic function, Equation (3.31), to simulate the effect of dressing.

$$z^{fr}(x,y) = \cos(\hat{\omega}_x x + \hat{\alpha}_x) + \cos\left(\hat{\omega}_y y + \hat{\alpha}_y\right) \tag{3.31}$$

where $\hat{\omega}_x$, $\hat{\alpha}_x$, $\hat{\omega}_y$ and $\hat{\alpha}_y$ are random numbers. Figure 3.12 shows the results of the simulation of Hegeman's topography model without dressing. The wheel surface is located at $z = 0$. This model requires some parameters, which are listed in Table 3.1, that are experimentally determined.

Table 3.1 Required wheel parameters in Hegeman model.

Wheel parameter	Symbol	Experimental technique
Grain density per unit area	C_A	Scanning electron microscopy
Grain base radius	$r_g^x = r_g^y$	Confocal scanning optical microscopy
Grain protrusion height	r_g^z	Confocal scanning optical microscopy

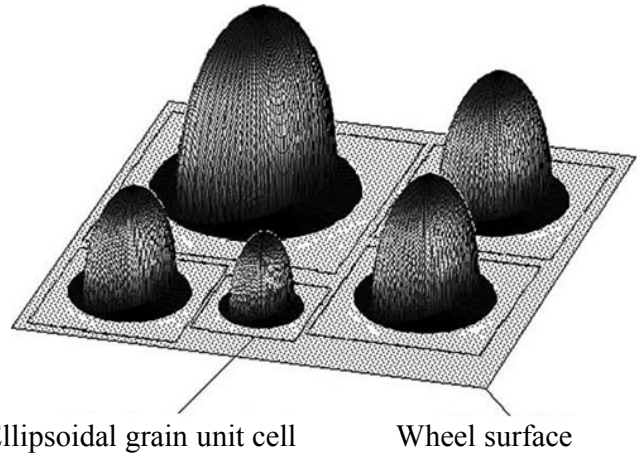

Figure 3.12 Schematic of Hegeman model approximation of the grinding wheel topography [10].

3.5.2 A framework for general 3D model by Doman

Doman *et al*. [10] constructed a framework for a general 3D topography model from a survey of the grinding wheel topography models prior 2005. Doman *et al*. [10] summarized the grinding topography model in a general modeling approach, as shown in Figure 3.13. The framework has two principle parts. The first part is the modeling of undressed grinding wheel topography, while the second part applies the dressing process to produce the final grinding wheel topography model.

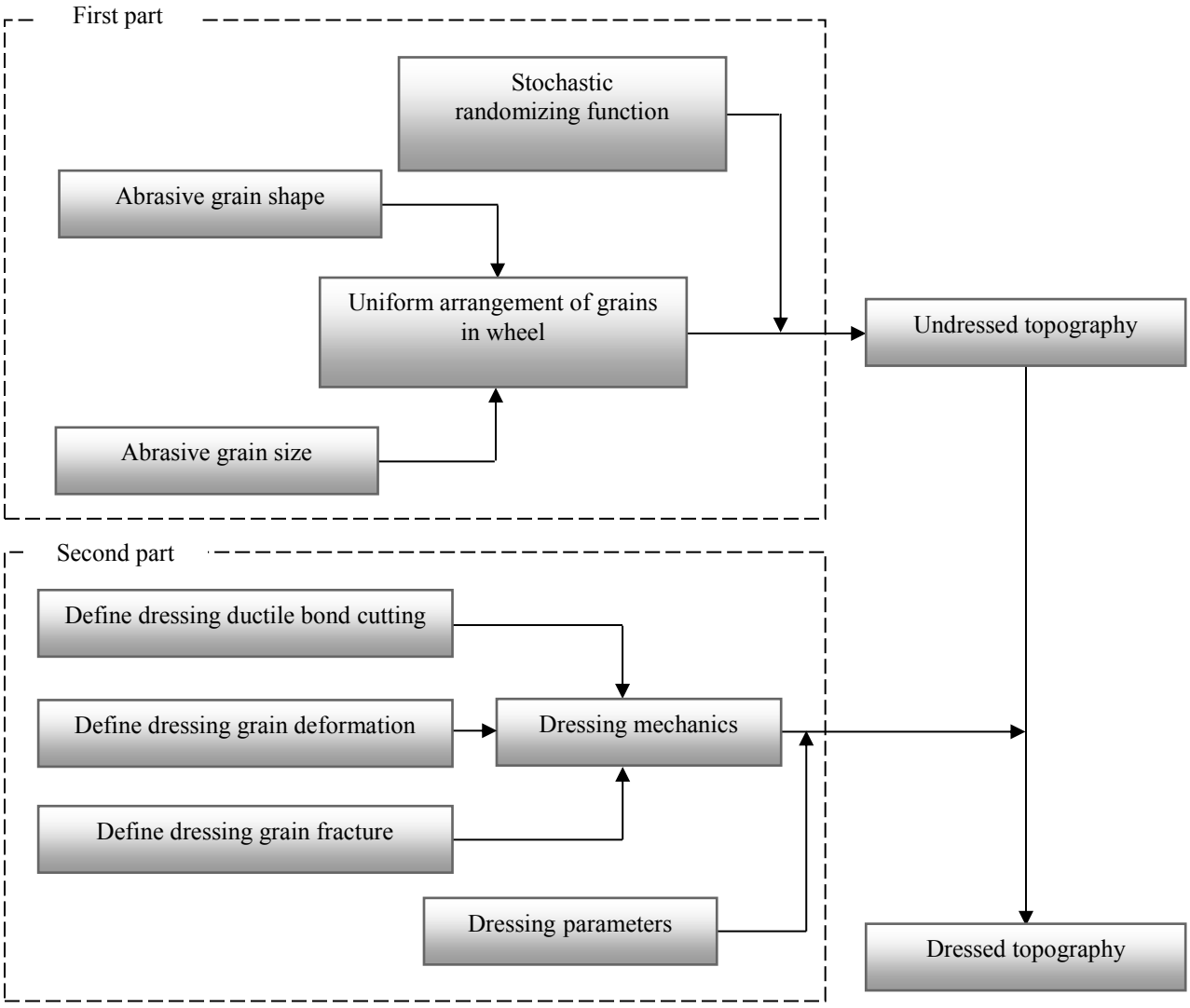

Figure 3.13 General 3D physical topography model approach [10].

In the first part of the framework the grains are randomly shaped, sized, and located. The abrasive grain shape, which is usually simplified by spherical, size, and location are set uniformly. Consequently, the stochastic randomizing function is applied to randomize the grains size and location. The resulting model is then ready for the dressing process.

The second part on the framework model consists of the dressing technique, which is a product of three major mechanisms. These mechanisms are grain fracture, ductile bond cutting, and grain deformation. All these mechanisms are affected by the dressing parameter, such as dressing tool shape, dressing depth, and dressing lead.

3.6 Grinding wheel surface measurement

Grinding wheel surface measurement methods were reviewed by Verkerk [16] including grain counting, profilometry, and a taper print method. In 1996 Lonardo *et. al* [38] also reviewed grinding wheel measurement techniques and classified the 3D surface measurement instrument to distinguish between contact and non-contact measuring methods.

3.6.1 Contact measuring methods

Surface measurement using a stylus, which has been used since 1927 [38] and is still the most widely used for the measurement of surface roughness, is a contact method. In this technique, a small force is applied by the stylus tip to ensure continuous contact between the stylus tip and the measured surface during the measurement procedure. In the surface measurement process using the stylus, the stylus tip travels across the surface and records the changes in the profile height of the surface. This process can be repeated in orthogonal directions to measure a surface in 3D (rastor scan procedure). Blunt and Ebdon [39] used a Somicronic Surfascan 3D stylus-based measuring instrument and Nguyen and Butler [40] used a Talyscan 150 stylus system to characterize the grinding wheel surface. The surface measurement process using a probe is also classified as a contact measuring method.

3.6.1.1 Xie *et al.* model

Xie *et al.* [15] introduced a measuring system that provides 3D wheel topography data. The system employed LH-65 coordinates measuring machine (CMM) to conduct the measurement of grain protrusion topography on the wheel surface. Figure 3.14 illustrates the scheme for the 3D measurement of the grains. The $4\,mm$ diameter spherical carbuncle probe touches the wheel surface circumference and records the coordinate system of each point. This procedure is repeated at each level of depth δ_y of wheel width (y-axis). Each measured point $P_i(x_i, z_i)$ is transformed to the polar coordinate $P_i\left(r_{p_i}, \theta_i\right)$ by the following equations [15]:

$$r_{p_i} = \sqrt{x_i{}^2 + z_i{}^2} \tag{3.32}$$

$$\theta_i = \tan\left(\frac{x_i}{z}\right) \tag{3.33}$$

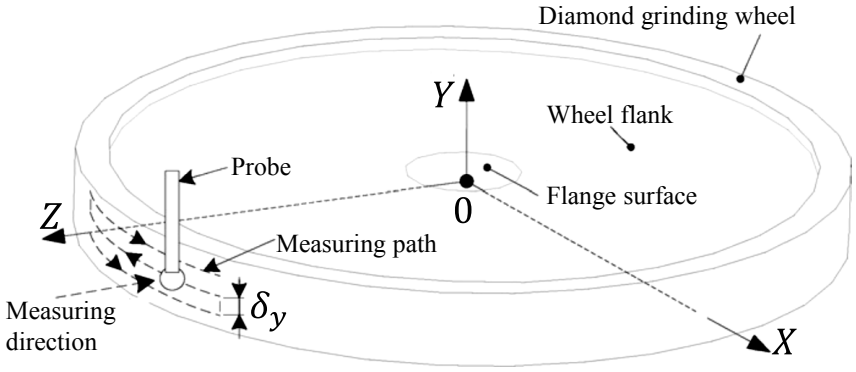

Figure 3.14 Scheme of 3D measuring of grain protrusion surface [15].

Figure 3.15 shows the measured profile. The mean radius of r_{p_0} used as a datum surface radius was given by [15]:

$$r_{p_0} = \frac{1}{n}\sum_{i=1}^{n} r_i \tag{3.34}$$

The measurements were converted to an arc length L_{r_i} and a protrusion height P_{h_i} using the following equations [15]:

$$L_{r_i} = r_{p_0}\,\theta_i \tag{3.35}$$

$$P_{h_i} = r_{p_i} - r_{p_0} \tag{3.36}$$

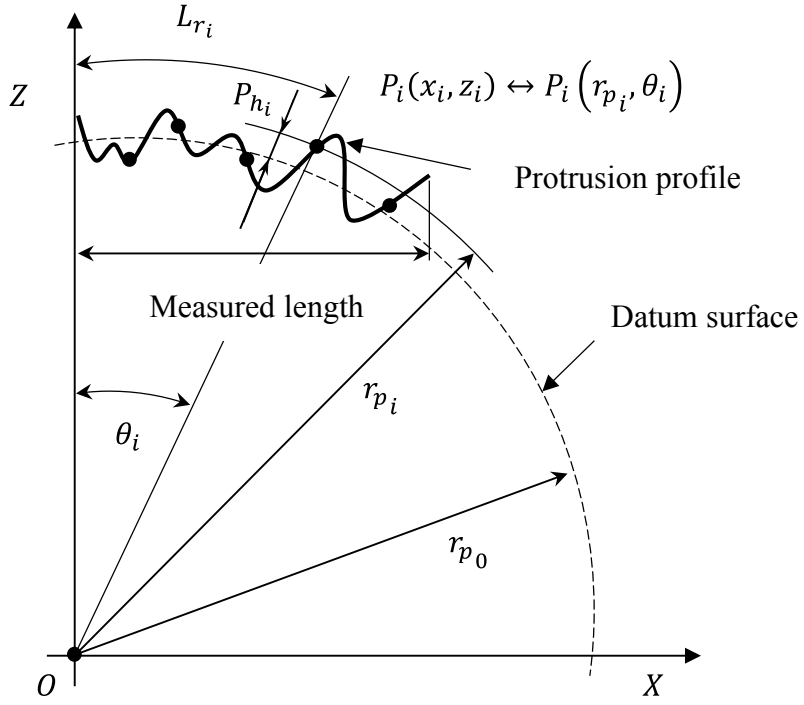

Figure 3.15 The geometrical mode of the grain protrusion profile.

Figure 3.16 shows the 3D grain protrusion topography on the wheels working surface. By enlarging the measured area of the grinding wheels work surface, more information about the grain protrusion distribution can be obtained.

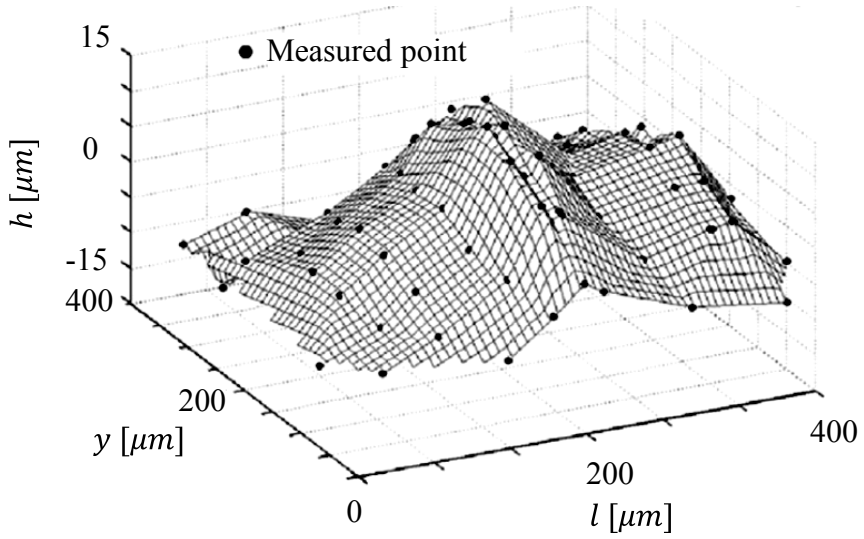

Figure 3.16 Grain protrusion topography on wheel working surface [15].

Due to the stylus and probe geometry, however, it is difficult to measure the small features that make up a grinding wheel surface; also the information of the measured surface at the deep peaks is not reachable. Therefore, the measurements were made directly on the outmost layers of the grinding wheel surface. Moreover, when increasing the measuring speed (scan speed) the stylus tends to lose the contact with the measured surface resulting in low pass filtering [38]. In addition, using the stylus or probe on a very rough hard surfaces such as grinding wheel surfaces can cause accelerated wear to the stylus [36].

3.6.2 Non-contact measuring methods

Non-contact methods seem to be more suitable for the measurement of the grinding wheel topography [41], because in contact methods the measurement result is greatly influenced by the measuring tool geometry as well as the measurement mechanism [38].

Several attempts of non-contact methods of grinding wheel topography have been conducted; these methods can be classified as non-optical or optical techniques. The non-optical non-contact techniques include Scanning Electron Microscopes (SEM) and Acoustic Emission (AE) sensors.

Matsuno *et al.* [42] used a scanning electronic microscope to generate a stereographic image of the grinding wheel surface; however, this technique requires a very small sample size ($2 \times 2\ mm$), which may not be sufficient to characterize an entire grinding wheel. The stereographic image of the grinding wheel surface was converted into contour plots allowing cutting edge density at different level of wheel surface depth to be observed.

Syoji *et al.* [36] used a pair of scanning electronic microscope stereo photographs to generate the grinding wheel topography in three dimensions, by comparing photographs taken simultaneously from different angles. Information about the third dimension (image depth) can then be obtained through a triangulation process.

Weingaertner and Boaron [43] used an acoustic emission sensor mounted on a dressing tool to count the number of cutting edges on a grinding wheel. This system could map the location of cutting edges but could not directly determine the cutting edge size or protrusion height. Acoustic emission was also used by Oliveira [44] to define the wear and surface location of the grinding wheel.

Optical non-contact approaches include conventional optical microscopes, auto-focusing systems, white light interferometer and binocular stereovision. Lachance *et al*. [45] used a conventional optical microscope with inline lighting mounted on a grinding machine to identify cutting edges with wear flats between grinding cycles but could not identify sharp cutting edges or the protrusion height of cutting edges. Inasaki [46] and Xie *et al*. [47] used an auto-focusing system that relied on the fact that the intensity of light reflected from an object that is in focus is higher than when it is out of focus. Thus the in-focus distance can be used to determine the height of a cutting edge. Yan *et al*. [48] used a white light interferometer to measure a sample of a grinding wheel. In this technique the depth of an object is determined by examining the interference pattern produced when white light from a single source is reflected off the desired object and a mobile reference object.

Zhang *et al*. [49] used binocular stereovision to measure the grinding wheel topography. In this system two images of the grinding wheel are taken from different locations and the principles of triangulation are used to determine the height of a cutting edge. It is worth mentioning that all of the non-contact techniques reviewed, with the exceptions of the work by Weingaertner and Boaron [43] and Lachance *et. al* [45], have small measurement volumes and could only measure very small grinding wheels or required the destructive preparation of larger grinding wheels limiting their practical application.

3.7 Uncut chip thickness and contact length models

In grinding, as in all machining methods, the material is removed in a chip formation process, but at a much finer scale. Due to the stochastic nature of grinding wheels, it is difficult to calculate fundamental geometric properties of grinding such as the uncut chip

thickness and contact length for individual grains. These quantities are essential in order to accurately predict forces, power, temperature, and workpiece surface roughness in grinding.

There has been extensive research conducted into the modeling and simulation of grinding wheel surfaces. Gong *et al.* and Nguyeb *et al.* [50, 51] conducted work into the simulation of the interaction between the grinding wheel and the workpiece to study the result on the workpiece surface roughness or on the determination of the active grains. The results of this research, however, has not translated into estimates of the uncut chip thicknesses and contact length partly due to the lack of grinding metal removal models. However, work has been conducted to estimate the uncut chip thickness and contact length either analytically or experimentally.

In 1992, Zhang *et al.* [52] proposed a formula to predict the contact length based on the cutting force, elastic deformation and one empirical constant. Qi *et al.* [53] modified an orthogonal contact length model based on Qi *et al.* [54] and concluded that the magnitude of the real contact length is up to three times that of the geometric contact length. The work was conducted by replacing the force variable in the orthogonal contact length model by an empirical formula and specific grinding power that can be easily obtained. In 2011 a new methodology for the estimation of the actual contact length in grinding was proposed by Inigo *et al.* [55]. In their proposal, they have attached thermo-couples to the workpiece (100 μm below the work surface) and measured the changes in the temperature during grinding. The temperature was measured versus time and subsequently converted to the contact length.

For the uncut chip thickness, few works were found in the literature review to determine the uncut chip thickness. Work has been done by Brough *et al.* [56] to analytically re-examine and develop the uncut chip model, which was developed by Reichenbach *et al.* [57], by taking into account the active cutting-edge distribution. Zhang *et al.* [58] used a Carbon Nanotube grinding wheel (CNT) to experimentally measure the chip thickness of the produced chip. They concluded that the chips were difficult to measure due to the chip sizes and agglomeration despite the use of high magnification up to $7.2 \times 10^6\ x$.

In 1974 Brecker *et al*. [59] developed a dynamic method to determine the number of grains per unit area that not only appear in the grinding wheel surface, but also participate in the cutting operation. A thin workpiece, that ensured only one grain was in contact at a given time, was mounted on a very high natural frequency dynamometer to measure the normal force. The number of chips produced in a given time was determined by counting the number of force peaks from the plot.

Throughout the previous research, however, the grains were assumed to have even distribution, size and protrusion height. As a result of these assumptions, the grain would be in contact with the workpiece from point *B* to point *A* in Figure 3.17.

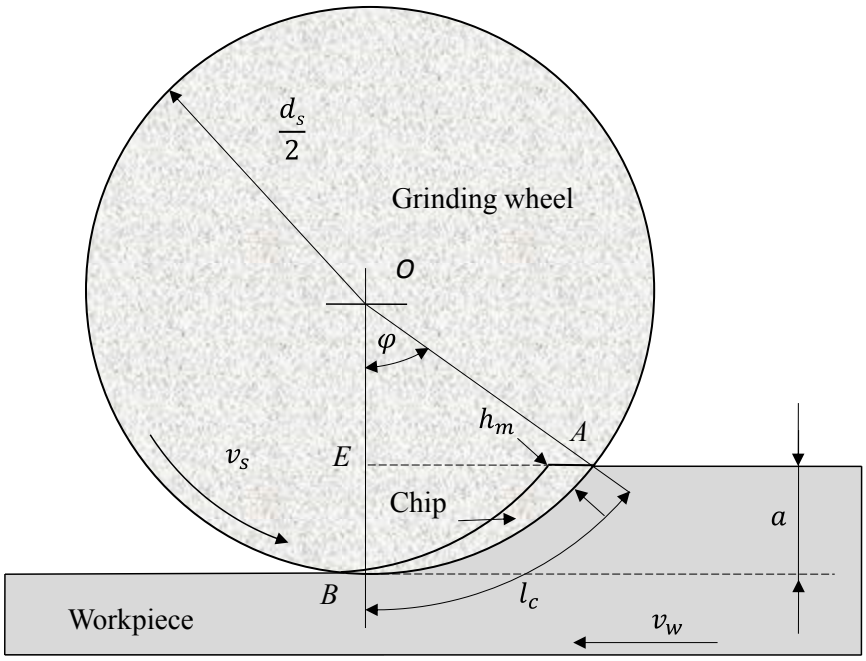

Figure 3.17 Surface grinding.

3.8 Summary

This chapter reviewed some of the research conducted into the modeling of grinding wheel topography and the interaction between the abrasive grains based on simulation techniques. Although some works have succeeded in describing the wheel surface and

predicting the machined surface roughness, the results have not been extended to describe the chip geometry produced by each individual abrasive grain that is exposed on the wheel surface.

Although the reviewed non-contact methods seem to be more suitable for the measurement of the grinding wheel topography, all the non-contact techniques (with the exceptions of the work by Weingaertner and Boaron [43] and Lachance *et al*. [45]) have small measurement volumes. Methods such as scanning electronic microscope may not be sufficient to characterize an entire grinding wheel. These methods measure only very small grinding wheels or require the destructive preparation of larger grinding wheels, limiting their practical application.

CHAPTER 4. 2D METAL REMOVAL SIMULATION FOR GRINDING

4.1 Introduction

Due to the complexity of the grinding wheel topography and the interaction between the abrasive grains and the workpiece during grinding, the analytical models tend to produce inaccurate estimates of the uncut chip thickness and contact length. The purpose of this chapter is to develop a 2D simulation-based stochastic method to more accurately calculate the instantaneous uncut chip thickness and contact length, and investigate the effect of the grain size, grain spacing and grain protrusion height distribution on the calculation of the uncut chip thickness and contact length. A subsequent 3D model was built on this 2D model.

4.2 The simulation theory

The modified 2D z-map technique is based on the work of Kim [60]. Kim's method was selected because it is a relatively straightforward method to implement, computationally efficient and easily scalable to 3D.

4.2.1 z-map technique

The z-map technique is used for performing simulation and verification in cutting milling operations to evaluate the workpiece surface roughness [61]. In this technique the workpiece is modeled as a set of discrete columns in a Cartesian space as shown in Figure 4.1. The height of each z-column is stored as a number in an array called the z-map. The simulation is performed by intersecting the lines, which are defined by the z-columns, with the geometry tool motions. After each intersection the value in the z-map is compared with the intersection result. If the intersection result is smaller than the z-map value, the value in the z-map is replaced by the intersection value. The z-map can be displayed to visually inspect the results.

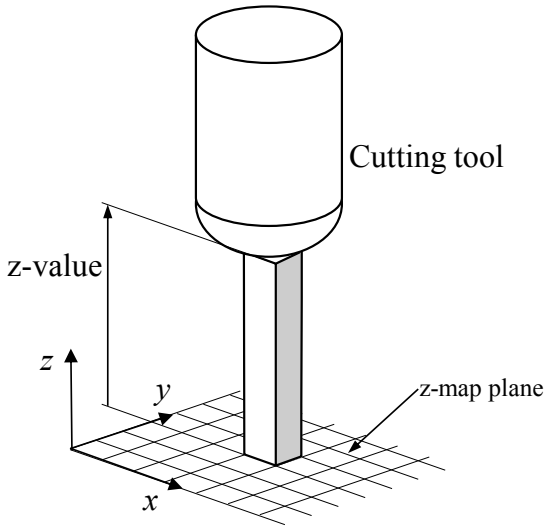

Figure 4.1 The z-map technique.

4.2.2 Modified 2D z-map technique

A 2D version of the z-map technique can be used for the simulation of metal removal in grinding. In the modified 2D z-map technique, the workpiece material is represented by a

set of evenly spaced vertical line segments as shown in Figure 4.2. The length of the line segments represents the workpiece height while the number of line segments times the space between adjacent line segments represents the workpiece length. The accuracy of the workpiece representation is determined by the spacing of the line segments or by the line segment density σ_{ls}, which is the number of line segments per unit length. Smaller spacing will result in a more accurate model, whereas larger spacing will result in a less accurate model; in other words, the higher the line segment density the more accurate the model. The line segment density can be calculated as follows:

$$\sigma_{ls} = \frac{N_{ls}}{l_{wp}} \tag{4.1}$$

where N_{ls} is the number of line segments and l_{wp} is the workpiece length.

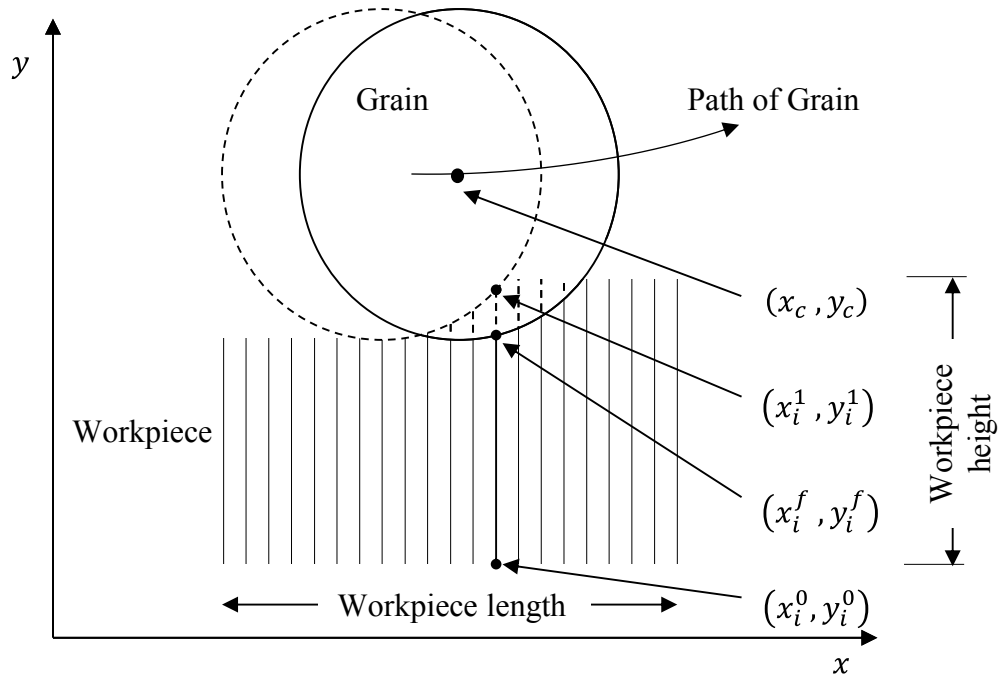

Figure 4.2 The modified 2D z-map technique for grinding.

Each line segment is represented by a one-dimensional parametric equation. The parametric equation uses a length parameter called f.

$$x_i^f = x_i^0 = x_i^1 \tag{4.2}$$

$$y_i^f = y_i^0 + f(y_i^1 - y_i^0) \tag{4.3}$$

where $0 \leq f \leq 1$

4.2.3 Simulation of grain motion

The grain geometry has often been approximated by spheres [11, 62], cones [63], ellipsoids [14, 24], or has been generated from modified basic geometries, such as octahedrons, cuboids, and tetrahedrons [64]. In this simulation the abrasive grains are assumed to have a spherical shape; therefore, circles will represent the abrasive grains in a 2D model as shown in Figure 4.2. Note, however, that in this technique the grains can easily have different shapes.

The grains travel along a trochoidal path, which is a combination of a circular rotation and a linear translation as expressed in Equation (4.4) and (4.5). These equation are used to define the grain center (x_{cj}, y_{cj}) at time t:

$$x_{cj}(t) = v_w t + \left(\frac{d_s - d_g}{2}\right) cos\left(\frac{t \times v_s}{\left(\frac{d_s - d_g}{2}\right)} + \beta_j\right) + x_w \tag{4.4}$$

$$y_{cj}(t) = \left(\frac{d_s - d_g}{2}\right) sin\left(\frac{t \times v_s}{\left(\frac{d_s - d\_g}{2}\right)} + \beta_j\right) + y_w \tag{4.5}$$

where j is the grain index, v_w is the workpiece speed, v_s is the cutting speed, d_g is the grain diameter, d_s is the grinding wheel diameter, x_w and y_w represent the location of the

grinding wheel center at initial time ($t = 0\ sec$) and β_j represents the grain angle which is measured at initial time ($t = 0$ sec) as shown in Figure 4.3. The grain angle β_j for each grain is calculated by the following equation:

$$\beta_j = \sum_{j=0}^{i} \frac{L_j}{\left(\frac{d_s - d_g}{2}\right)} \tag{4.6}$$

where L_j is the grain inter-spacing, which is the space between the centers of adjacent grains. The term ($v_w t$) in Equation (4.4) represents the feed motion, while the term $\left\{\frac{d_s - d_g}{2} cos\left(\frac{t \times v_s}{\frac{d_s - d_g}{2}}\right)\right\}$ represents the x-component of the rotation of the grain around the wheel center. The y-component of the rotation of the grain around the wheel center is determined by the term $\left\{\frac{d_s - d_g}{2} sin\left(\frac{t \times v_s}{\frac{d_s - d_g}{2}}\right)\right\}$ in Equation (4.5). In this simulation technique, the relative feed motion is accomplished by a wheel translation while the workpiece stays stationary. The initial location of the grinding wheel center (x_w, y_w) shown in Figure 4.3 is defined by the following equations:

$$x_w = -\sqrt{a d_s - a^2} \tag{4.7}$$

$$y_w = l_{wp} + \frac{ds}{2} - a \tag{4.8}$$

where l_{wp} is the workpiece height.

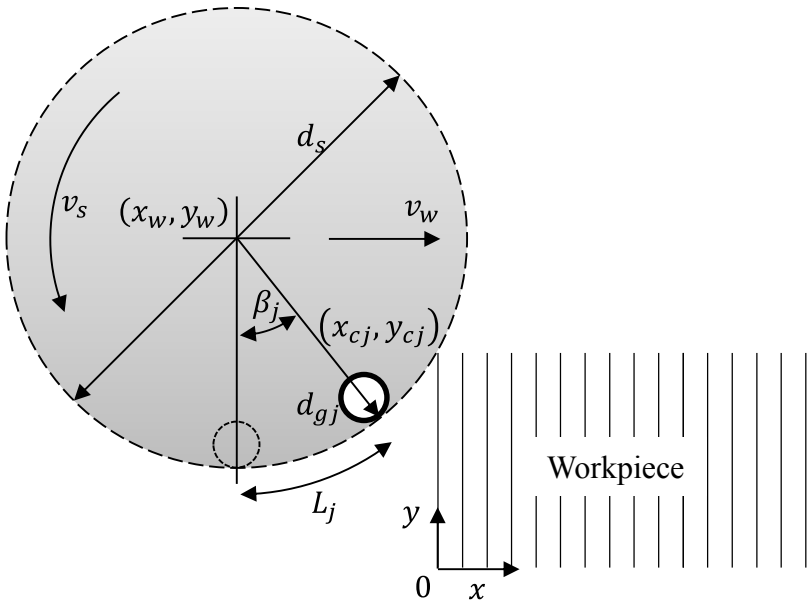

Figure 4.3 The initial location of the grinding wheel.

In order to apply the simulation of the grain motion, time was divided into discrete, equal time steps δt. Thus, the grain motion starts at time $t = 0\ sec$ and the material removal simulation is applied for this moment. Then each grain will be moved intermittently using Equation (4.4) and Equation (4.5) to the new location with respect to time $(0 + \delta t)$ and $(0 + \delta t + \delta t)$ and so on. The discrete-time interval is set as following:

$$t = [\ 0\ , \delta t\ , 2\delta t\ , 3\delta t\ , 4\delta t\ , \dots\ ] \tag{4.9}$$

The time step δt is determined by the following equation:

$$\delta t = \frac{dt_f}{\sigma_{ls}\ \ v_x} \tag{4.10}$$

where dt_f is the time step factor. When the time step factor is 1 ($dt_f = 1$), the time step will be enough for each grain to travel a distance equal to the space between each two adjacent line segments. Full engagement between the grinding wheel and the workpiece

is achieved when the center of the grinding wheel (x_w, y_w) aligns with the first point on the workpiece in x-direction. The time required for full engagement can be calculated by the following equation:

$$t = \frac{\sqrt{a\ d_s + a^2}}{v_w} \tag{4.11}$$

4.3 Metal removal

Intersecting the circle with the line segments at discrete time intervals simulates metal removal. The portions of the line segments that are inside the circle (dashed lines in Figure 4.2) are removed by adjusting the length of the line segments. Equation (4.12) describes the circle which intersects the line segments:

$$(y - y_c)^2 + (x - x_c)^2 = R^2 \tag{4.12}$$

where R is the circle radius. To define the intersection point between the circle and each line segment, Equations (4.2) and (4.3) are substituted into Equation (4.12) to obtain Equation (4.13):

$$\left(y_i^f\right)^2 + 2y_c\ y_i^f + k = 0 \tag{4.13}$$

where:

$$k = {y_c}^2 + \left(x_i^f - x_c\right)^2 - R^2 \tag{4.14}$$

To determine y_i^f, Equation (4.13) is rewritten in the quadratic equation form as following:

$$y_i^f = \frac{-2y_c \pm \sqrt{(2y_c)^2 - 4k}}{2} \tag{4.15}$$

The length parameter f is then found by rearranging Equation (4.3) in the following manner:

$$f = \frac{y_i^1 - y_i^f}{y_i^1 - y_i^0} \tag{4.16}$$

Since the line segment will be cut by the lower half of the circle, only the minus sign $(-)$ in the Equation (4.15) is considered. Note that the length parameter f can be one of the following cases:

1. $f = a + b\sqrt{-1}$ when there is no intersection point between the line segment and the circle.
2. $f < 0$, or $f > 1$ when the intersection point is outside the range of intersect.
3. $0 \leq f \leq 1$ when the intersection point exists on the line segment.

Once the length parameter f is obtained with a value of $0 \leq f \leq 1$ the cut portion is removed by substituting the value of y_i^1 with the value of y_i^f that is obtained from Equation (4.15).

In order to reduce the time required for the simulation, only the line segments that are in the interval $[x_c - R\ ,\ x_c + R\ ]$ are checked for the cutting process at each discrete time step for each grain. Using this formulation it is easy to control the accuracy of the simulation by specifying the line segment density and the time step.

4.4 Uncut chip thickness and contact length calculation

Figure 4.4 illustrates the simulated uncut chip geometry. The dimensions in the vertical direction are exaggerated in order to emphasize the chip geometry and the grain is shrunk to illustrate the position of the grain on the chip. The dashed lines are the segments that are removed by the grain. The coordinate system for the top point of the cut line segment is (x_i', y_i') and for the bottom line is (x_i, y_i). The uncut chip thickness can be defined as the shortest distance between the chip vertex (point l in Figure 4.4) and the chip bottom

line (from point m_v to point n in Figure 4.4). The following equation is used to calculate the uncut chip thickness:

$$h_m = \min_{i=m_v \to n} \left(\sqrt{(x_l - x_i)^2 + (y_l - y_i)^2} \right) \tag{4.17}$$

In Figure 4.4 the distance between point l and point m_a is referred to as the actual uncut chip thickness, which can be approximated by the distance between point l and point m_v. The distance between point l and point m_v is referred to as the vertical uncut chip thickness and is calculated by Equation (4.18):

$$h_{mv} = y_l - y_m \tag{4.18}$$

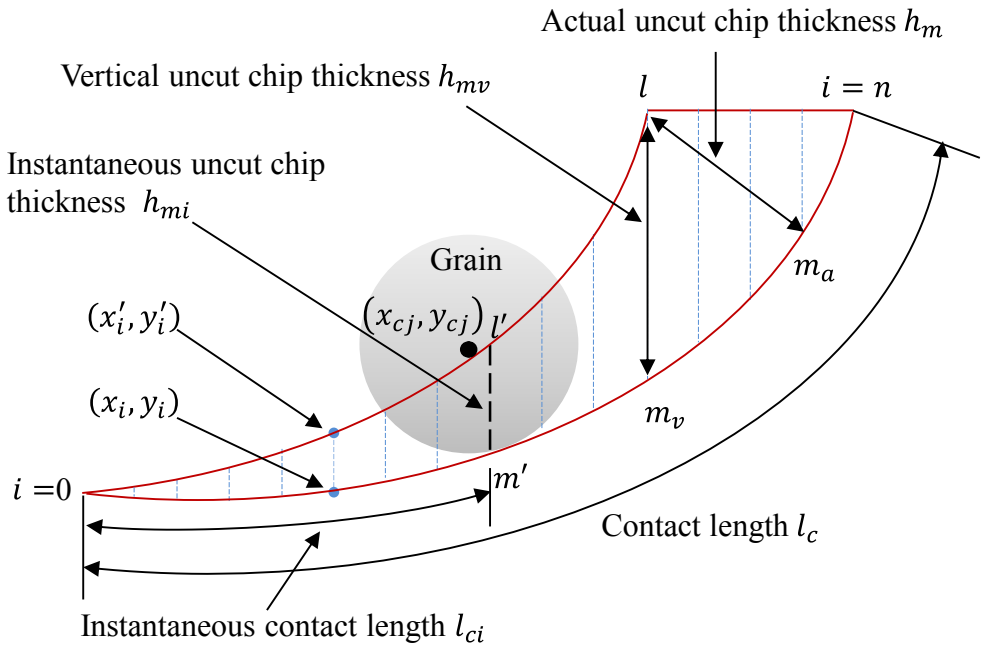

Figure 4.4 The uncut chip thickness and contact length on the simulated chip.

The comparison between the actual and vertical uncut chip thickness will be presented in the simulation accuracy section.

For the contact length calculation, Equation (4.19) is used to define the summation of the distances between the bottom points (x_i, y_i) of adjacent cut line segment.

$$l_c = \sum_{i=1}^{n} \sqrt{(x_{i-1} - x_i)^2 + (y_{i-1} - y_i)^2} \tag{4.19}$$

During the progress of the cutting process the instantaneous uncut chip thickness and the instantaneous contact length, (see Figure 4.4), can be calculated by Equation (3.14) and Equation (4.19), respectively, where $m = m'$ and $l = l'$.

The chip can also have more complex shapes as shown Figure 4.5. This shape can be generated when two traces or paths of successive active grains overlap causing the chip to have multiple cusps. To avoid incorrectly calculating the maximum uncut chip thickness, the maximum uncut chip thickness is calculated as the maximum value of the instantaneous uncut chip thickness at each time step, as shown in the following equation:

$$h_m = \max(h_{m_k}) \ , \ \ k = 0 \rightarrow n \tag{4.20}$$

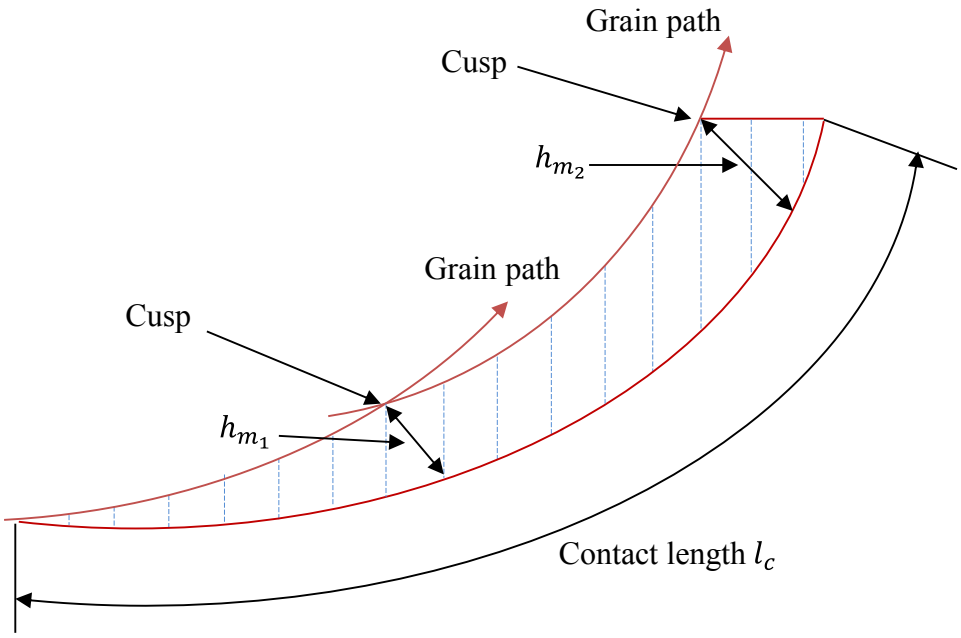

Figure 4.5 Different shape of the simulated cut chip.

4.5 The grinding wheel models

The proposed simulator was used to calculate the uncut chip thickness and contact lengths for two types of models of a standard grinding wheel. The first model type, referred to as the constant value model, assumes a constant grain size, grain spacing and grain protrusion height. This model was the benchmark and contains the same assumptions inherent in the analytical approach described in Section 2.5. The second model type, referred to as the stochastic model, assumes that the grain size, grain spacing and grain protrusion height have a stochastic distribution. Four models, which are different versions of the stochastic model, were implemented in order to identify the individual effects of stochastic grain size, grain spacing, and grain protrusion height on both the uncut chip thickness and contact length. These four models are referred to as the stochastic grain size model ("Stochastic dg") when only grain spacing and grain protrusion height are constant, stochastic spacing model ("Stochastic L") when only grain size and grain protrusion height are constant, stochastic protrusion height model ("Stochastic Hg") when only grain size and grain spacing are constant and the full stochastic model ("All stochastic") when grain size, grain spacing and grain protrusion height are stochastically distributed.

4.5.1 Constant value model

In the constant value model the information from the wheel marking system is used to determine the average grain diameter and the average spacing. All cutting edges in this model are assumed to protrude from the grinding wheel peripheral the same distance. A wheel with a nominal mesh size or (grit number) of 60 and structure number of 8 was used in this model and the stochastic model. The marking system of the grinding wheel was WR-A-60-J5-V1. This type of wheel is typically used for surface grinding steels to a medium surface finish.

Equation (4.21) is used to define the abrasive grain size for a given mesh [2]:

$$d_g = 15.2\, M^{-1} \tag{4.21}$$

where M is the mesh number. Equation (4.22) provides an empirical relationship between the grain volume fraction (packing density) and the structure number [2]:

$$V_g = 0.02(32 - S) \tag{4.22}$$

where S is the structure number. Figure 4.6 illustrates the constant value model. Assuming the packing density in 3D is the same in 2D, the grain spacing and the number of grains can be defined in the following manner. The packing density ρ is the area of the all grains to the area of the grinding wheel, as expressed in the following relation:

$$\rho = \frac{n\, A_{grain}}{A_{wheel}} = \frac{n\, \frac{\pi}{4}\, {d_g}^2}{\left(\frac{\pi}{4}{d_s}^2 - \frac{\pi}{4}\left(d_s - 2d_g\right)^2\right)} \tag{4.23}$$

The number of grains is then:

$$n = \frac{\rho\, \left(ds^2 - \left(d_s - 2d_g\right)^2\right)}{{d_g}^2} \tag{4.24}$$

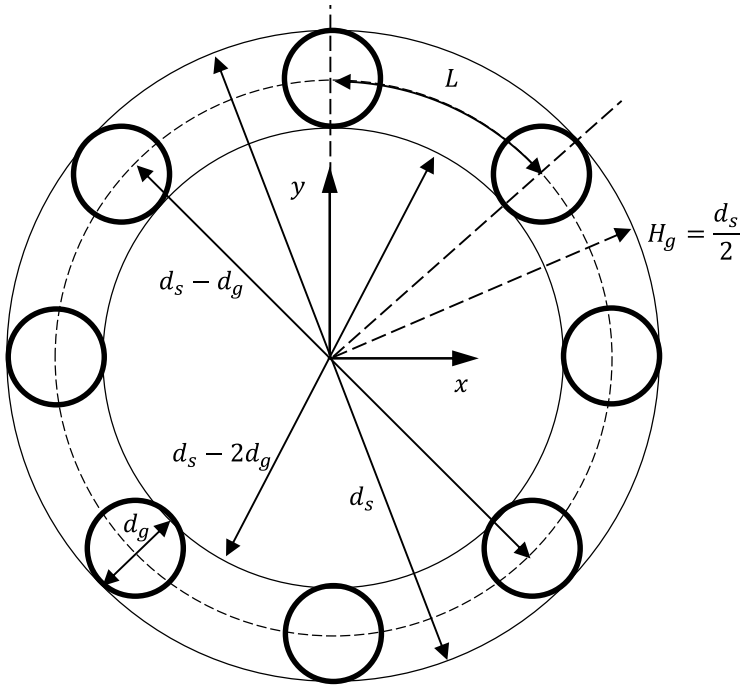

Figure 4.6 2D Constant value model.

Given the number of grains in the wheel model, the grain spacing can be calculated using the following equation:

$$L = \frac{\pi \left(d_s - d_g\right)}{n} \tag{4.25}$$

According to the aforementioned equations (from Equation (4.21) to Equation (4.25)), the constant model for the grinding wheel, which has a grit number of 60 and structure number of 8, has the parameters that are listed in Table 4.1

Table 4.1 Grinding wheel constant model parameters.

Parameter	value
Wheel diameter	$200\ mm$
Number of grains	$1515\ grains$
Grain diameter	$0.253\ mm$
Grain spacing	$0.415\ mm$
Grain protrusion height	$100\ mm$

4.5.2 Stochastic models

Stochastic models of grinding wheel generally consider the grain size, spacing and protrusion height. The stochastic model, which is used in this simulation, is a modified version of that proposed by Koshy *et al*. [13].

In the manufacture of grinding wheels, the distribution of grain sizes for a given nominal grain size usually takes the form of a normal distribution [12, 30]. A standard grit number is defined in terms of grain sizes corresponding to five sieves [2]. For example, grit number 60 involves abrasive grains caught on sieves number 46, 54, 60, 70, and 80. Using Equation (4.21) and grit number 80, 60 and 46 the minimum (d_{g_min}), average (d_g) and maximum (d_{g_max}) grain sizes were calculated, respectively. The standard deviation of the grain diameter was defined as follows:

$$\sigma = \frac{d_{g\_max} - d_{g\_min}}{6} \tag{4.26}$$

The protrusion height H_g is the distance that a cutting edge protrudes from the center of the grinding wheel as shown in Figure 4.7. Researchers are somewhat divided on whether the protrusion height is a normal distribution or a uniform distribution [13]. In this work a uniform distribution with the following characteristics was used:

$$\frac{d_s}{2} < H_g < \frac{d_s}{2} + 0.1 d_g \tag{4.27}$$

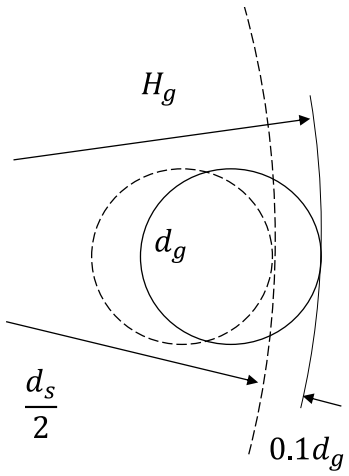

Figure 4.7 Grain height arrangement.

Based on experimental results, Koshy *et al*. [13] concluded that the grain spacing conforms to a gamma distribution. Thus, a gamma distribution with minimum and maximum values of grain spacing that results in a mean grain spacing of $0.415\ mm$ was used in the stochastic model.

For simplification purpose, the stochastic models were made in a separate program from the simulation program. The grinding wheel stochastic models were then provided as a pre-constructed array in the grinding simulation program. In the wheel model array, each grain is specified by its size, spacing and protrusion height. A function was used to generate random numbers between 0 and 1 for each stochastic model, taking into account whether the histogram of the generated numbers conform to a normal distribution, gamma distribution or uniform distribution. The parameters of the stochastic models are listed in Table 4.2.

Figure 4.8, Figure 4.9 and Figure 4.10 plot the histogram distributions of the grain size, grain spacing and grain protrusion height, respectively, for each stochastic model.

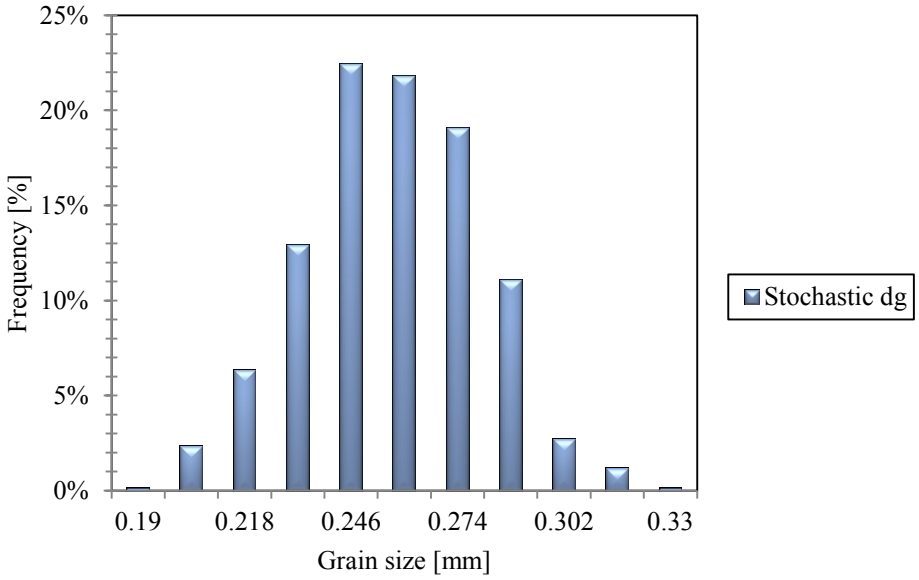

Figure 4.8 Grain size histogram (Stochastic dg model).

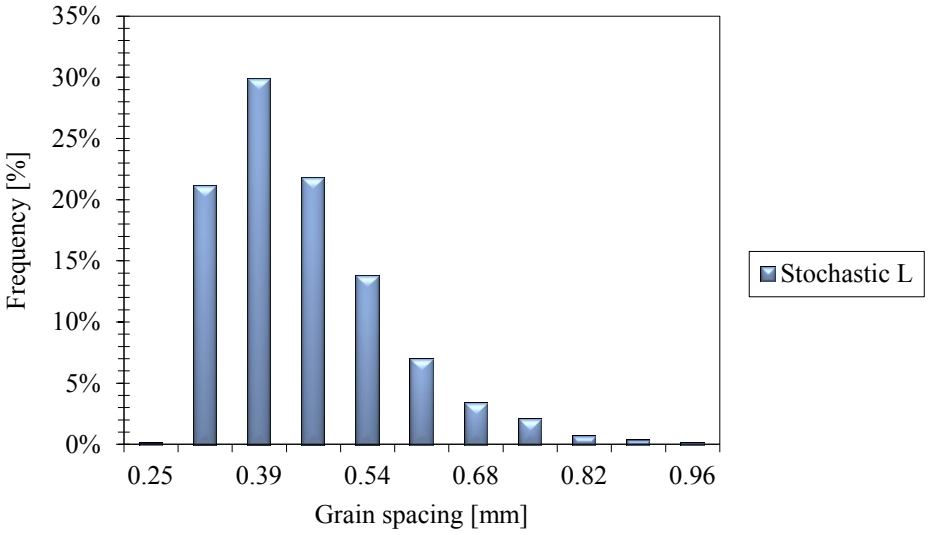

Figure 4.9 Grain spacing histogram (Stochastic L model).

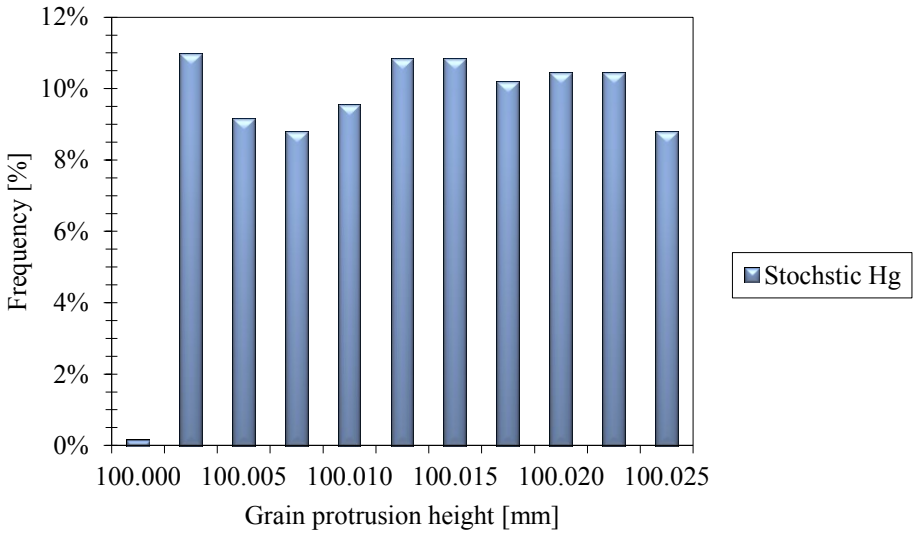

Figure 4.10 Grain protrusion histogram (Stochastic Hg model).

Table 4.2 Grinding wheel stochastic models parameters.

Model	Parameter	value
Stochastic dg	Number of grains	1515 grains
	Grain diameter	Stochastic
	Grain spacing	0.415 mm
	Grain protrusion height	100 mm
Stochastic L	Number of grains	1515 grains
	Grain diameter	0.253 mm
	Grain spacing	Stochastic
	Grain protrusion height	100 mm
Stochastic Hg	Number of grains	1515 grains
	Grain diameter	0.253 mm
	Grain spacing	0.415 mm
	Grain protrusion height	Stochastic

4.6 Visualization and resolution assessment

4.6.1 Visualization of metal removal

To avoid errors, the simulation required visual monitoring to verify simulation of the grains' movement and the simulation of material removal. Figure 4.11 shows a sample visualization of the grinding simulation. This figure shows that the simulation is working as expected. The grain size and spacing in the wheel model used in this test were exaggerated. This model was specially constructed for this test in order to emphasize the grain movement and cutting simulation. In this test the grain color changes to green as soon as it enters the cutting zone area and changes back to blue as soon as it leaves the cutting zone. Line segments are colored orange, they are re-plotted when their length are adjusted by the cutting simulation.

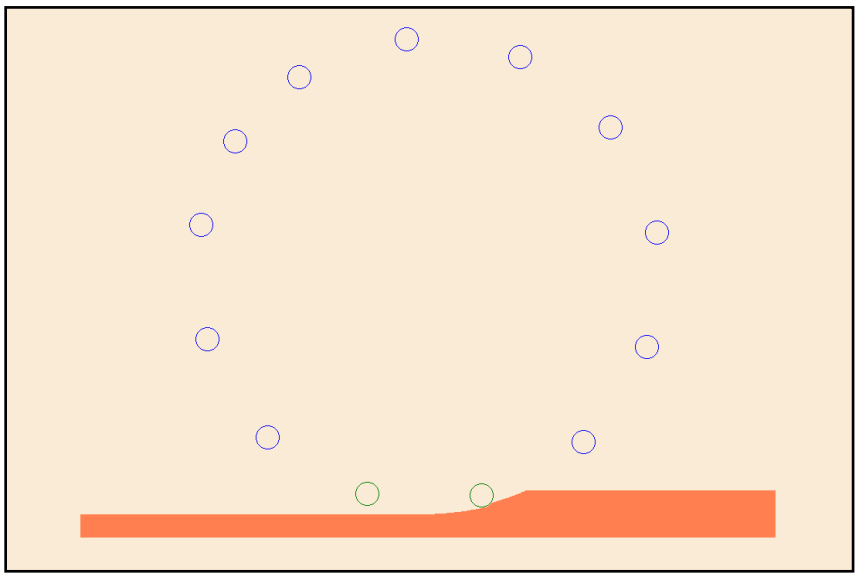

Figure 4.11 The simulation program test picture.

4.6.2 Effect of line segment density and time step factor on accuracy and solution time

The accuracy of the result is controlled by the line segment density σ_{ls} and the time step factor dt_f. As σ_{ls} increases and/or dt_f decreases the simulation is more realistic and the result is more accurate; however, the simulation takes much more time. Figure 4.12 plots the line segment density versus time required for a single grain to finish one complete pass through the workpiece (cutting zone area) with a time step factor $dt_f = 1$. The result shows that the running time increases very rapidly as the line segment density increases.

In order to select the optimum values of line segment density σ_{ls} and the time step factor dt_f , the simulation program was run for the constant value model of the grinding wheel at different values of line segment density and time step.

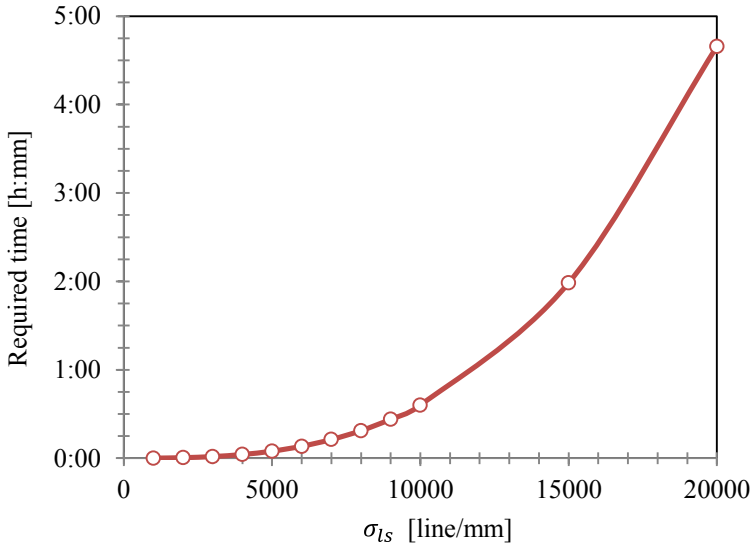

Figure 4.12 Number of line segments per mm vs. running time.

4.6.2.1 Line segment density

In this test the time step factor was 1 ($dt_f = 1$) and the line segment density was varied from 100 $line/mm$ to 10000 $line/mm$. The increment of the line segment density in this test was 100 $line/mm$. All grinding parameters and simulation parameters for this test are listed in Table 4.3. Figure 4.13 shows the line segment density versus contact length. The contact length quickly converges as the line segment density increases; therefore, the line segment density can be as small as 800 $line/mm$.

Table 4.3 The grinding and simulation parameters used in the line segment density test.

Parameter	Simple	Value	Unit
Depth of cut	a	0.1	mm
Cutting speed	v_s	30	m/s
Workpiece speed	v_w	0.3	m/s
Wheel diameter	d_s	200	mm
Grain diameter	d_g	0.253	mm
Grain spacing	L	0.415	mm
Time step factor	dt_f	1	--
Line segment density	δ_{ls}	[100,200, …,10000]	$line/mm$

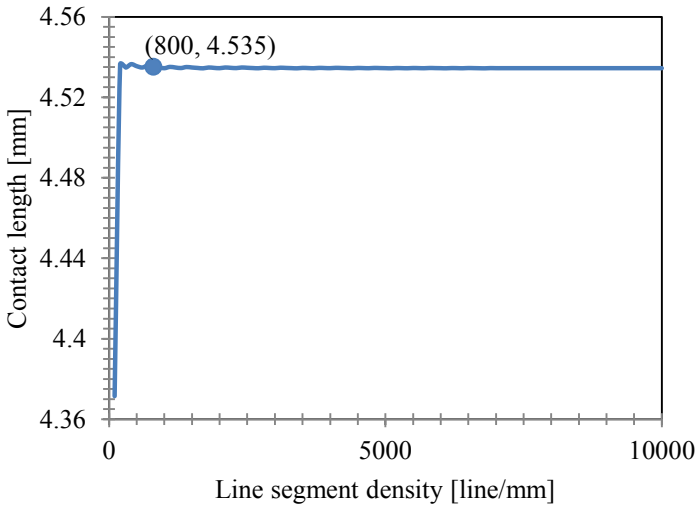

Figure 4.13 Contact length vs. line segment density.

Figure 4.14 plots the uncut chip thickness versus the line segment density. Unlike the contact length, the uncut chip thickness tends to converge slower as the line segment density increases. Moreover, the convergence in the uncut chip thickness is not smooth; the curve has a zigzag shape. This shape occurs because in some cases the uncut chip vertex exists between two adjacent line segments (point l'' in Figure 4.15). Thus, the uncut chip thickness that is determined by Equation (4.17) or Equation (4.18) is less accurate in this case. Therefore, the uncut chip thickness equation was modified by Equation (4.28).

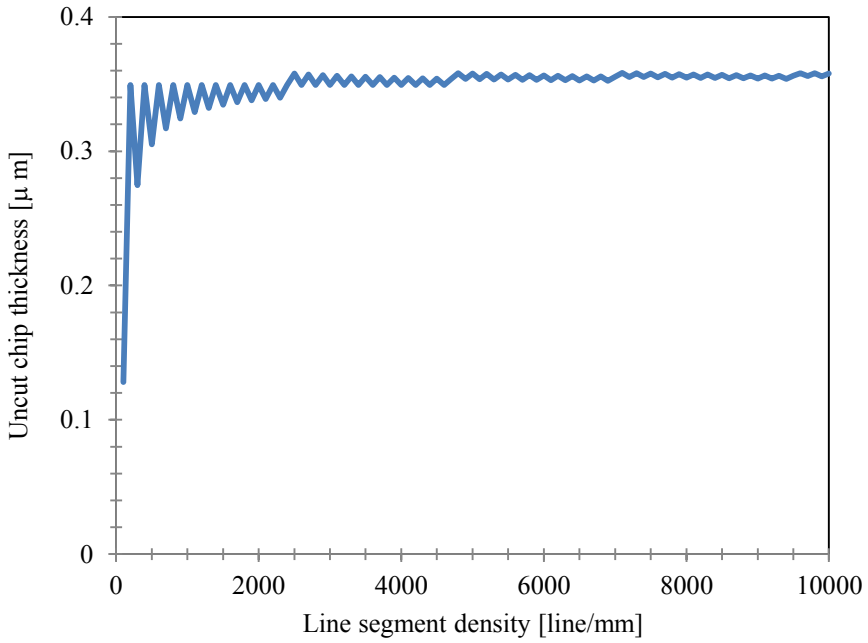

Figure 4.14 Uncut chip thickness vs. line segment density.

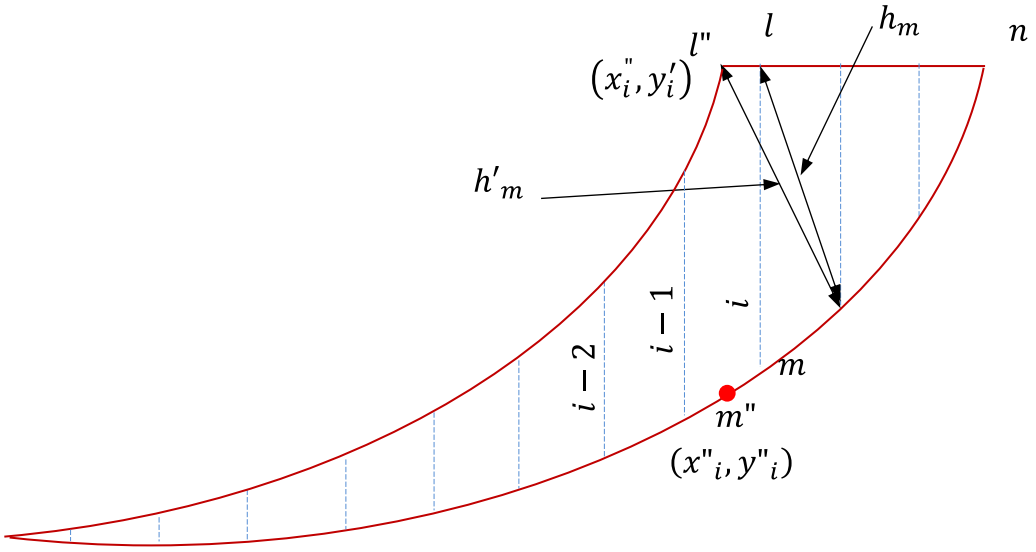

Figure 4.15 The case when the uncut chip vertex does not exist on any line segment.

$$h'_m = \min_{i=m''\to n} \left(\sqrt{(x_{l''} - x_i)^2 + (y_{l''} - y_i)^2}\right) \tag{4.28}$$

Equation (4.28) calculates the shortest distance between point l'' and points from point m'' to point n in Figure 4.15.

For the vertical uncut chip thickness h'_{mv} the following equation was used:

$$h'_{mv} = y'_i - y''_i \tag{4.29}$$

while the following two equations were used to define the point l'' and point m'' components:

$$x''_i = x_{i-2} + \frac{(x_{i-1} - x_{i-2})(y'_i - y_{i-2})}{(y_{i-1} - y_{i-2})} \tag{4.30}$$

$$y''_i = y_{i-2} + \frac{(y_{i-1} - y_{i-2})(x''_i - x_{i-2})}{(x_{i-1} - x_{i-2})} \tag{4.31}$$

In Figure 4.16 it can be seen that the uncut chip thickness calculated by Equation (4.28) converged quickly. It can be also seen in Figure 4.16 that, at high line segment density, the uncut chip thickness calculated by Equation (4.17) and Equation (4.28) are very close. Based on these results an optimum value of line segment density of $1000\ line/mm$ ($1\ \mu m$ between each two line segments) was selected for future simulations.

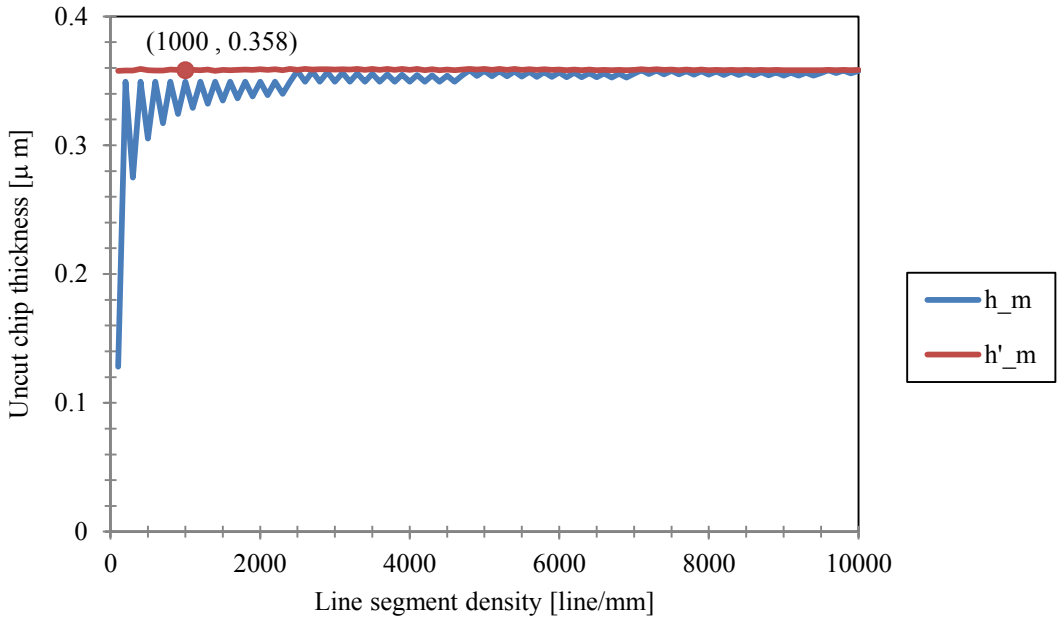

Figure 4.16 The uncut chip thickness before and after the correction by equation (4.28) vs. the line segment density.

4.6.2.2 Time step factor

In this test the simulation was run for the constant value model with a different time step factor dt_f (from 0.1 to 10), while the line segment was set to $1000\ line/mm$. The grinding parameters that are listed in Table 4.4 were used in the simulation.

Figure 4.17 plots the contact length at different values of the time step factor. The contact length is relatively stable in relation to the time step factor within the range of $[0.1 - 10]$. The difference between the maximum and minimum contact length in this test is 0.11%.

In Figure 4.18 it is clear that the uncut chip thickness is more sensitive to the change in the time step factor. In this test, the difference between the maximum and minimum uncut chip thickness exceeds 35.55%; therefore, the optimum value for the time step factor was set to 1.

Table 4.4 The grinding and simulation parameters used in the time step factor test.

Parameter	Simple	Value	Unit
Depth of cut	a	0.1	mm
Cutting speed	v_s	30	m/s
Workpiece speed	v_w	0.3	m/s
Wheel diameter	d_s	200	mm
Grain diameter	d_g	0.253	mm
Grain spacing	L	0.415	mm
Time step factor	dt_f	$[0.1 , 0.2 , \dots , 10]$	--
Line segment density	δ_{ls}	1000	$line/mm$

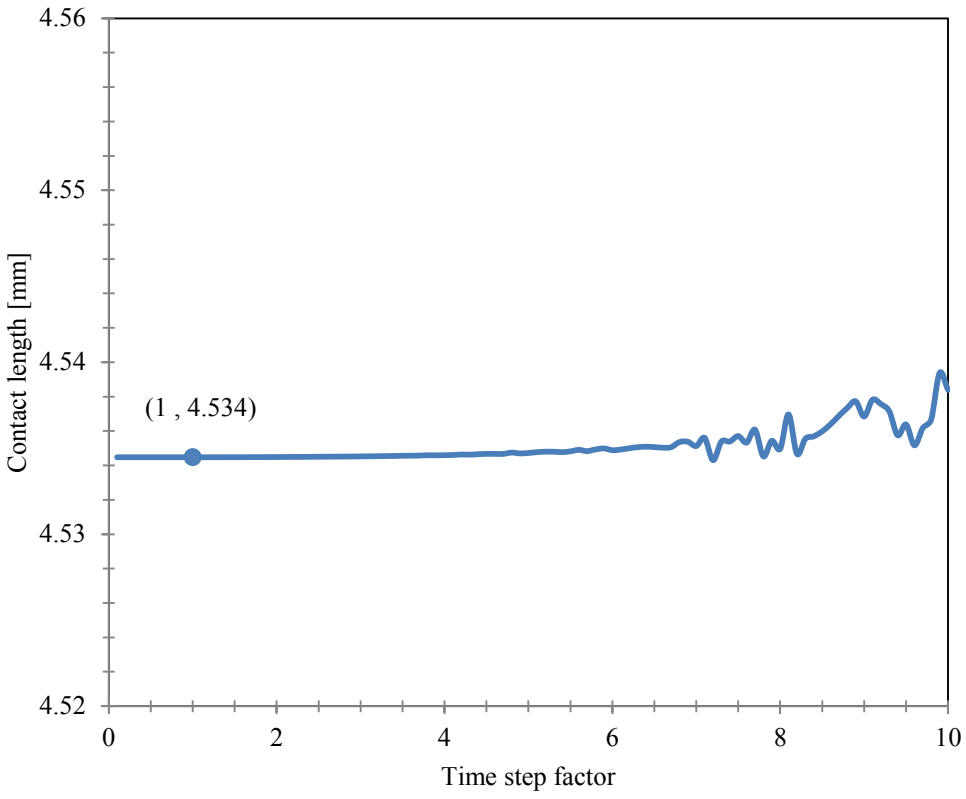

Figure 4.17 The contact length vs. time step factor.

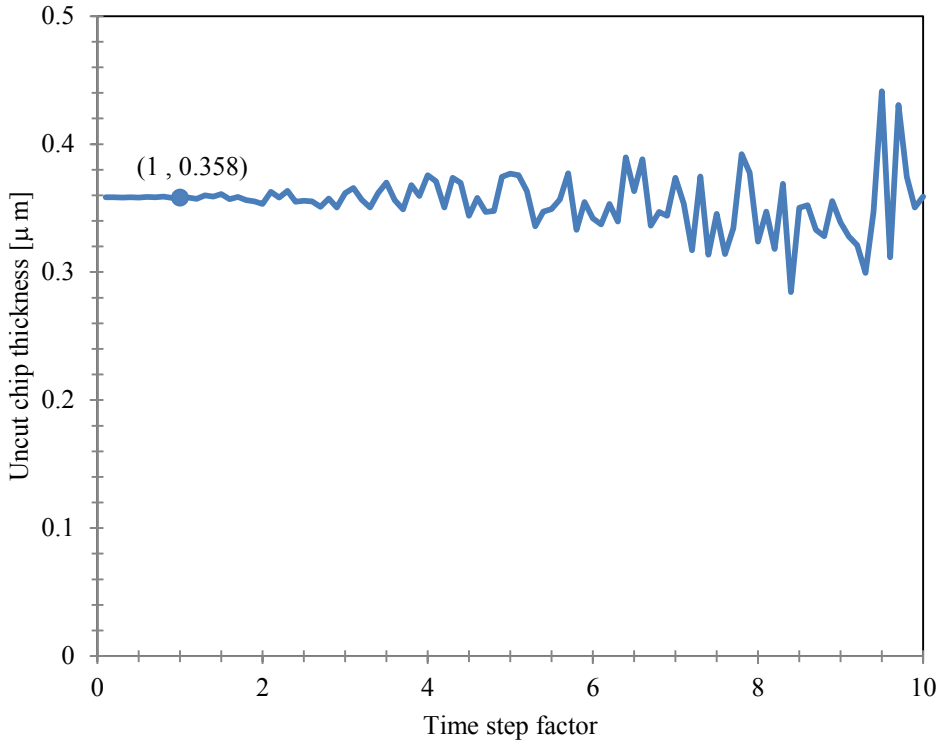

Figure 4.18 The uncut chip thickness vs. time step.

4.6.3 Uncut chip thickness calculation test

In the simulation of grinding operations the instantaneous uncut chip thickness and contact length are calculated for each time step and for each active grain. This calculation requirement means that Equation (4.28) and Equation (4.19) are executed many times. From a computing perspective, Equation (4.28) takes much more time than Equation (4.29) does, because Equation (4.28) is significantly more complex. Thus, replacing Equation (4.28) with Equation (4.29) to calculate the instantaneous uncut chip thickness can significantly reduce time required for the simulation but might result in an inaccurate calculation. Thus, the uncut chip thickness was calculated first by Equation (4.28) and then by Equation (4.29) for the constant value grinding wheel model. The grinding

parameters that are listed in Table 4.3 were used for this test except for the line segment density, ranged from 5000 to 100,000 $line/mm$.

Figure 4.19 plots the differences between the uncut chip thicknesses calculated by Equation (4.28) and Equation (4.29) versus the lines segment density. The differences were calculated using Equation (4.32). It can be clearly seen that, in surface grinding, the difference between the uncut chip thickness that is calculated by Equation (4.28) and Equation (4.29) does not exceed 0.1% even when using very high density of line segment 100,000 $line/mm$. From these results, it can be concluded that the uncut chip thickness can be calculated using Equation (4.29).

$$\text{Difference} = \frac{\sqrt{\left(h'_m - h'_{m_v}\right)^2}}{h'_m} \times 100\ \% \tag{4.32}$$

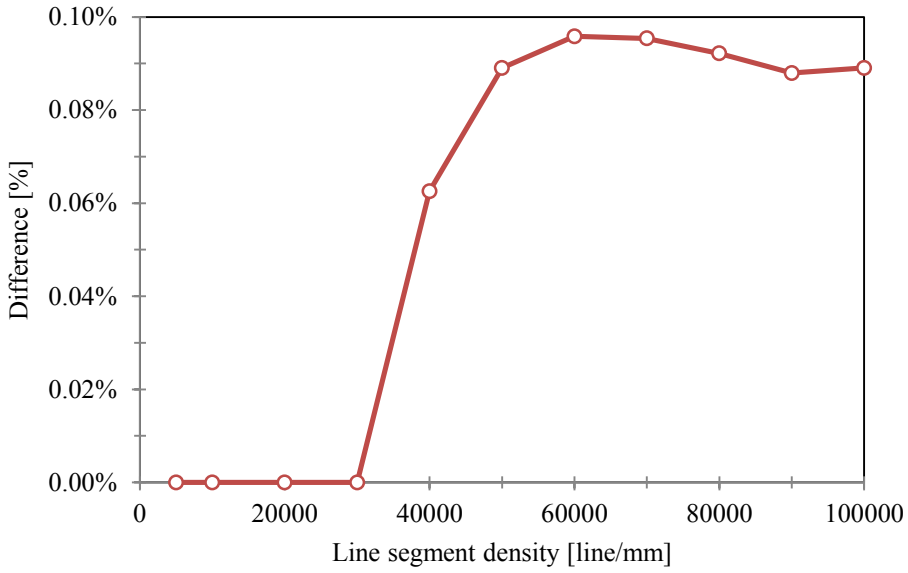

Figure 4.19 The difference between the uncut chip thickness by Equation (4.28) and Equation (4.29).

4.7 Result and discussion

4.7.1 Result for the constant value model

Figure 4.20 graphs the results of the simulation as the cutting edges pass through the cutting zone for the constant value model. Note that the image has been stretched significantly in the vertical direction as can be noted by the elliptic rather than circular grains. This stretching operation was conducted in order to emphasize the submicron uncut chip thickness typical of grinding. As can be seen from this figure every grain is cutting material from the workpiece.

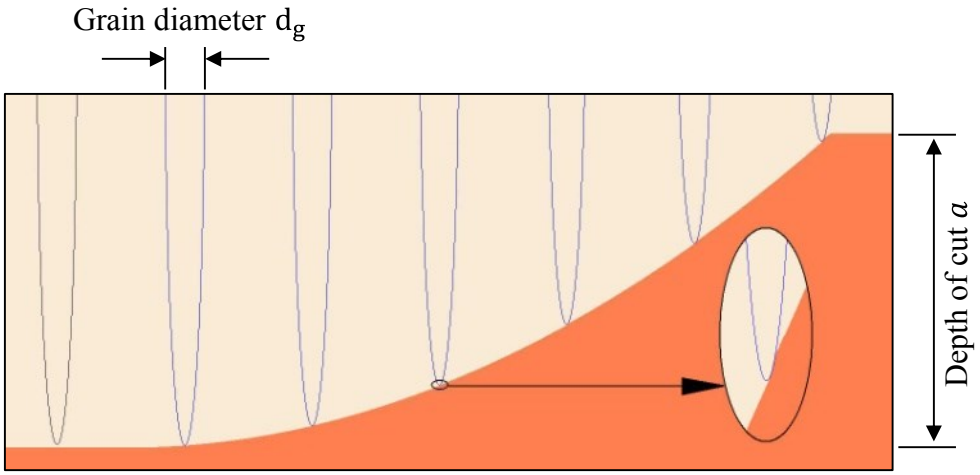

Figure 4.20 Graphical output of the simulation using the constant value model.

The parameters summarized in Table 4.5 (Case 1) were used to compare the simulation results of the constant value model with the analytical model results. Figure 4.21 and Figure 4.22 plot the uncut chip thickness and contact length as a function of depth of cut for both the "Simulated" results (using the constant value model) and the "Analytical" results obtained from Equation (2.6) and Equation (2.9). These two figures show excellent agreement between the simulation and analytical results. The differences in the uncut chip thickness and contact length were 1.1% and 1.4% for a depth of cut $0.1\ mm$, and 1.0% and 2.1% for a depth of cut of $0.01\ mm$.

Table 4.5 Grinding parameters.

Parameter	Symbol	Case1	Case2	Unit
Depth of cut	a	0.01 – 0.1	0.01 – 0.1	mm
Wheel Diameter	d_s	200	200	mm
Wheel Speed	v_s	30	30	m/s
WP Speed (feed)	v_w	0.3	0.3	m/s
Grain Spacing	L_{min}	0.415	Stochastic	mm
Grain Diameter	d_{g_min}	0.253	Stochastic	mm
Grain Protrusion Height	H_{g_min}	0.127	Stochastic	mm

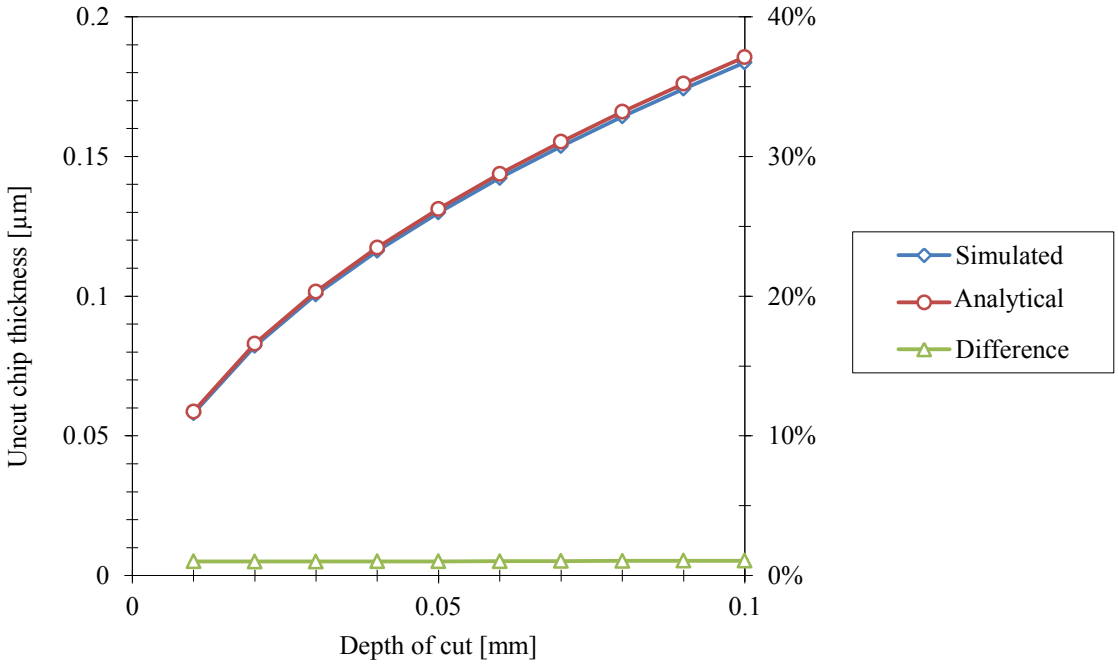

Figure 4.21 The Simulated and Analytical uncut chip thickness vs. the depth of cut (constant value model).

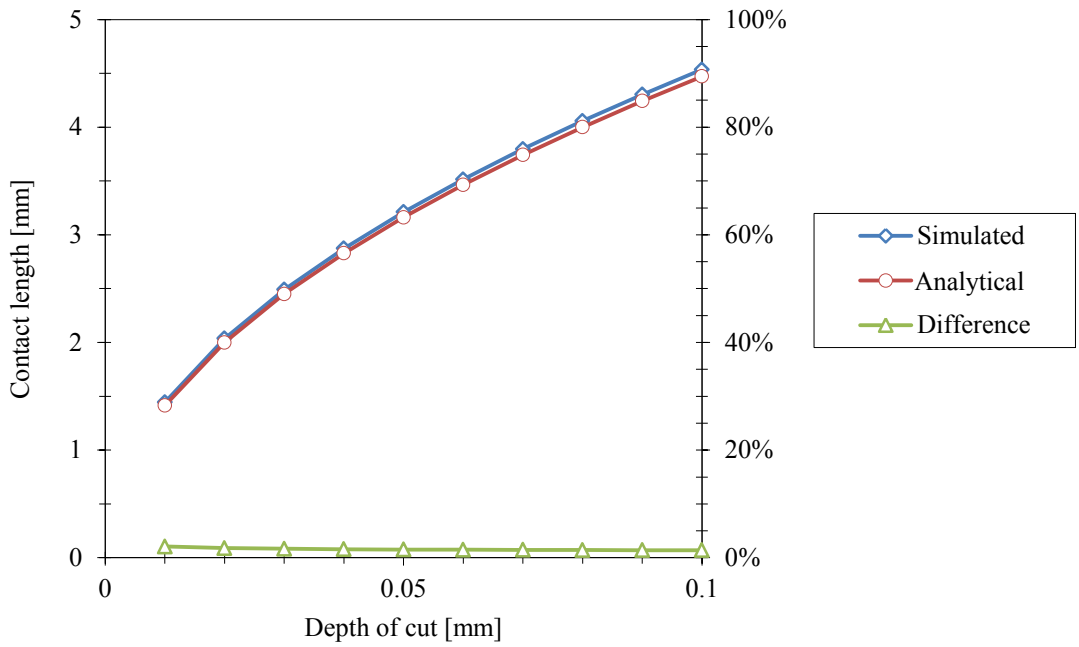

Figure 4.22 The simulated and Analytical contact length vs. the depth of cut (constant value model).

4.7.2 Result for the stochastic models

Figure 4.23 graphs the results of the simulation as the cutting edges pass through the contact zone for a stochastic model. Note that the image has been stretched significantly in the vertical direction as can be noted by the elliptic rather than circular grains. This stretching operation was conducted in order to emphasize the uncut chip thickness. As can be seen from this figure only three of six grains are cutting material from the workpiece.

The parameters in Table 4.5 (Case 2) were then used to compare the simulation results using the stochastic wheel model with the analytical results. Four different versions of the stochastic model were implemented in order to identify the individual effects of stochastic grain size, grain spacing, and grain protrusion height on both the uncut chip thickness and contact length. These four models are referred to as the stochastic grain size model ("Stochastic dg"), stochastic spacing model ("Stochastic L"), stochastic

protrusion height model ("Stochastic Hg") and the full stochastic model ("All stochastic"). Figure 4.24 and Figure 4.25 plot the resulting average uncut chip thickness and the average contact length as a function of the depth of cut using the simulated results from all four stochastic models as well as the analytical results using Equation (2.6) and Equation (2.9). Note that the difference curves "Diff_hm" in Figure 4.24 and "Diff_lc" in Figure 4.25 refer to the difference between the analytical results and the simulated results with the "All Stochastic" model. Several observations can be made from these figures.

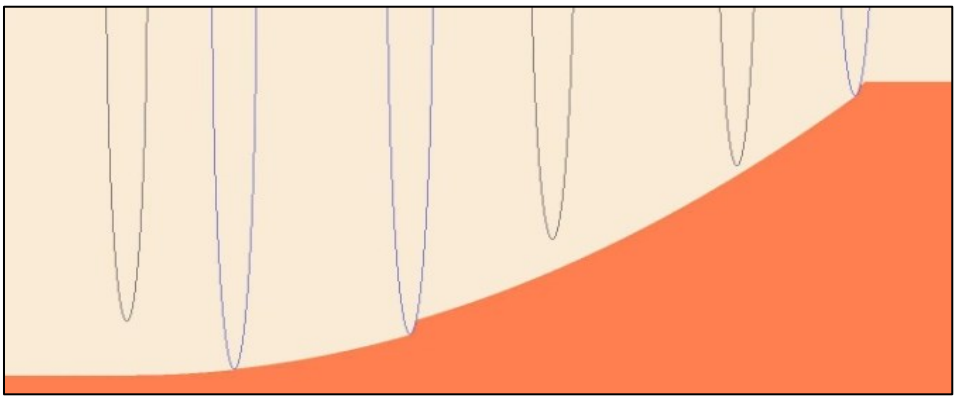

Figure 4.23 The graphical result of the cutting zone for the stochastic model.

The "Analytical", "Stochastic L" and "Stochastic dg" models behaved in roughly the same manner. As the depth of cut increased the average contact length and the average uncut chip thickness increased. It can also be seen in Figure 4.24 that the average uncut chip thicknesses for the "Analytical", "Stochastic Hg" and "All Stochastic" models behave in roughly the same manner. However, as can be seen in Figure 4.25, the average contact length calculated by the "Stochastic Hg" and "All Stochastic" models is an order of magnitude smaller than the average contact length calculated by the "Analytical" model.

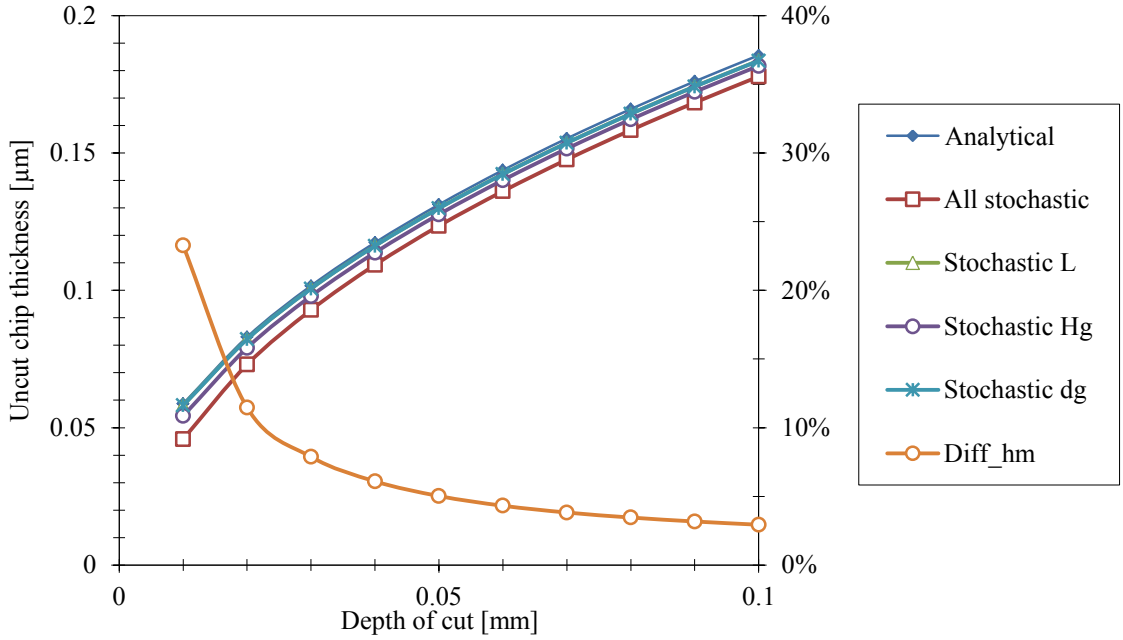

Figure 4.24 The Simulated and Analytical uncut chip thickness (stochastic model).

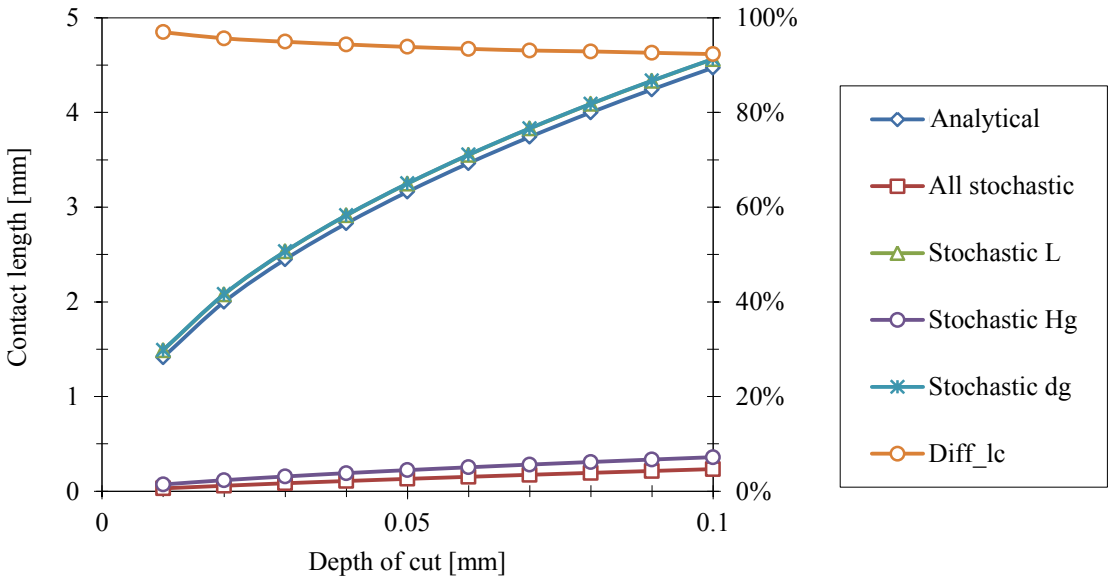

Figure 4.25 The Simulated and Analytical contact length (stochastic model).

The reason that the contact length results and uncut chip thickness results behave in substantially different manners can be explained using Figure 4.26. If grain 1 and grain 2 are active then the average uncut chip thickness and contact length are:

$$\bar{h}_m = \frac{h_{m1} + h_{m2}}{2} \tag{4.33}$$

$$\bar{l}_c = \frac{l_{c1} + l_{c2}}{2} \tag{4.34}$$

If grain 1 is inactive because it does not protrude far enough, then the uncut chip thickness and the contact length become:

$$\bar{h}_m = \frac{h_{m1} + h'_{m1}}{2} \tag{4.35}$$

$$\bar{l}_c = \frac{l_{c1}}{2} \tag{4.36}$$

Since h'_{m1} and h_{m2} are approximately the same and l_{c1} and l_{c2} are approximately the same, it can be deduced from these equations that the average uncut chip thickness for one verses two active grains are nearly the same but the average contact length for one active grain is about half the average contact length for two active grains.

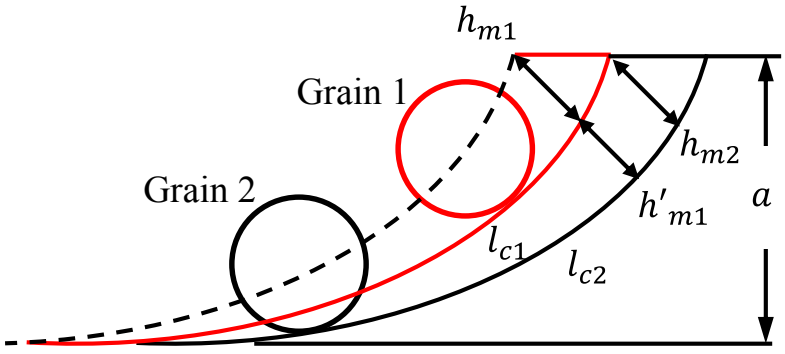

Figure 4.26 Illustration of two successive grains when both are active and when just one is active.

This point is further illustrated by Figure 4.27, which shows the uncut chip thickness and the contact length values of seven successive grains from all four stochastic models. For the "Stochastic L" and the "Stochastic dg" models all seven grains are active, while only grain number 1 and 7 are active for the "All stochastic" and the "Stochastic Hg" models. For the "Stochastic L" and the "Stochastic dg" models the uncut chip thickness and the contact length for each grain are approximately equal to the analytical results. However, in the "All stochastic" and the "Stochastic Hg" models, the contact length of the active grains (1 and 7) are approximately equal to the analytical contact length obtained from Equation (2.6), while the uncut chip thickness of the active grains are much greater than the analytical uncut chip thickness. The inactive grains (from 2 to 6) have zero values of the uncut chip thickness and contact length. The result is that the average of simulated uncut chip thickness is approximately equal to the analytical uncut chip thickness obtained from Equation (2.9), while the average of simulated contact length is much smaller than the analytical contact length obtained from Equation (2.6).

Figure 4.28 shows the uncut chip thickness for every single active grain on the circumference of the wheel for a depth of cut of $0.1\ mm$ for the full stochastic model. Note that the inactive grains have been eliminated from Figure 4.28 since they have zero values for the uncut chip thickness. For this depth of cut, the analytical and simulation models estimated that the average of the uncut chip thickness was $0.19\ \mu m$ and $0.18\ \mu m$ respectively, which is only a 2.9% difference. However, even though the difference in the average value is small, the range of uncut chip thicknesses produced by the stochastic full model is huge – the minimum value was $0.00\ \mu m$, the maximum value was $8.45\ \mu m$ and the standard deviation was $0.8\ \mu m$. Furthermore, only 8.5% of the grains are actually cutting! The reason that so few grains are involved in cutting is because, in many cases, grains do not protrude far enough out of the wheel or follow too closely behind an active grain.

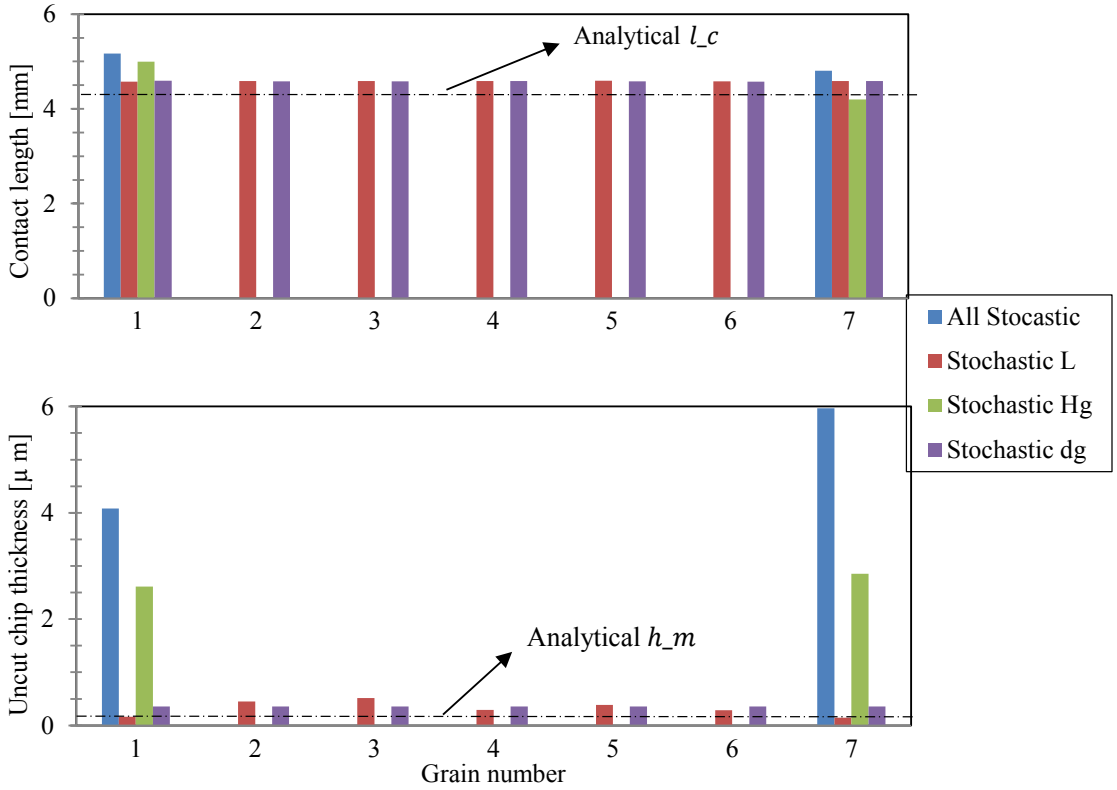

Figure 4.27 The uncut chip thickness and contact length values of seven successive grains for the four stochastic models.

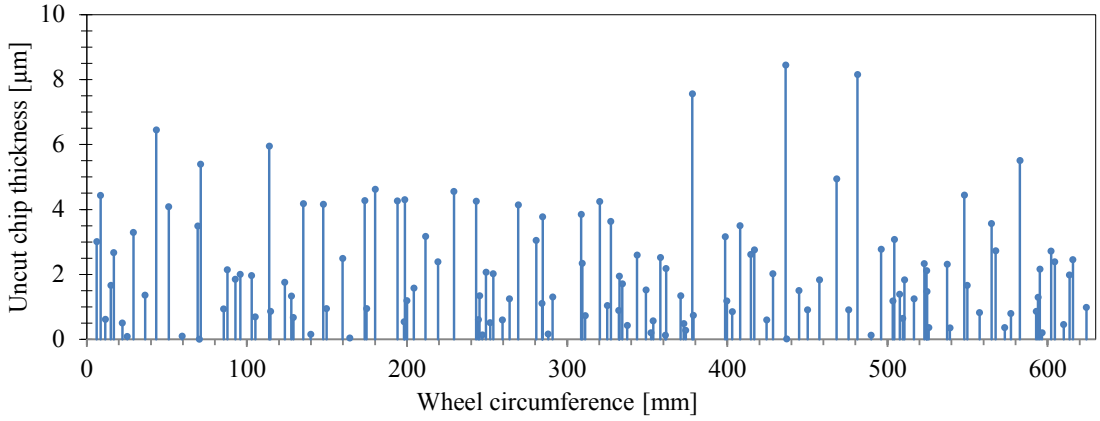

Figure 4.28 The simulated uncut chip thickness for every active grain at the depth of cut of 0.1 mm vs. wheel circumference.

Table 4.6 shows the average, the minimum, the maximum, and the standard deviation of the uncut chip thicknesses and the contact lengths at a depth of cut of $0.1\,mm$ for all stochastic models. It is clear that the "Stochastic Hg" model has much more effect on the result than the "Stochastic dg" model and "Stochastic L" model. In the "Stochastic Hg" model only 10.9% of the grains were contributing to the cutting operation while 100% of the grains were active in the "Stochastic dg" model and the "Stochastic L" model. Moreover, the standard deviation of the uncut chip thickness and contact length for the "Stochastic Hg" model was $0.7\mu m$ and $1.11\,mm$, respectively, while the standard deviation of the uncut chip thickness and contact length for the "Stochastic dg" model was $0.00\,\mu m$ and $0.01\,mm$, respectively, and the standard deviation of the uncut chip thickness and contact length for the "Stochastic L" model was $0.05\,\mu m$ and $0.27\,mm$, respectively.

Table 4.6 Summary of results for all four stochastic models at the depth of cut of 0.1 *mm*.

		Full stochastic	L stochastic	Hg stochastic	dg stochastic
Uncut chip thickness [µm]	Average	0.18	0.18	0.18	0.18
	Minimum	0.00	0.04	0.00	0.18
	Maximum	8.45	0.42	5.94	0.18
	Standard Deviation	0.8	0.05	0.7	0.0
Contact length [mm]	Average	0.34	4.55	0.46	4.58
	Minimum	0.00	0.01	0.00	4.54
	Maximum	5.30	4.60	4.95	4.59
	Standard Deviation	0.87	0.27	1.11	0.01
Active grain		8.5%	100%	10.9%	100%

4.8 Summary

This chapter presented a 2D metal removal simulation for grinding based on the z-map technique, due to its straightforwardness and the ability to upgrade to 3D. The model was used to estimate the uncut chip thickness and contact length when the grain spacing, grain size and protrusion height were assume to follow stochastic distributions. The model was also used to investigate the effect of the distribution of grain size, grain inter-spacing and grain protrusion height on the calculation of the uncut chip thickness and contact length.

CHAPTER 5. 3D METAL REMOVAL SIMULATION FOR GRINDING

5.1 Introduction

In this chapter the 2D metal removal model for grinding will be upgraded to a 3D model. A 3D wheel model will be generated based on the information obtained from the wheel marking system in order to be used for the 3D metal removal model. Spherical grains were evenly sized and distributed within the wheel volume, and the grains were then randomly resized and replaced. The interaction between the grains and the workpiece material was simulated and the uncut chip thickness and contact length was calculated for each active grain. In addition, the machined surface of the workpiece was generated and the surface topography was compared with experimental results.

5.2 Method

Similar to the 2D metal removal simulator, the proposed 3D version is based on the work of Kim [60], which was used to simulate metal removal in surface milling. In the following sections the grain, workpiece and their interaction will be introduced, followed by the determination of the uncut chip geometry in 3D.

5.2.1 The workpiece

In the proposed simulator the workpiece is represented by a set of evenly spaced vertical line segments distributed in the $x-z$ plane and the abrasive grain is represented by a sphere as shown in Figure 5.1. The position of each line segment in the array is identified by its i and j index. The length of each line segment, in the y-direction, represents the workpiece height. The number of line segments in the x and z directions times the space between the line segments represent the workpiece length and width, respectively. The accuracy of the workpiece representation is determined by the spacing of the line segments. Smaller spacing will result in a more accurate but computationally slower model. Conversely larger spacing will result in a less accurate but computationally fast model. Each line segment is represented by a one-dimensional parametric equation, which uses a length parameter called f.

$$x_{ij} = x_{ij}^1 - f\left(x_{ij}^1 - x_{ij}^0\right) \tag{5.1}$$

$$y_{ij} = y_{ij}^1 - f\left(y_{ij}^1 - y_{ij}^0\right) \tag{5.2}$$

$$z_{ij} = z_{ij}^1 - f\left(z_{ij}^1 - z_{ij}^0\right) \tag{5.3}$$

$$[0 \leq f \leq 1]$$

Note that for the special case where the line segment is parallel with the y-axis, $x_{ij} = x_{ij}^0 = x_{ij}^1$ and $z_{ij} = z_{ij}^0 = z_{ij}^1$.

5.2.2 The grains

For simplification, in this work the grains are assumed to have a spherical shape. Note, however, that with this technique any grain shape can be modeled. The sphere center $(x_c\,, y_c\,, z_c)$ travels along a trochoidal path, which is a combination of a rotation and a translation as expressed in Equations (5.4), (5.5) and (5.6):

$$x_c(t) = v_w t + \frac{d_s}{2} cos\left(\frac{t\, v_s}{\frac{d_s}{2}} + \beta\right) + x_w \tag{5.4}$$

$$y_c(t) = \frac{d_s}{2} sin\left(\frac{t\, v_s}{\frac{d_s}{2}} + \beta\right) + y_w \tag{5.5}$$

$$z_c(t) = Constant \tag{5.6}$$

where t is the time, $(x_w\,, y_w\,, z_w)$ is the grinding wheel center coordinates and β is the grain angular component in the polar coordinate system in the $x-y$ plane (grain angle) and is calculated by the following equation:

$$\beta = \tan^{-1}\left(\frac{y_c - y_w}{x_c - x_w}\right) \tag{5.7}$$

The grain radial component in the polar coordinate system in the $x-y$ plane is calculated by the following equation:

$$R_g = \sqrt{(x_c - x_w)^2 + (y_c - y_w)^2} \tag{5.8}$$

5.2.3 The grain/wheel interaction

Intersecting the sphere with the line segments at discrete time intervals simulates the metal removal. The portions of the line segments that are inside the circle (dashed lines in Figure 5.1) are removed by adjusting the length of the line segments. Equation (5.9) describes the sphere, which intersects the line segments.

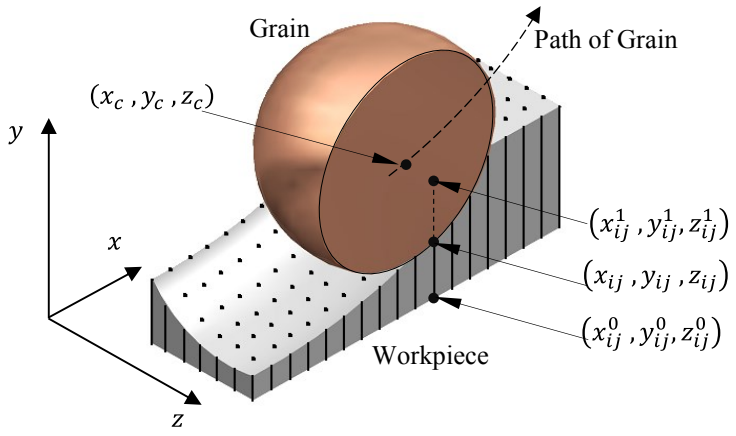

Figure 5.1 Metal removal simulation for a single grain.

$$(x - x_c)^2 + (y - y_c)^2 + (z - z_c)^2 = {R_g}^2 \tag{5.9}$$

To define the intersection point between the sphere and each line segment, Equations (5.1), (5.2) and (5.3) are substituted into Equation (5.9) to obtain Equation (5.10):

$${y_{ij}}^2 + 2y_c \; y_{ij} + k = 0 \tag{5.10}$$

where $k = {y_c}^2 + \left(x_{ij} - x_c\right)^2 + \left(z_{ij} - z_c\right)^2 - {R_g}^2$

Using the quadratic equation, y_{ij} can be determined. The length parameter f is then found by rearranging Equation (5.3) in the following manner:

$$f = \frac{y_{ij}^1 - y_{ij}}{y_{ij}^1 - y_{ij}^0} \tag{5.11}$$

Note that the length parameter f can be one of the following three cases:

1. $f = comlex\ number$, No intersection point between the line segment and the sphere exists.

2. $f < 0$ or $f > 1$, The intersection point is outside the range of interest.
3. $0 \leq f \leq 1$, The intersection point is inside the range of interest.

Once the length parameter f is obtained with a value of $0 \leq f \leq 1$, the cut portion is removed by substitution of ${y_{ij}}^1$ with the y_{ij} value that is obtained from Equation (5.10).

5.2.4 Uncut chip thickness and contact length calculations

The uncut chip thickness and contact length can be determined by examining the simulated chip as shown in Figure 5.2. The chip consists of a rectangular grid of vertical line segments. The chip is then sectioned into a series of planes that are parallel to the $x - y$ plane. Each of these cross-sectional planes is numbered from j_{min} to j_{max} using its j index. One of these planes is highlighted in Figure 5.2. Each line segment in this plane is numbered from i_{min} to i_{max} using its i index. The maximum uncut chip thickness h_{m_j} can be defined for each cross-section plane as the shortest distance between the point $({x'}_{mj}, {y'}_{mj}, {z'}_{mj})$ in Figure 5.2 and the bottom vertices of the line segments representing the chip as described by the following equation:

$$h_{m_j} = \min_{i=i_{min} \to i_{max}} \left(\sqrt{\left(x_{mj} - x_{ij}\right)^2 + \left(y_{mj} - y_{ij}\right)^2 + \left(z_{mj} - z_{ij}\right)^2} \right) \tag{5.12}$$

The maximum uncut chip thickness can then be found by determining the maximum values of the chip thickness for all the slices making up a chip. However, since the chip cross section is very irregular, this measure of chip thickness was deemed to be a poor measure of the actual chip thickness. An average maximum chip thickness was used instead, by finding the average of the maximum uncut chip thicknesses for all cross-section planes as shown in the following equation:

$$h_m = \frac{1}{j_{max} - j_{min}} \sum_{j=j_{min}}^{j_{max}} h_{m_j} \tag{5.13}$$

The contact length for each cross-section is the summation of the distances between the bottom vertices of successive cut line segments as shown in Equation (4.14).

$$l_{c_j} = \sum_{i=i_{min}}^{i_{max}} \sqrt{\left(x_{(i-1)j} - x_{ij}\right)^2 + \left(y_{(i-1)j} - y_{ij}\right)^2 + \left(z_{(i-1)j} - z_{ij}\right)^2} \quad (5.14)$$

Therefore, the average contact length for the chip is:

$$l_c = \frac{1}{j_{max} - j_{min}} \sum_{j=j_{min}}^{j_{max}} l_{c_j} \quad (5.15)$$

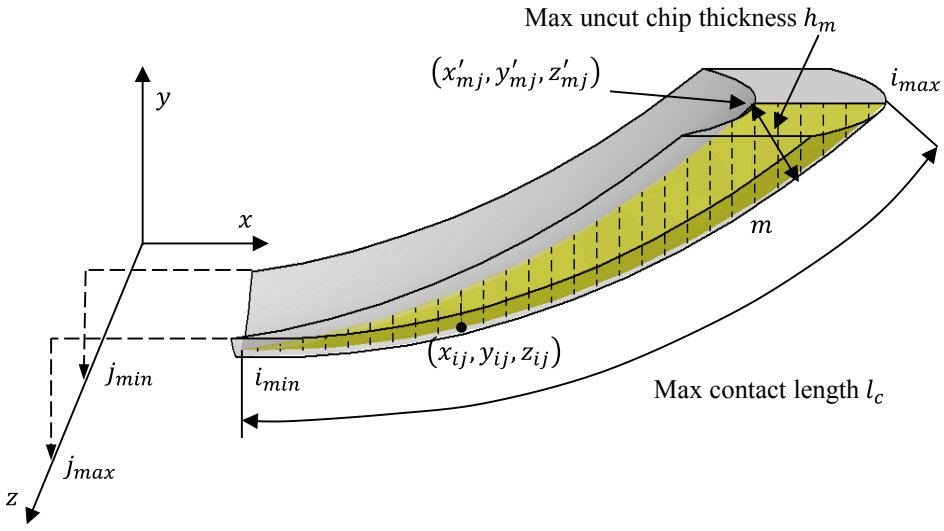

Figure 5.2 The uncut chip thickness and contact length on the 3D chip.

5.2.5 Grinding wheel model

The proposed simulator was used in conjunction with a non-stochastic and a stochastic grinding wheel model.

5.2.5.1 Non-stochastic wheel model

The non-stochastic model consisted of a single row of uniformly sized grains evenly spaced about the circumference of the grinding wheel as shown in Figure 5.3. In the

stochastic model the grain size, protrusion height and spacing were randomly distributed. According to Malkin [2], Equation (5.16) and (5.17) can be used to calculate the average grain diameter d_g and the grain volume fraction V_g. For this work, the nominal grain diameter, protrusion height and spacing were determined based on a wheel with a grit number M of 60 and a structure number S of 8.

$$d_g = 15.2\, M^{-1} \tag{5.16}$$

$$V_g = 0.02(32 - S) \tag{5.17}$$

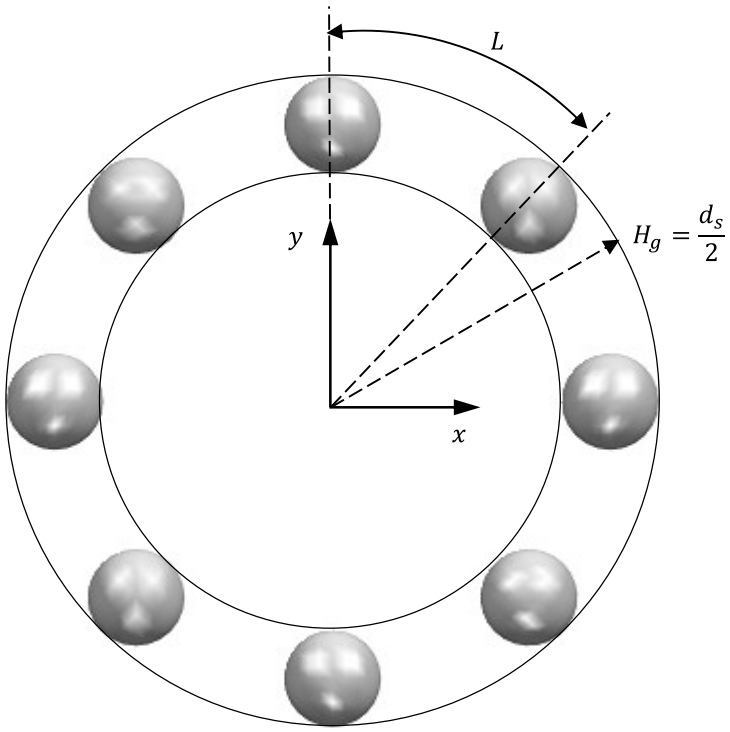

Figure 5.3 Illustration of the single row constant value model.

For the non-stochastic model, the grinding wheel takes the shape of a torus; therefore, the packing density in this model is the number of grains n times the grain volume V_{grain} divided by the volume of the torus V_t:

$$V_g = \frac{n\,V_{grain}}{V_t} = \frac{n\,\frac{\pi}{6}d_g^3}{\frac{\pi^2}{4}(d_s - d_g)d_g^2} \tag{5.18}$$

Therefore, the number of grains in the non-stochastic model can be calculated by rewriting Equation (5.18) as follows:

$$n = \frac{3}{2}\,\pi\,V_g\left(\frac{d_s}{d_g} - 1\right) \tag{5.19}$$

The grain spacing *L*, which is the distance between the centers of two successive grains, can be calculated using Equation (5.20).

$$L = \frac{\pi(d_s - d_g)}{n} \tag{5.20}$$

5.2.5.2 Stochastic wheel model

The stochastic model considered the distribution of grain size, spacing and protrusion height. This model is a modified version of that proposed by Koshy *et al.* [13]. The stochastic wheel model was generated for a Radiac Abrasives (WR-A-60-J5-V1) aluminum oxide grinding wheel. Using the equations from Equation (5.16) to Equation (5.19) the grain diameter was $0.253\,mm$, the packing density 0.48, the wheel diameter $355\,mm$, and the wheel width $5.06\,mm$. The number of grains in this model was 552,425 grains.

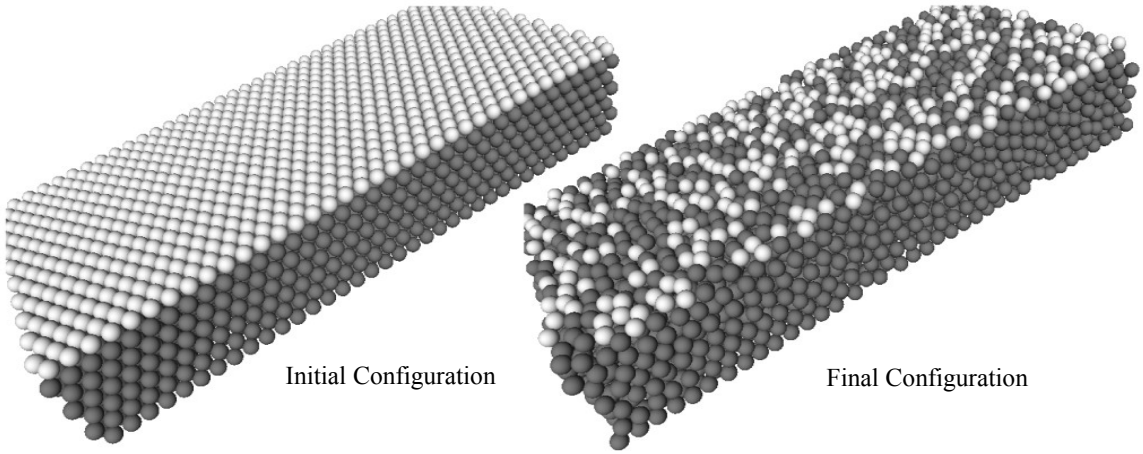

Figure 5.4 The stochastic grinding wheel model before and after shaking process.

To generate the stochastic grinding wheel model, grains with the average diameter were distributed evenly within the wheel volume to achieve a grain packing density as shown in the initial wheel segment in Figure 5.4. Subsequently, each grain was randomly moved in the x, y and z directions. If a grain interfered with another grain or was outside the wheel's boundary, it was moved back until it touched the other grain or the wheel border. This shaking process continued until the grain distribution was as homogenous as possible. A portion of the final wheel is shown in Figure 5.4. Since the wheel surface is irregular, a decision had to be made as to whether a grain was on the surface of the wheel or not. It was decided that, if a grain was within 0.1 grain diameter of the maximum protrusion height, then the grain was considered to be on the surface and potentially actively involved in cutting. In Figure 5.4, the grains that meet this requirement are colored white, and are considered to be on the wheel surface.

The distribution of grains was assessed in the following manner. A number of parallel cutting planes were intersected with the wheel model, as illustrated in Figure 5.5. For each plane the 2D packing density was calculated by dividing the area of all sectioned grains by the area of sectioned wheel.

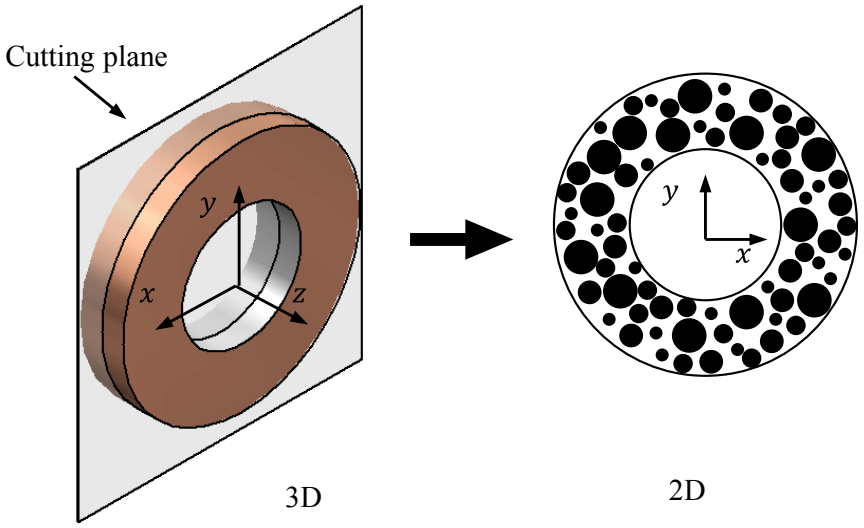

Figure 5.5 2D packing density.

Figure 5.6 shows the resulting 2D packing density versus the distance along the y-axis for the stochastic model before and after the shaking process. Before shaking, the packing density varies periodically along y-axis from 0.0 to approximately 0.72 because of the regular spacing of the grains, but had the anticipated average packing density of 0.48. After shaking, the variation in the packing density is significantly reduced, especially towards the center of the wheel, and the average packing density is still 0.48. Closer to the boundaries there is still considerable variation in the packing density due to the constraint on grain movement cause by the boundary condition. To mitigate the boundary effect, only $2\,mm$ of the central portion of the stochastic wheel was used in the metal removal simulations.

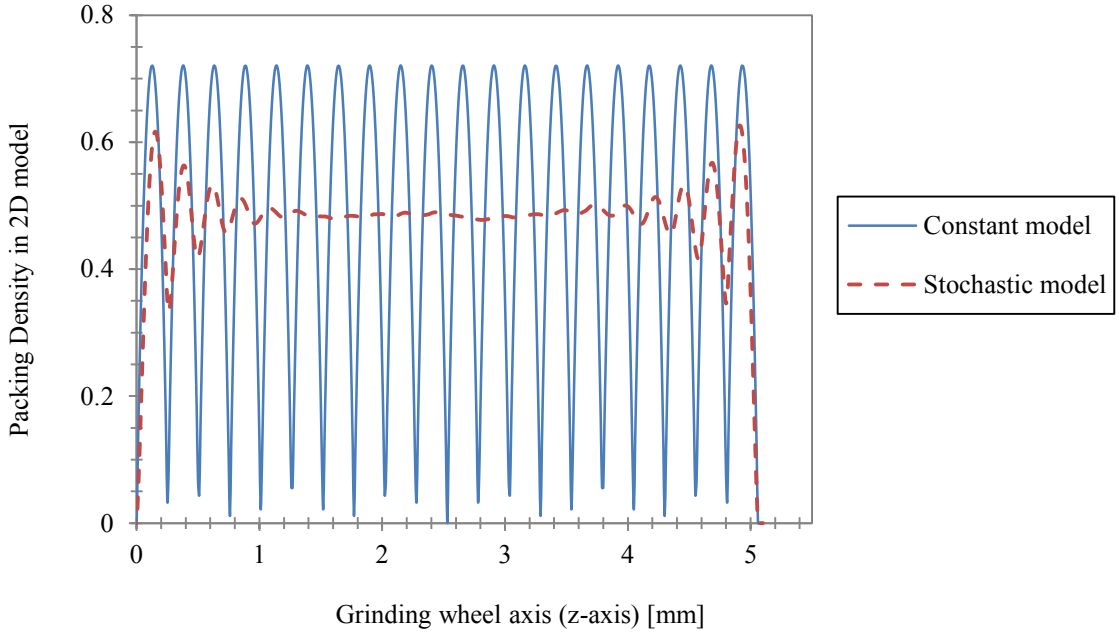

Figure 5.6 Packing density in 2D models along the grinding wheel axis.

After the grains have been shaken, the grain size is adjusted to account for the distribution of grains typically found in grinding wheels. According to Koshy *et al.* [12] and Hou *et al.* [30] the distribution of grain sizes for a given nominal grain size usually has a normal distribution. A standard grit number is defined in terms of grain sizes corresponding to five sieves (Malkin [2]). A 60 grit wheel has grains caught on sieves number 46, 54, 60, 70, and 80. Using Equation (5.16) and grit numbers 46 and 80, the minimum d_{g_min} and maximum d_{g_max} grains size were calculated. The standard deviation of the grain diameter was then defined as follows:

$$\sigma = \frac{d_{g\_max} - d_{g\_min}}{6} \tag{5.21}$$

Figure 5.7 shows that the grain diameters used in this simulation were specified to have a normal distribution. The protrusion height H_g is the distance that a cutting edge protrudes from the grinding wheel center. Researchers are somewhat divided on whether the

protrusion height is a normal distribution or a uniform distribution [13]. In this work the protrusion height for the stochastic model was a result of the shaking process; however, it is found that the protrusion height has an approximately uniform distribution as shown in Figure 5.8. Based on experimental results, Koshy *et al.* [13], concluded that the grain spacing conforms to a gamma distribution. The grain spacing distribution for the 3D wheel model was accomplished by applying a cutting plane parallel to x-y plane (see Figure 5.5) and generating a 2D model for the sectioned grains in this plane. Subsequently, in the 2D model the grain spacing was calculated for the grains that were exposed in the wheel working surface. Several 2D models were generated and the average grain spacing histogram was calculated. It was found that the grain spacing exhibited an approximately gamma distribution as shown in Figure 5.9.

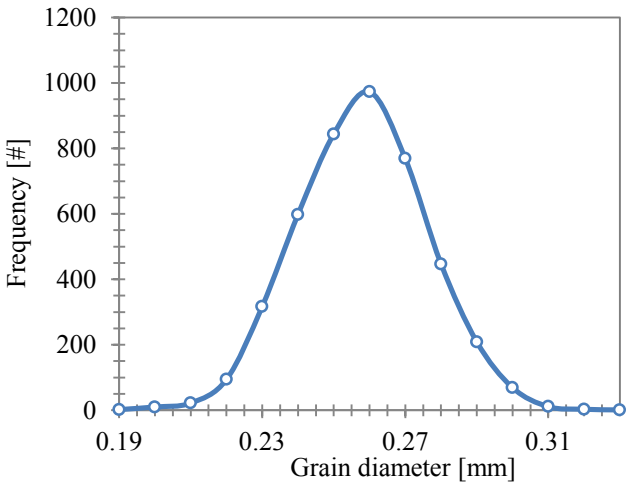

Figure 5.7 Grain size histogram for stochastic grinding wheel model.

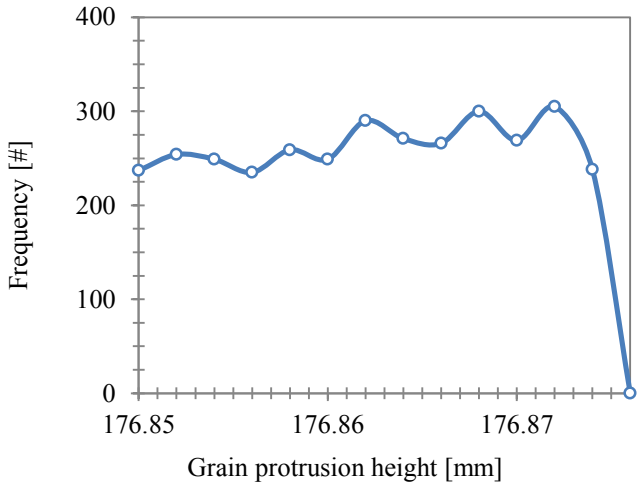

Figure 5.8 Grain protrusion height histogram for stochastic grinding wheel model.

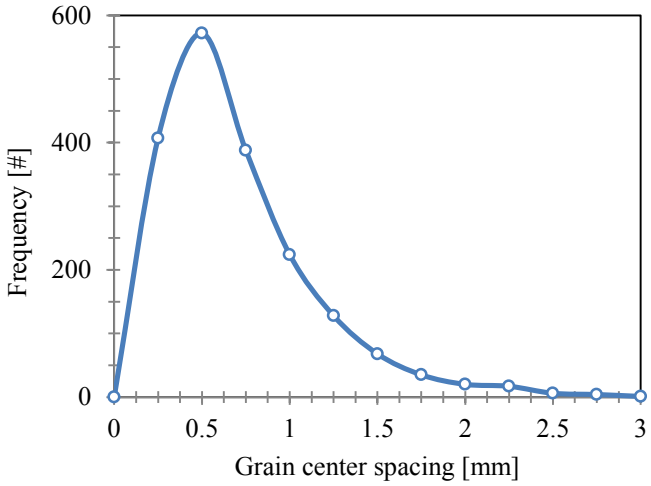

Figure 5.9 Grain center spacing histogram for stochastic grinding wheel model.

5.3 3D model vs. 2D model

In this section a comparison between the 3D material removal simulation and the 2D material removal simulation for the 3D and 2D wheel models will be presented. The 3D wheel models were constructed in a single row, which is similar to the one illustrated in Figure 5.3, for the same parameters used for the 2D models ("Constant wheel model" and

"All stochastic wheel model", see chapter 3). Table 5.1 lists the grinding and simulation parameters that were used in the simulation.

Table 5.1 The grinding and simulation parameters.

Parameter	Simple	Value	Unit
Depth of cut	a	$[0.01\ , 0.02\ , \ldots\ , 0.1]$	mm
Cutting speed	v_s	30000	mm/sec
Workpiece speed	v_w	100	mm/sec
Wheel diameter	d_s	200	mm
Grain diameter	d_g	0.253 (for constant model)	mm
Grain spacing	L	0.35 (for constant model)	mm
Time step factor	dt_f	1	--
Line segment density	δ_{ls}	1000	$line/mm$

5.3.1 3D constant model vs. 2D constant model

After the simulation in 2D and 3D had finished, the result for the uncut chip thickness and contact length for the 3D model was taken for only the middle slice of the 3D chip (refer to Figure 5.2) using Equation (5.12) and Equation (5.14), respectively. This step was taken to ensure that the 3D simulator provides the same result as the 2D model for the constant model. Figure 5.10 and Figure 5.11 plot the simulated uncut chip thickness and contact length versus the depth of cut for both 3D and 2D constant models. From the figures the differences were as small as 0.25% and 0.03% for the uncut chip thickness and contact length, respectively.

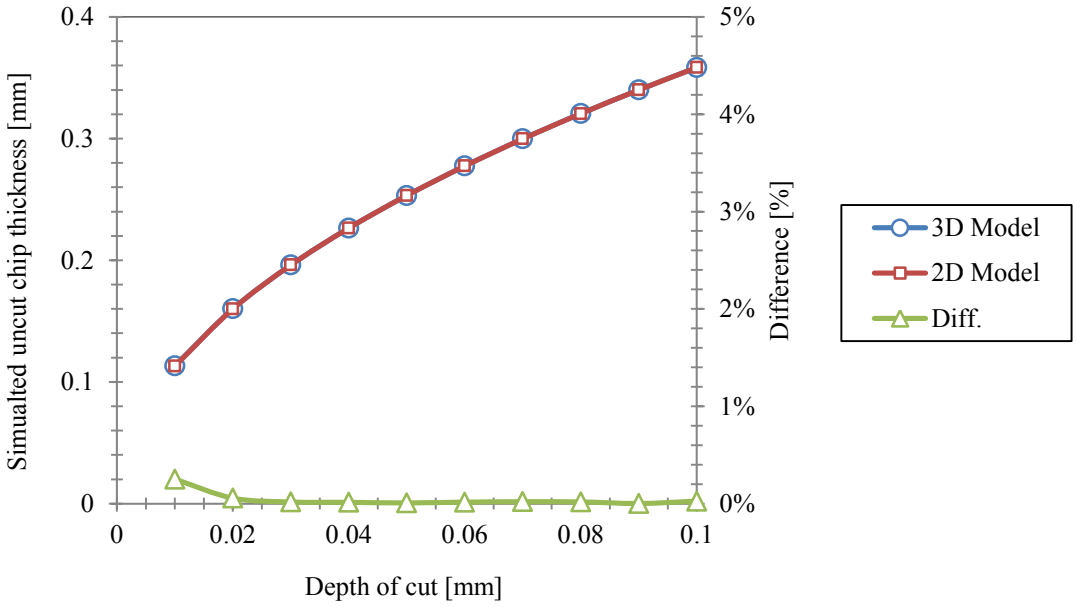

Figure 5.10 The uncut chip thickness for the "Constant" 3D and 2D models vs. the grinding depth of cut.

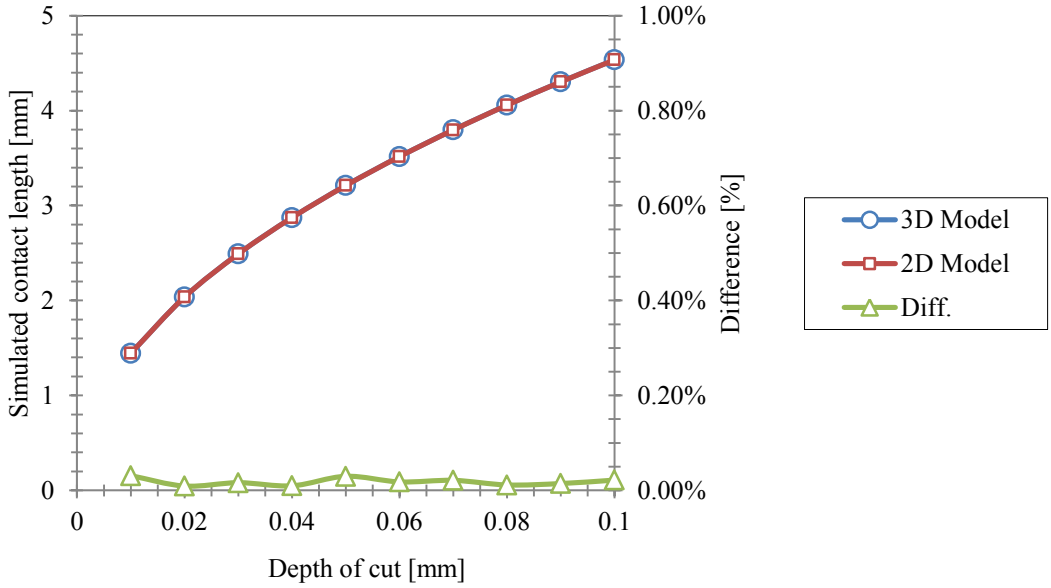

Figure 5.11 The contact length for the "Constant" 3D and 2D model vs. the grinding depth of cut.

5.3.2 3D All stochastic model vs. 2D All stochastic model

The simulated uncut chip thickness and contact length for the 3D model of "All stochastic" were calculated using Equation (5.13) and Equation (5.15), respectively. These equations calculated the average of the uncut chip thickness and contact length across the y-axis in the 3D chip as shown in Figure 5.2. The simulated uncut chip thickness and contact length versus the depth of cut for the 3D and 2D stochastic models are plotted in Figure 5.12 and Figure 5.13, respectively. The uncut chip thickness and contact length for both the 3D and 2D stochastic models behave in the same manner. As the cutting depth increases the uncut chip thickness and contact length increases; however, the differences rapidly increase with the depth of cut. At depth of cut of 0.1 mm the differences for the uncut chip thickness and contact length were 60.3 % and 19.7 %, respectively.

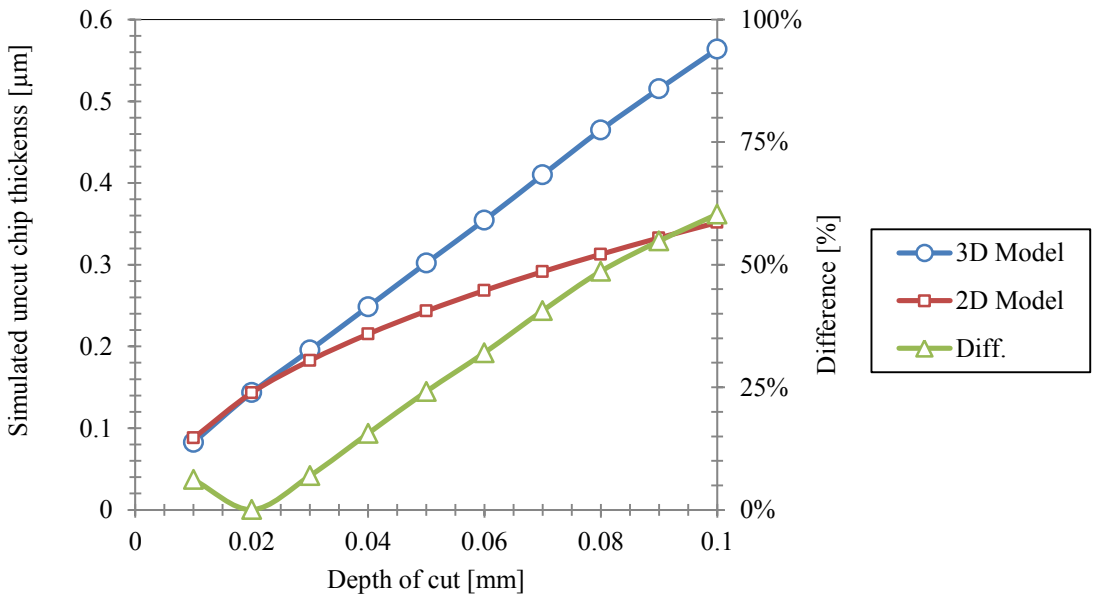

Figure 5.12 The uncut chip thickness for the "All stochastic" 3D and 2D models vs. the grinding depth of cut.

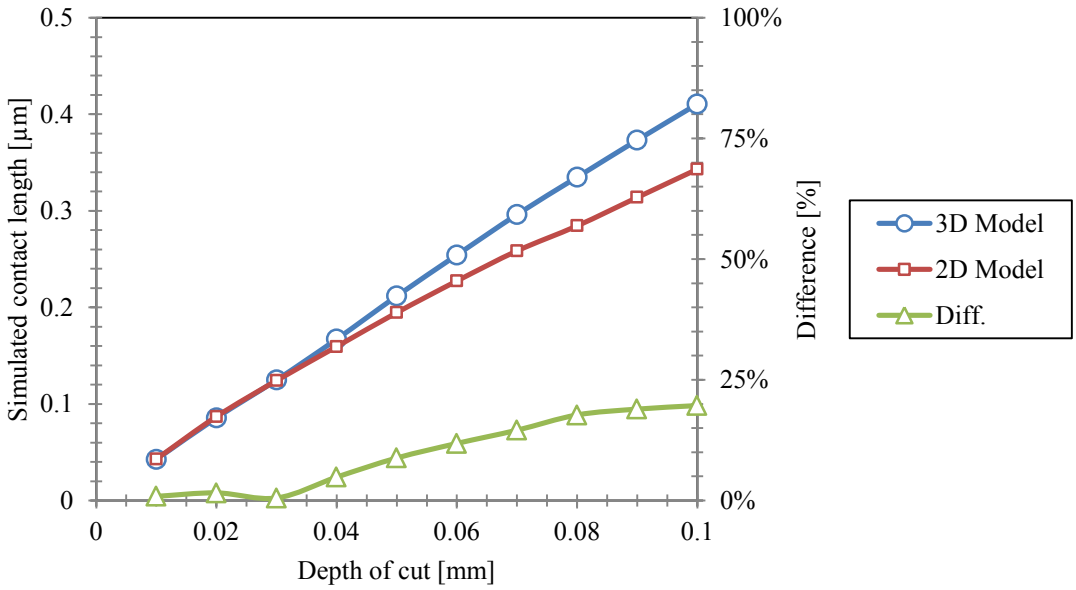

Figure 5.13 The contact length for the "All stochastic" 3D and 2D model vs. the grinding depth of cut.

To explain this difference, the uncut chip thickness and contact length for a single grain from the 3D "All stochastic" model (grain number 203) versus the grain width was plotted in Figure 5.14. In the middle of the grain the values of the uncut chip thickness and contact length were zero, but on the sides both the uncut chip thickness and contact length had positive values. The reason for this observation is that there was another active grain, which was smaller in size but with a larger protrusion height than grain 203, which cut the workpiece just before grain 203. The small grain cut the workpiece material from the middle and left some material on the sides for grain 203. A 2D model could be constructed from the 3D model by taking a section through the bottom dead center of the grain. This 2D model is represented by the vertical dashed line in Figure 5.14. Since the 2D model only considered one point on the grain width, grain 203 would be considered inactive in the 2D model. Therefore, when calculating the average uncut chip thickness and contact length it is not surprising that the results for the 2D model are smaller than

the results for the 3D model because the grain may be cutting the workpiece in an off centered manner.

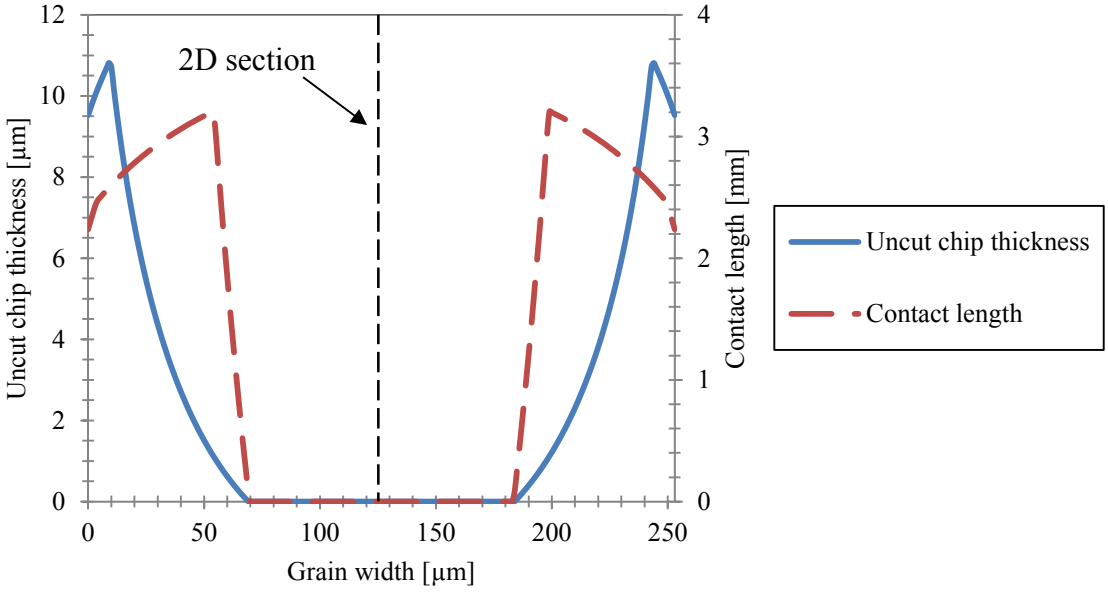

Figure 5.14 Uncut chip thickness and contact length for a single grain in the "3D All stochastic" model vs. the grain width.

5.4 3D simulation challenges

Performing the simulation on a typical desktop computer was time consuming. The 2D simulations were carried on a computer that has an "Intel(R) Core(TM)2 Quad CPU, 3.4 GHz" processor and 4.0 GB of RAM. With this type of computer the simulation took from 2 to 4 hours for the 2D metal removal simulation and 4 to 5 days to develop a 3D wheel model. To reduce the solution time, the 3D simulation code was converted into parallel code so it could run on ACEnet (Atlantic Computational Excellence Network).

The Atlantic Computational Excellence Network is a consortium of nine Atlantic Canada institutions with large scale high-performance computing (HPC) facilities for research. The nine institutions include: Memorial University of Newfoundland, University of New Brunswick, Mount Allison University, Dalhousie University, St. Francis Xavier University, Saint Mary's University, the University of Prince Edward Island, Cape Breton University, Mount St. Vincent University and Acadia University. The HPC resources are

connected by several Optical Regional Advanced Networks (ORAN's) with links of various speeds up to 10 $gigabits/second$.

The simulation was converted to parallel code by slicing the 3D model into a number of thin 2D models as shown in Figure 5.15, and then running each model on a single CPU on a supercomputer cluster. The converted 2D model is referred to as 2D-slice model to distinguish between the converted 2D model and the 2D model that was developed in Chapter 4. When all 2D-slice simulations finished, the 2D-slice results were collected for the 3D result as illustrated in Figure 5.15. The accuracy of the 3D result depends on the distance between each two 2D-slices. In order to achieve the targeted accuracy of the simulation, the number of 2D-slices must be equal to the number of line segment in the y-axis. Equation (5.23) was used to define the number of 2D-slices based on the line segment density δ_{ls}.

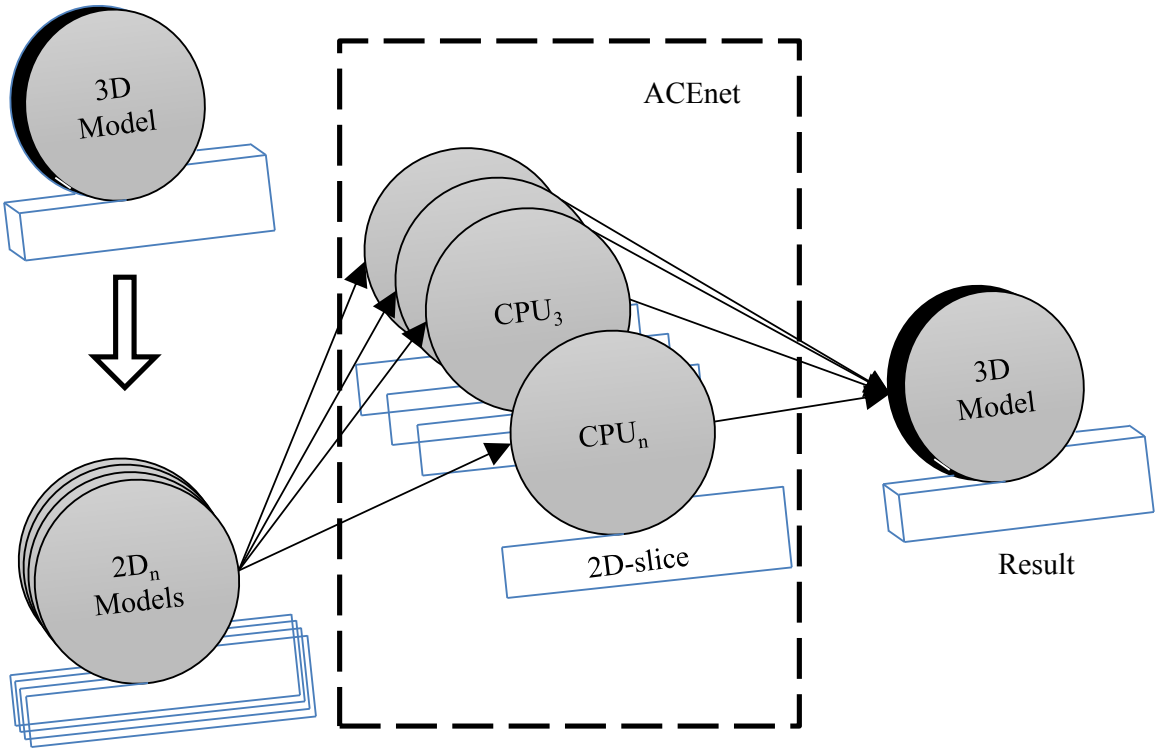

Figure 5.15 Illustration of the converting the 3D simulation into 2D and converting back to 3D.

$$number\ of\ slices = \delta_{ls} \times workpiece\ width \tag{5.22}$$

Performing the 3D simulation by converting the 3D model into several 2D models on the ACEnet clusters required from two hours to one day depend on the number of computers in the clusters that were available.

5.5 Result and discussion

Simulations of grinding metal removal were carried out using the following parameters for both the non-stochastic and stochastic wheel models: depth of cut from $0.02\ mm$ to $0.1\ mm$, wheel diameter of $354.04\ mm$, wheel speed of $30.0\ m/s$ and workpiece speed of $100\ mm/s$.

Figure 5.16 and Figure 5.17 plot the uncut chip thickness and contact length as a function of depth of cut for both the "Simulated" results for the non-stochastic model and the "Analytical" results obtained from the following equations [2]:

$$l_c = \sqrt{ad_s} \tag{5.23}$$

$$h_m = 2L\left(\frac{v_w}{v_s}\right)\left(\frac{a}{d_s}\right)^{\frac{1}{2}} \tag{5.24}$$

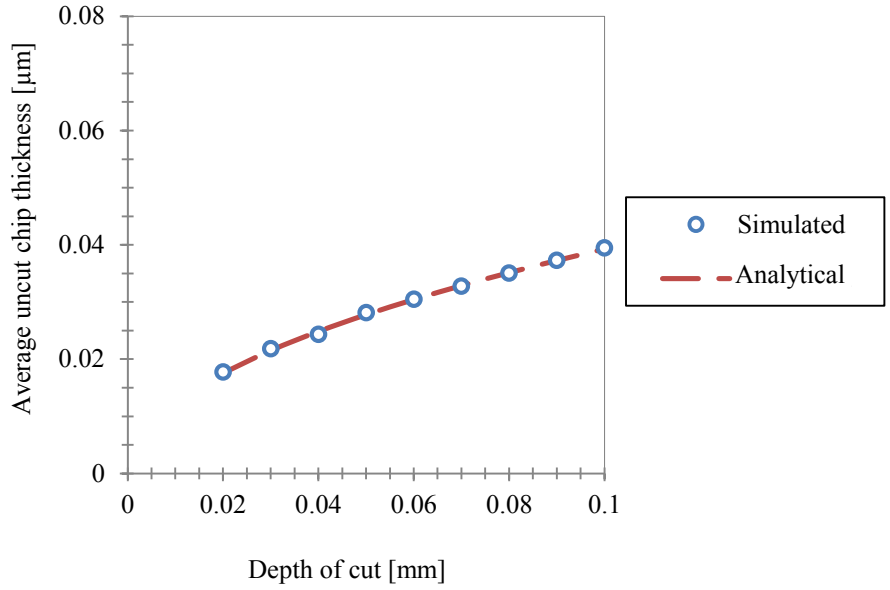

Figure 5.16 Simulated and Analytical uncut chip thickness vs. the depth of cut for the non-stochastic model.

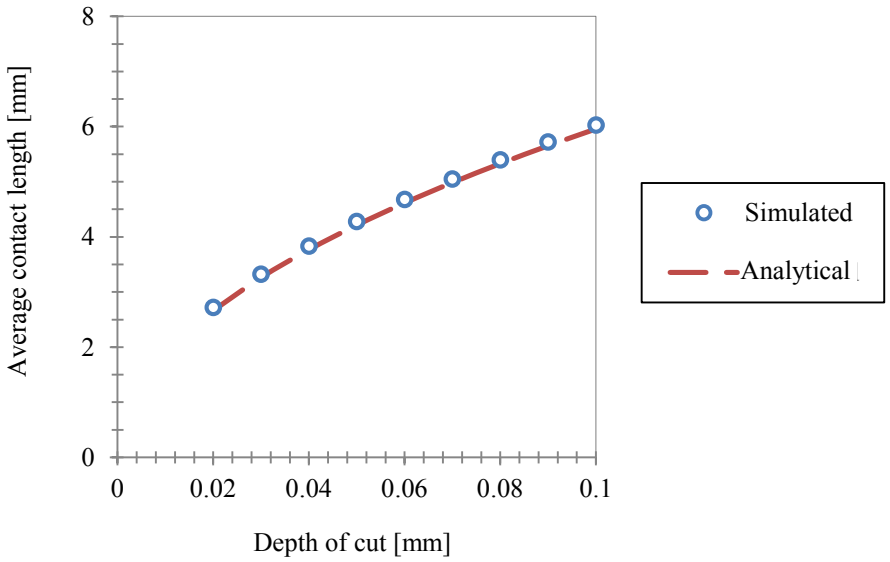

Figure 5.17 Simulated and Analytical contact length vs. the depth of cut for the non-stochastic model.

The purpose of these figures was to demonstrate that the simulation with the non-stochastic grinding wheel model could replicate the result produced by the analytical approach given the same underlying assumptions that all grains were the same size, had the same protrusion height and were equally spaced around the grinding wheel. These two figures show an excellent agreement between the simulation and analytical results. The differences in the uncut chip thickness and contact length were 0.5% and 1.2%, respectively, for a depth of cut $0.1\ mm$, and 1.2% and 2.2%, respectively, for a depth of cut of $0.02\ mm$. From this comparison one can conclude that the proposed simulation is as least as accurate as the analytical approach.

Next, the simulation using a stochastic wheel model was compared to experimental results. The grinding parameters in the experiment were the same as the grinding parameters used in the simulation. Since the grinding wheel model has not been dressed, the grinding wheel used in the experiment was crushed by a rotary diamond roll. The purpose of using this dressing method is to produce or expose new abrasive grains that have not fractured. This dressing condition can be achieved by using large dressing ratio (1.0 or more) [8, 9]. The dressing amount was also selected to ensure that worn abrasive grains (caused by previous grinding) are removed. The dressing parameters were as follows: dressing ratio was 1.1, dressing in-feed velocity was $3.05 \times 10^{-3} mm/rev$ and dressing amount was $0.165\ mm$. This process was repeated twice. The workpiece material type used in the experiment was AISI 1018 Steel.

Figure 5.18 shows the simulated workpiece surface roughness and the resulting surface finish for a depth of cut of $0.09\ mm$. A Nanovea PS-50 non-contact optical profilometer was used to measure the surface topology of the experimental workpieces. The simulation was terminated when the wheel was fully engaged with the workpiece and had continued to rotate an additional two rotation to make sure that the simulation had reached steady state. The simulated surface was then imported into the same software used to analyze the surface of experimental workpieces to ensure that there were no discrepancies in the analysis. Figure 5.19 shows an experimental and simulated profile of the ground surface and Figure 5.20 shows the height distribution of the profiles. While

the profiles are clearly not identical there are some remarkable similarities. The roughness Ra of the experimental and simulated profiles are $1.9\,\mu m$ and $2.1\,\mu m$, respectively, and the height distribution appears normally distributed with a range from $-9\,\mu m$ to almost $7\,\mu m$. The main difference between the two profiles is that the experimental data appears to have slightly higher frequency content than the simulated data. This discrepancy is likely the result of the fact that real grains may have multiple cutting edges and the simulation does not account for plowing of workpiece material to the sides of the grains. Nevertheless it should be emphasized that no tuning of the model was required to obtain excellent agreement between the simulated and measured surface roughness values.

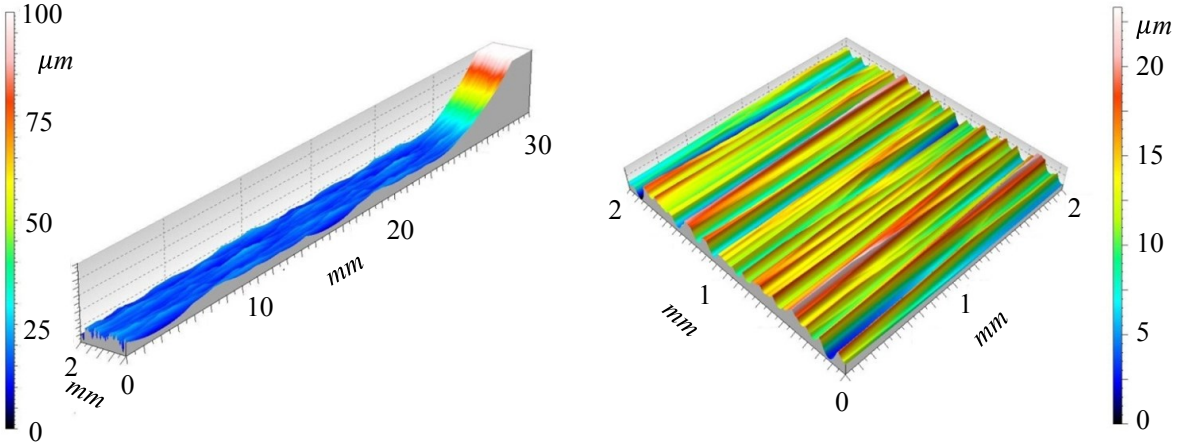

Figure 5.18 Sample of simulated workpiece data.

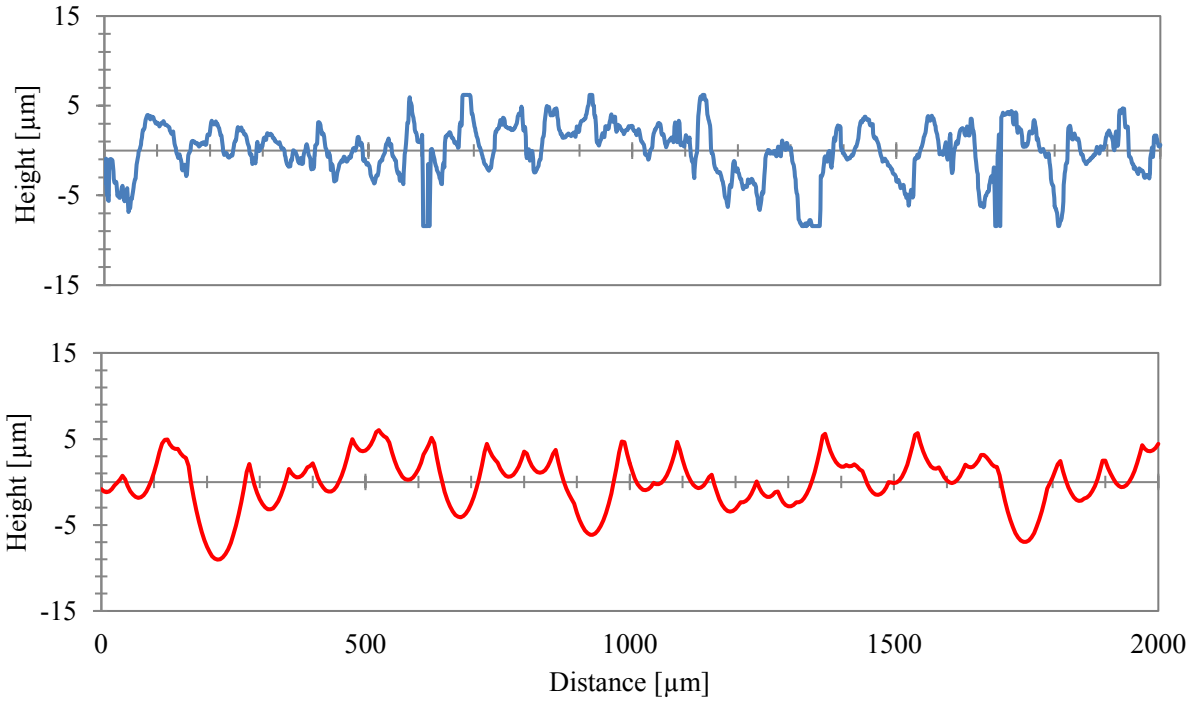

Figure 5.19 Experimental (above) and the simulated (below) profiles of the workpiece.

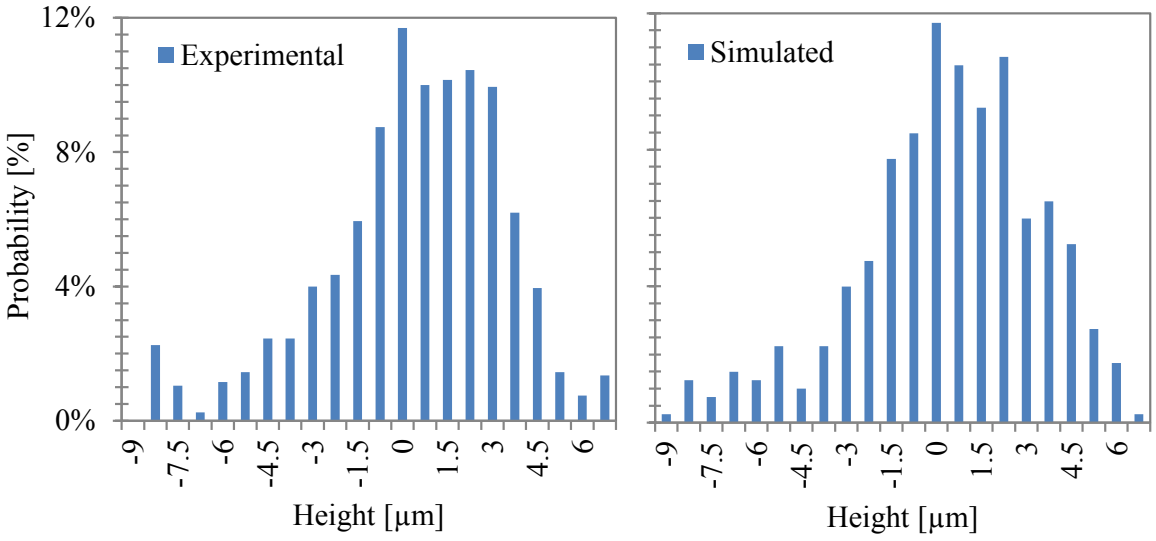

Figure 5.20 The histogram of the profile height for the experimental and simulated profiles.

The author believes that the ability to calculate instantaneous metal removal is one of the chief advantages of this approach as it opens the door to better force and power models for grinding. For example, Figure 5.21 shows the simulated instantaneous material removal rate for one complete revolution of the $2\ mm$ wide wheel at a depth of cut of $0.09\ mm$. The simulated material removal rate is the summation of material removed by the cutting operation divided by the elapsed time. The average simulated MRR is $18\ mm^3/sec$ while the material removal rate calculated by multiplying the workpiece width by the depth of cut by the workpiece velocity is also $18\ mm^3/sec$ confirming that the bulk metal removal is being simulated correctly.

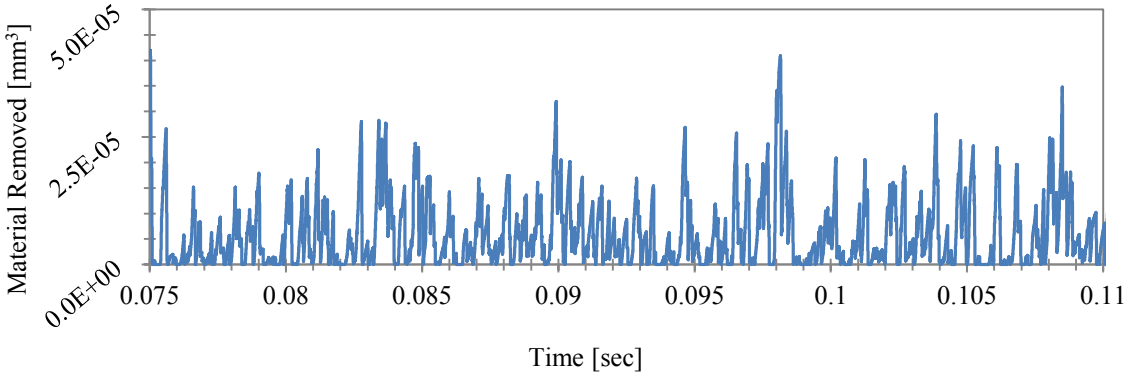

Figure 5.21 Simulated material removed vs. time.

The simulation also makes it possible to map the uncut chip thickness onto individual cutting edges. Figure 5.22 shows the uncut chip thickness for every single active grain on a $200\ mm$ section of the wheel surface for a depth of cut of $0.09\ mm$. From this figure it is possible to conclude that most of the material removal has been accomplished by relatively few grains. The range of uncut chip thicknesses produced by the stochastic model is huge – the minimum value was $0.0\ \mu m$, while the maximum value was $17.9\ \mu m$, and the standard deviation was $2.1\ \mu m$ because only 21.4% of the grains are actually cutting! This information is critical for those researchers that are conducting finite element simulations of grinding micro-mechanics who need accurate estimates of the uncut chip thickness in order to perform useful simulations.

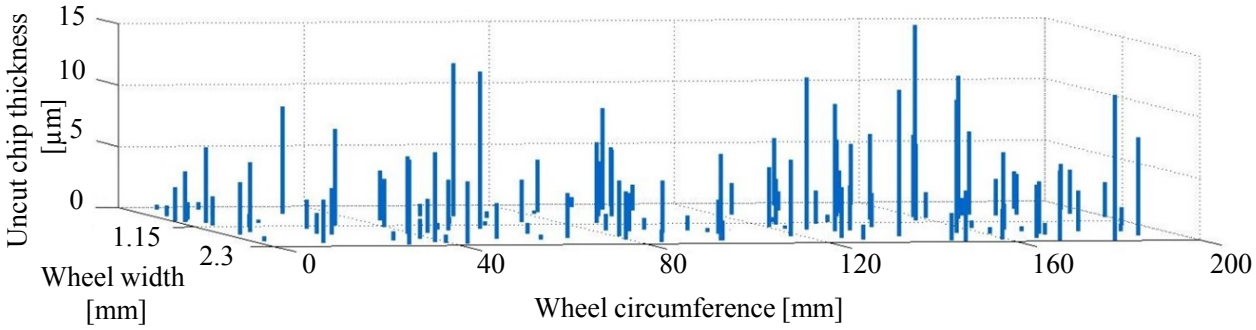

Figure 5.22 The simulated uncut chip thickness for every active grain for a 200 mm long section of the grinding wheel.

Figure 5.23 and Figure 5.24 plot the resulting average uncut chip thickness and the average contact length as a function of the depth of cut using simulated results from the stochastic model as well as the analytical results obtained from Equation (5.23) and Equation (5.24). Several observations can be made from these figures. The analytical and the stochastic models behaved in roughly the same manner. As the depth of cut increased the average uncut chip thickness and the average contact length increased. However, the differences between the simulated and analytical uncut chip thickness results are slightly larger than the differences in the contact length results. At the depth of cut of $0.1\ mm$ the difference between the simulated and analytical uncut chip thickness and contact length is 95.7 % and 89.6 % , respectively.

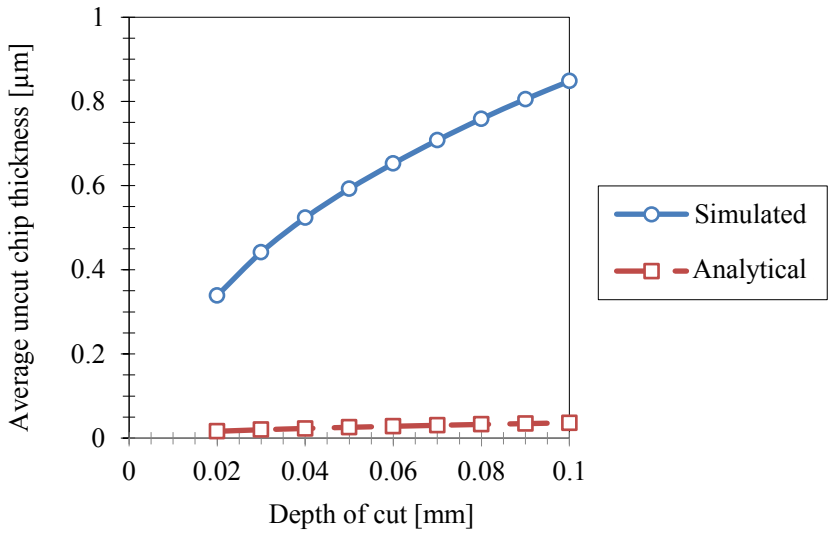

Figure 5.23 The Simulated and Analytical uncut chip thickness vs. the depth of cut.

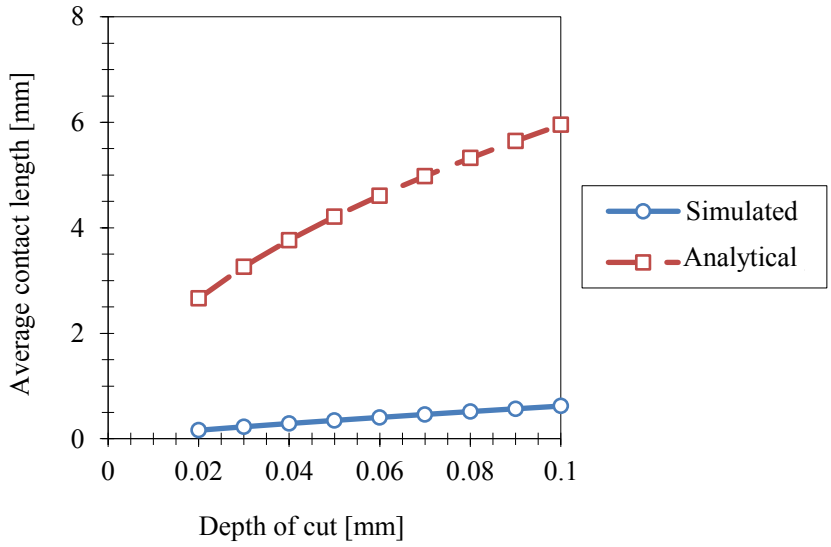

Figure 5.24 The simulated and Analytical contact length vs. the depth of cut for the stochastic model.

The difference between the average uncut chip thickness and contact lengths determined via the simulation and the analytical approach can partially be attributed to the difference

between the number of active grains actually participating in cutting. This difference is quantified by Figure 5.25, which shows the percentage of active grains versus the depth of cut for the stochastic model. The percentage of the active grains increases as the depth of cut increases, because more grains that have a small protrusion height participate in the cutting operation. This figure shows that the number of active grains is quite small and ranges from about 11% to 22%. Given that the number of active grains has a significant effect on the uncut chip thickness and contact length, it make sense to calculate the uncut chip thickness and contact length for the number of active grains for both the simulation and analytical approach as can be seen in Figure 5.26 and Figure 5.27. When this correction is made, the discrepancy between the simulated and analytical values drop; however, the simulated results still suggest that the chips are still about twice as thick and half as long as the standard analytical calculation would predict. These differences are likely due to the assumption of constant grain spacing and protrusion height made in the analytical solution.

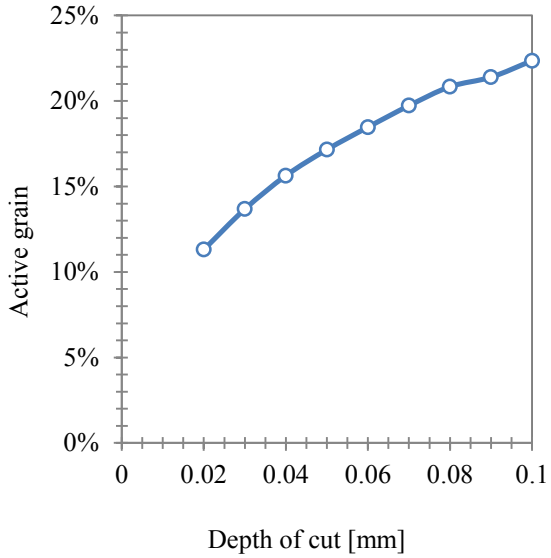

Figure 5.25 Grain active vs. depth of cut.

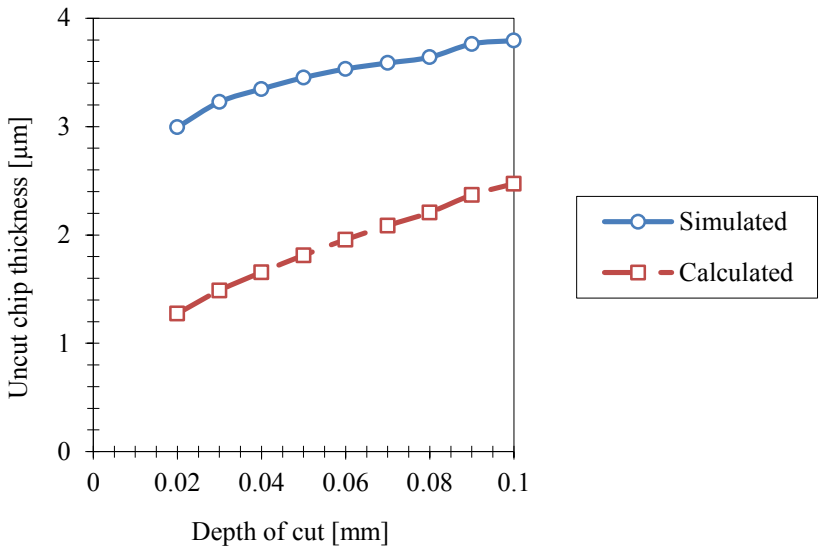

Figure 5.26 The effect of the number of active grain on the simulated uncut chip thickness.

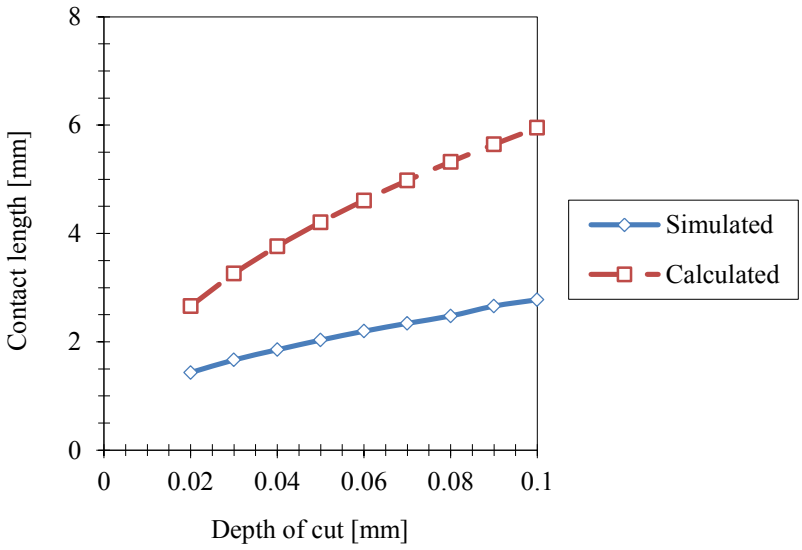

Figure 5.27 The effect of the number of active grain on the simulated contact length.

5.6 Summary

A novel simulation-based method of calculating the uncut chip thickness, the contact length, and surface roughness in grinding was presented in this chapter. The model was generated based solely on the wheel markings and process parameters, without the use of

a dressing operation. Grinding experiments were carried out to demonstrate that this novel approach was able to accurately predict the workpiece surface roughness. The grinding wheel was crushed by a diamond rotary roll to produce abrasives grains that have not fractured. The simulation was also shown to be able to calculate instantaneous material removal rates, and map chip geometry information to individual grains on the grinding wheel. It was decided to develop a dressing model to dress the grinding wheel model; therefore, information about grinding wheel topography was required. In the following chapter, an automated non-contact 3D wheel scanning system that is capable of measuring grinding wheels in a non-destructive and rapid manner is presented.

CHAPTER 6. CHARACTERIZATION OF GRINDING WHEEL SURFACE TOPOLOGY USING A WHITE CHROMATIC SENSOR

6.1 Introduction

In Chapter 5 the grinding wheel model was not dressed due to the lack of a suitable dressing model and inadequate information about grinding wheel topography such as cutting edge density, size and spatial distribution. In the present chapter, an automated, non-contact, 3D wheel scanning system that is capable of measuring grinding wheels in a non-destructive and rapid manner is presented. This system incorporates a white light chromatic sensor with a custom-designed wheel positioning system and it was used to determine the effect of dressing feed on the grinding wheel topography of an aluminum oxide grinding wheel. For each dressing feed the cutting edge size, spacing and protrusion height distributions were determined.

6.2 Measurement principle:

The principle of the white-light axial chromatic depth scanning technique was first introduced by Molesini *et al*. [65]. With this measurement technique, white light passes

through a lens with a high degree of chromatic aberration separating the light into its constituent colors (wavelengths) as illustrated in Figure 6.1. Each wavelength of the white light is focused at a different distance from the lens. The wavelength of light that is focused on the object of interest will be reflected back through the lens while the out-of-focus wavelengths will tend to be scattered. By identifying the wavelength of light that returns to the sensor it is possible to infer the distance the object is from the lens via the focal distance of the reflected wavelength of light.

6.2.1 Advantages associated with the chromatic aberration technique

The advantages that are associated with the chromatic aberration technique are:

- Excellent spatial resolution, regardless of ambient illumination.
- Zero influence of sample reflectivity variations.
- Appropriate for: transparent/opaque, specular/diffused and polished/rough materials.
- No sample preparation required.
- Relatively high measuring range with nanometer resolution.
- No physical contact with the measured object required.
- The data acquisition rate varies from 30 Hz up to 30 KHz, which leads to fast scan process.

There is, however, a limitation when using the axial chromatic technique, which is the difficulty to measure surfaces with steep angles.

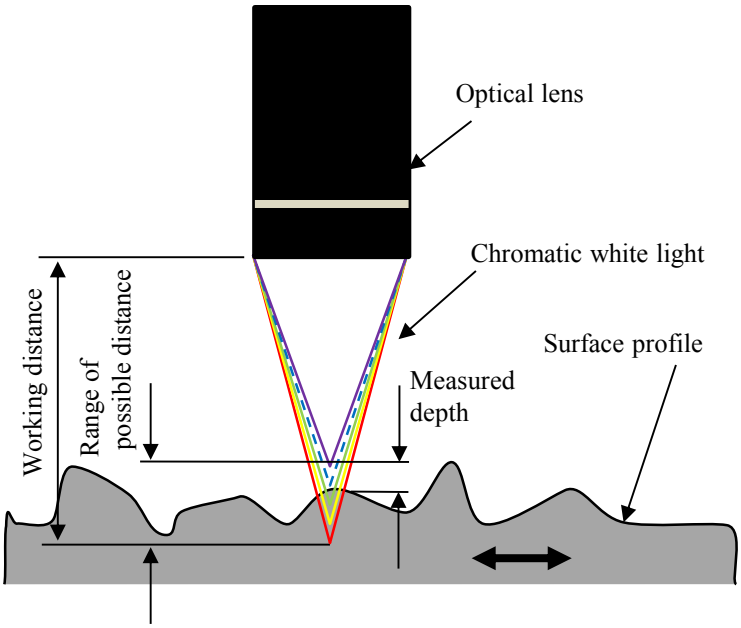

Figure 6.1 The white light axial chromatic technique.

6.3 Experimental apparatus

The heart of the unique grinding wheel scanning system developed for this research is a Nanovea CHR150 white light chromatic sensor with a 1200 μm optical pen. This sensor gives the wheel scanning system a measurement range of 1200 μm, a depth accuracy of $\pm 200\ nm$, a depth resolution of $\pm 25\ n$, a maximum planer resolution of 1 μm and a range of sampling rates between 30 and 1000 Hz. The grinding wheel scanning system was designed to position the optical pen relative to the grinding wheel using a horizontal stage, a vertical stage and a rotary stage as shown in Figure 6.2.

The manually-operated horizontal stage is used to bring the optical pen into measurement range of the grinding wheel surface and can accommodate grinding wheels from 10" (250 mm) to 20" (500 mm) in diameter. Also shown in Figure 6.2 is a second horizontal stage that is used to adjust a light source and illumination lens so that digital images can be taken of the wheel surface. The vertical stage is used to automatically control the axial position of the optical pen during surface measurements and consists of a Parker Series

4000 stage with a ZaberTLA28A linear actuator having a range of 28 mm and a step size of 0.1 μm. The rotary stage was custom built for this application. It consists of a vertical spindle with a number 40 taper at the top to receive a grinding wheel mounted in a flange. The angular position of the grinding wheel is determined using a 48,000 (in quadrature mode) line count Teledyne-Gurley Series 825 rotary encoder attached to the bottom of the grinding wheel spindle. The grinding wheel is automatically rotated at constant velocity by a friction wheel pressed against the circumference of the grinding wheel. The friction wheel is driven by a SILVERPAK 17C stepper motor with a 51: 1 planetary gear box and can drive a 16" (400 mm) grinding wheel from 1 $\mu m/sec$ to 10 mm/sec. By adjusting the white light chromatic sensor's sampling rate and the rotational speed of the grinding wheel it was possible to measure the surface of a 16" (400 mm) grinding wheel at 1 μm intervals. The entire system was computer controlled using a custom LabView software program.

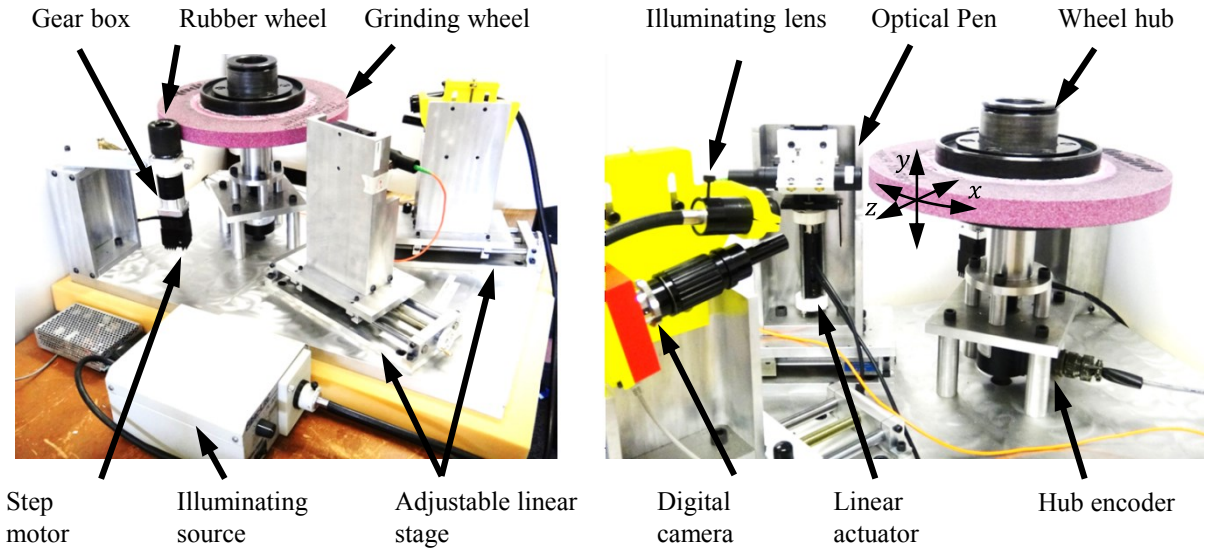

Figure 6.2 3D grinding wheel topography apparatus.

6.3.1 The rotary encoder

The rotary encoder is an electromechanical device that converts the angular position of the grinding wheel to a digital code. The rotary encoder used in the apparatus was an optical incremental type, which provides cyclical outputs when the grinding wheel is rotated. The optical encoder's disc is made of glass or plastic with very small transparent windows as shown in Figure 6.3. Two sensors, A and B, are attached to the encoder to generate pulses as the light passes through the transparent windows in the rotary disc. Sensor A and B are place so that their pulses are 90 degrees out of phase as shown Figure 6.4.

Since the pulses are generated when the light passes through the transparent windows on the rotary disc, the pulse's width will represent the width of the transparent widows. During the encoder test, it was found that the width of the encoder pulses is not constant. While the wheel was rotated at a constant speed, the encoder outputs (sensor A and B) were measured by an oscilloscope. Then the output of the channel A and channel B (volts) were plotted versus time as shown in Figure 6.4. From the figure, it can be clearly seen that the pulse widths are not constant. Channel A and B are connected together by the logical operator "AND" to provide higher encoder resolution. The logical operator "AND" results in a zero value only when both channels A and B have zero values, otherwise the result is 1, as shown in Figure 6.4. From the figure the pulse width at time 0.000125 second is about twice of the pulse width at time 0.0002 second.

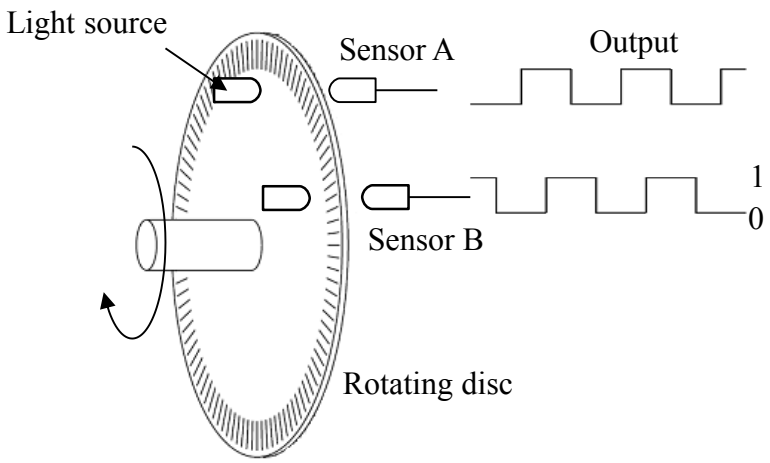

Figure 6.3 Rotary encoder.

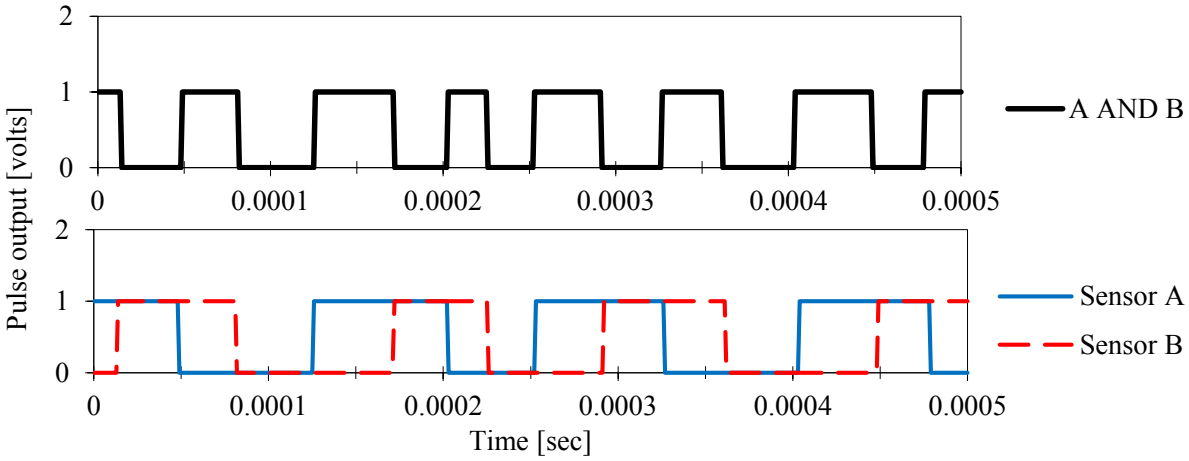

Figure 6.4 The pulses at the encoder output.

If the pulse width of the rotary encoder is not constant, the measured profile can be misshaped because the sampling interval is proportional to the sampling frequency and the pulse width. To explain the effect of the pulse width on the measured profile, a surface that has sinusoidal shape and $10\,mm$ length is assumed to be measured. In this example the changes in the pulse width will be simulated by the changes in the sampling interval, which can be caused by the speed of measuring tool. The measuring tool moves over the surface with a constant speed of $100\,mm/sec$ and a sampling frequency of

100 Hz. In this case the sampling interval, which is the distance between successive measured points, is constant and is equal to 0.1 mm. The result of this measurement is plotted in Figure 6.5 (a). Assume the measuring tool begins with a speed of 50 mm/sec and then the speed increased to 200 mm/sec while the sampling frequency remained constant at 100 Hz. Thus the average of the speed of the measuring tool is 100 mm/sec and the overall sample interval is 0.1 mm. The measured profile obtained by this sampling interval, however, is misshaped (stretched in the beginning and compressed at the end) as shown in Figure 6.5 (b).

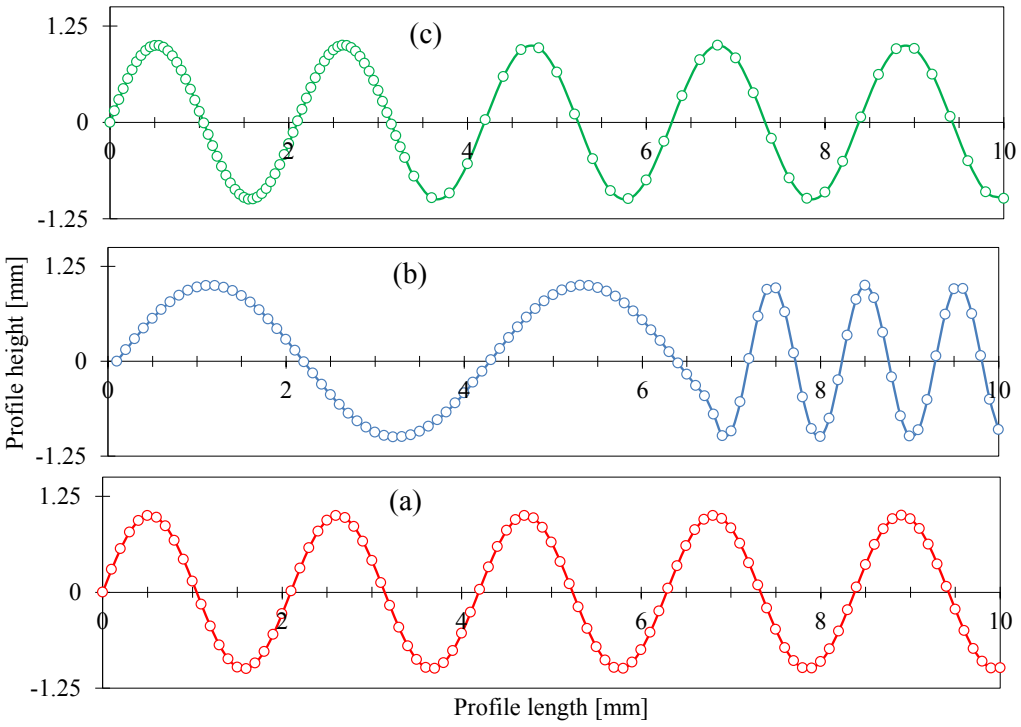

Figure 6.5 Sinusoidal profile (a) constant measuring speed and constant sampling interval, (b) different measuring speed and constant sampling intervals and (c) different measuring speed and different sampling interval.

To resolve this problem, the sampling interval should be calculated for each speed of the measuring tool. Thus, the sampling interval for the first speed will be 0.05 mm

and $0.2\ mm$ for the second speed. Figure 6.5 (c) plots the sinusoidal profile in good shape with different sampling intervals. As shown in this example, the sampling interval was calculated for each pulse of the rotary encoder, as will be explain in the following section.

6.4 Data conditioning

Grinding wheel topography measurements consisted of a set of profiles around the circumference of the grinding wheel with x being the circumferential direction, y being the axial direction and z being the radial height measurement. Data conditioning was needed to correct for any kinematic inaccuracies in the apparatus, small misalignments of the grinding wheel when mounted in the fixture, reassembling the measured profile when the sampling interval is not constant, and to fill in missing data points or to correct erroneous data points captured by the white light chromatic sensor.

Because the rotary encoder has an uneven pulse width, the sampling interval was calculated for each pulse. A test part was attached to a grinding wheel for evaluation purposes. Figure 6.6 (a) plots a profile height from the test part versus the grinding wheel circumference as measured by the rotary encoder pulses. The average of pulse width b_p was $23.5\ \mu m$. The following equation was used to calculate the average of pulse width.

$$b_p = \frac{\pi\ d_s}{N_p} \tag{6.1}$$

where N_p is the number of pulses per wheel revolution. In Figure 6.6 (a) the details of the measured profile is lost because a number of measured heights were sampled and plotted at the same value of wheel circumference (or encoder pulse). To avoid the misshaping of the measured profile, the sampling interval was calculated for each pulse and then the profile was resampled based on the new sampling intervals. The sampling interval for each pulse δ_p was calculated using the following equation:

$$\delta_p = \frac{b_p}{n_p} \tag{6.2}$$

where n_p is the number of samples per pulse. Figure 6.6 (b) plots the resampled measured profile.

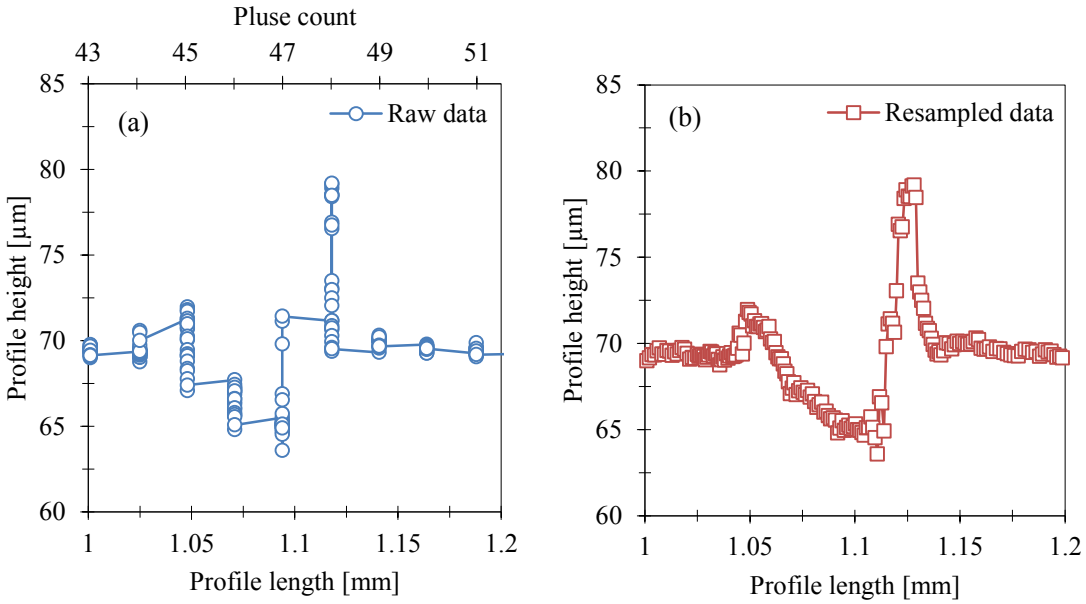

Figure 6.6 (a) Raw measured profile (b) resampled measured profile.

Because of small fixture misalignments of the grinding wheel and axial run out of the spindle bearings, a sinusoidal wave can be seen in the measured data having a wavelength that corresponds to the wheel circumference as shown in the upper plot of Figure 6.7. A sinusoidal curve was fit to the data and subtracted from the measurements using Equation (6.3) to remove the axial run out from the data as follows:

$$z' = z - A\,sin\left(\frac{2}{d_s}x + \emptyset\right) \tag{6.3}$$

where A is the amplitude, $\emptyset$ is the phase angle, and d_s is the grinding wheel diameter. The lower plot of Figure 6.7 shows the results of the correction of this run out effect. Next, the grinding wheel topography profiles were assembled into a surface. At this stage any additional kinematic errors in the system due to axis misalignment or mounting of the grinding wheel are minimized using the leveling function in the Mountains 3D analysis software. With this software, a plane is fit through the data using the least-squares method and the data is then rotated until the normal to the fitted surface is collinear with the z-axis.

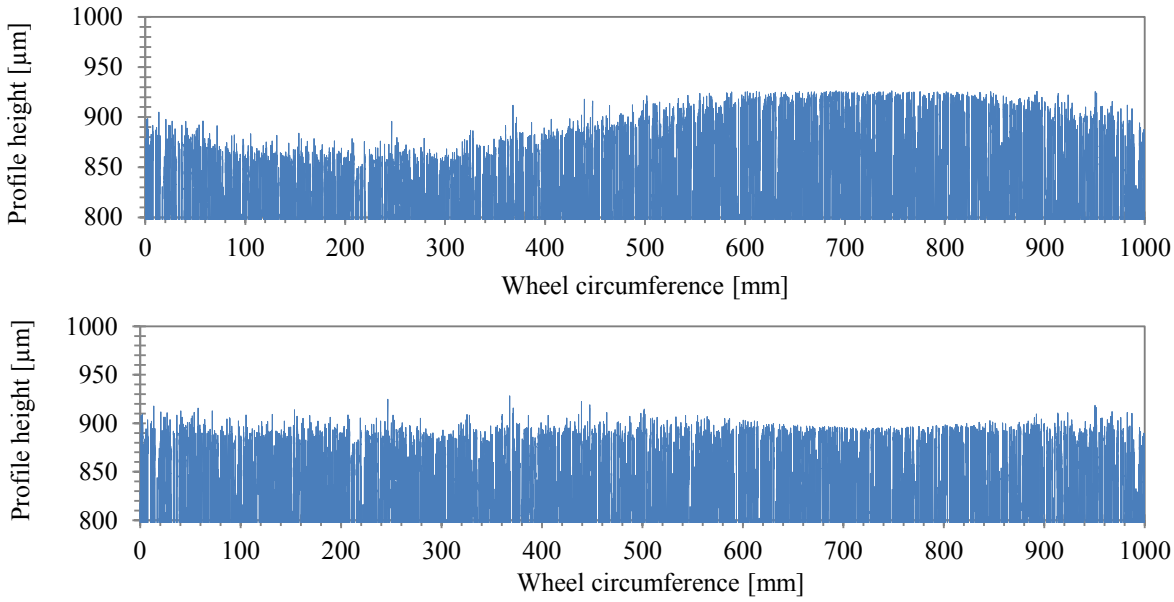

Figure 6.7 2D profile of the grinding wheel, Top: before the correction of run out effect, Bottom: after the correction.

Next, a hole-filling operation was used to fill in any missing data points. A point on the wheel surface may not be measured if, for example, insufficient light is reflected back from the surface or a pore in the grinding wheel surface was deeper than the white light chromatic sensor's measurement range. Thus, the hole filling function available in Nanovea's Mountains 3D Analysis Software was used to fill in holes by blending the points surrounding a hole as shown in Figure 6.8.

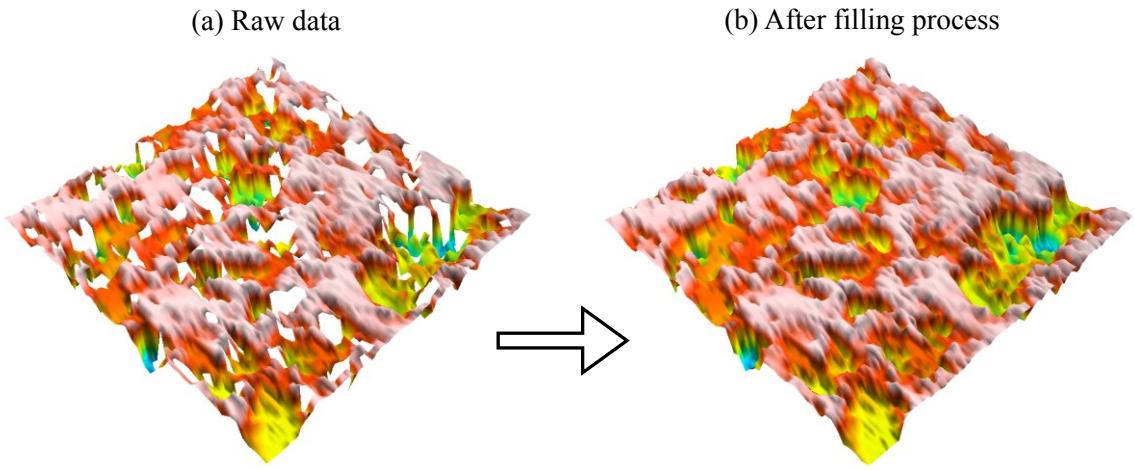

Figure 6.8 Hole filling process (a) before the process, (b) after the process.

Finally, measurement noise that took the form of spikes in the measurements in the data, as shown in Figure 6.9 (a), was modified. Figure 6.10 plots the Abbott-Firestone curve, which presents the bearing ratio curve of the measured surface. This curve shows, for a given surface depth, the percentage of material traversed in relation to the area covered. This function is a cumulating function of the amplitude distribution function. As can be seen in Figure 6.10, up to a depth of 382.2 µm, only 0.1% of the measured surface is accounted. This percent of measured surface manifested itself as spikes and were truncated as shown in Figure 6.9 (b) using the threshold function that available in Nanovea's Mountains 3D Analysis Software.

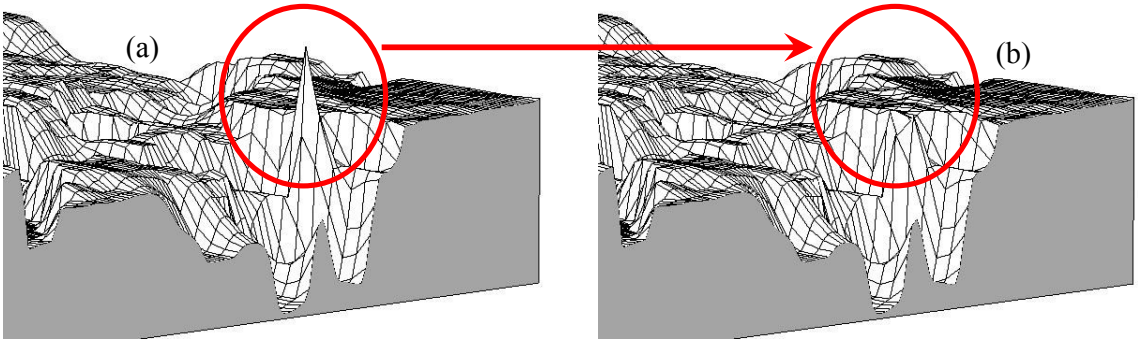

Figure 6.9 Threshold command (a) before and (b) after.

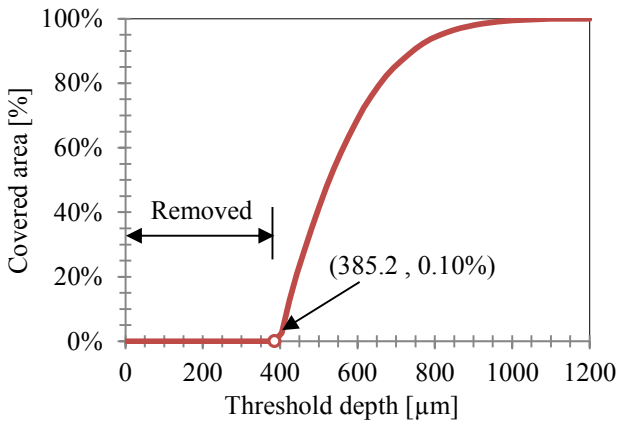

Figure 6.10 The Abbott-Firestone curve of the measured surface.

6.5 Validation experiments

Validation experiments were carried out on a test surfaces to confirm that the grinding wheel scanner developed in this research has the required positional accuracy and resolution to measure a grinding wheel (not to confirm that the optical sensor and pen were performing as specified by the vender). The code "SSM-80", stamped on a thin sheet of metal, was measured using the new grinding wheel scanner as well as with a HITACHI S-4700 Scanning Electronic Microscope and a Nanovea PS50 profiler as shown in Figure 6.11. This test surface was selected because it is of similar size to the grinding wheel patches that the wheel scanner was intended to measure. Note that three SEM images were required to measure the entire test surface due to the SEM's limited measurement range. Eight vertical (y-direction) and twenty-four horizontal (x-direction) measurements were taken at identifiable features on the test surface. The location of some of these in-plane measurements along the x-axis (x_i) and y-axis (y_i) are superimposed on the composite SEM image shown in Figure 6.11 (a), while Figure 6.11 (b) shows the 3D measurement results from the new grinding wheel scanning system. In the case of the 3D measurements, the same depth was used to take the in-plane measurements for the grinding wheel scanner and the Nanovea PS50 profiler.

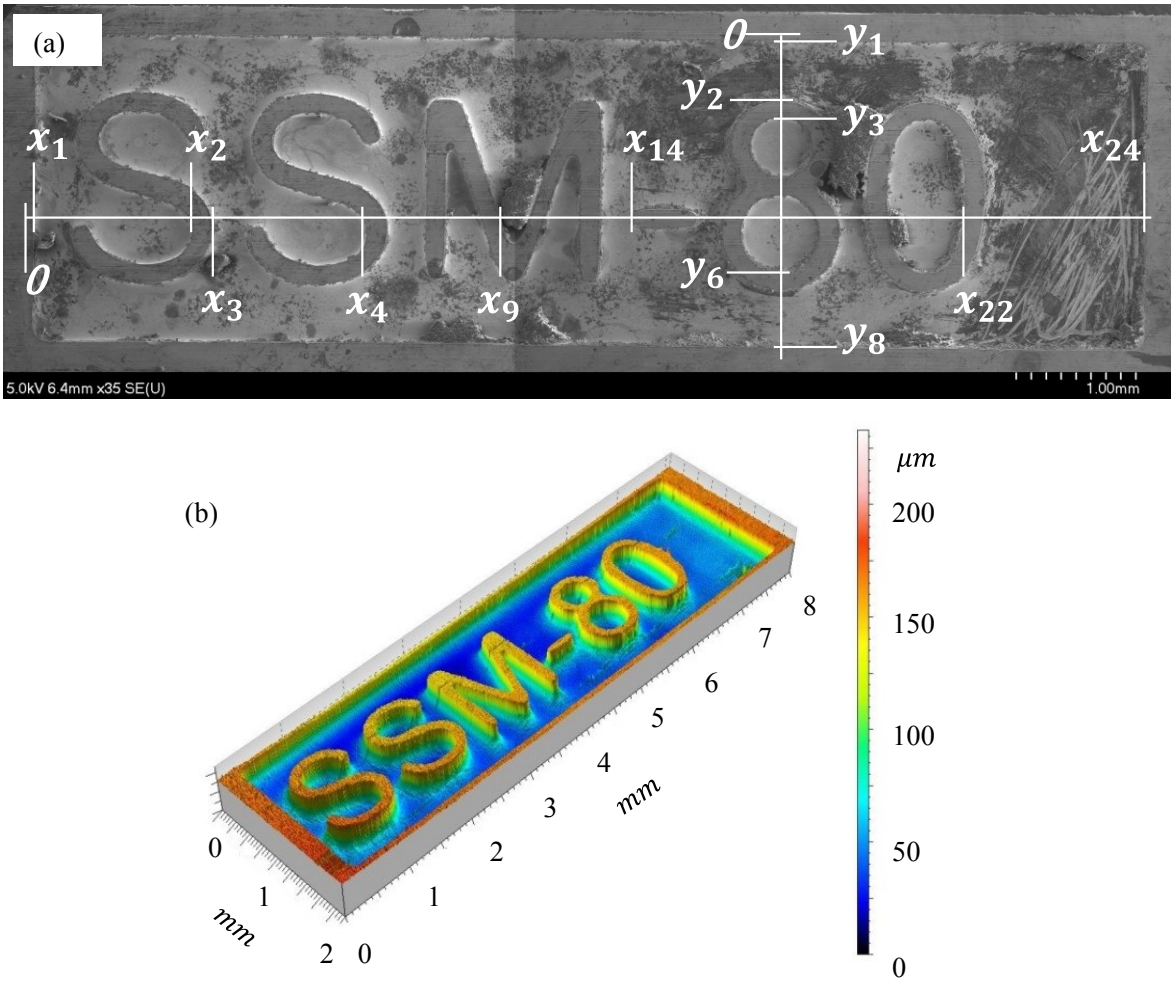

Figure 6.11 “SSM-80” image by SEM, (b) 3D scan of “SSM-80” stamp by the grinding wheel scanner.

Figure 6.12 shows the horizontal measurements. It should be noted that, in the case of the 3D measurements, the edges of the measured features were slightly rounded making it difficult to accurately establish the position of the features. The intersection between these edges and a constant reference plane placed below the surface being measured was, therefore, used to help remove any ambiguity in the positions of the features.

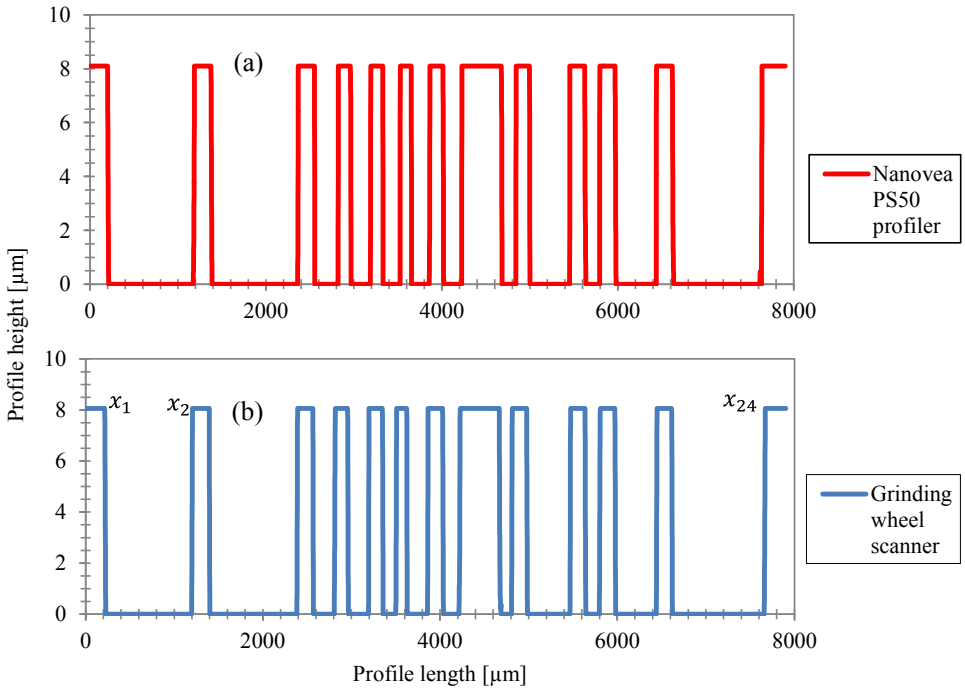

Figure 6.12 The 2D profile in x direction by (a) the grinding wheel scanner and (b) Nanovea PS50 profiler.

Table 6.1 and Table 6.2 show the resulting measurements and analyses for the horizontal and vertical directions. To analyze the results, the mean measurement values were calculated as well as the difference between the mean measurements and the actual measurements. The Root Mean Square (RMS) values of the measurement differences were then used to compare the proposed grinding wheel scanning system with the SEM and the Nanovea PS50 profiler. The RMS values for n positions of x is calculated using Equation (6.4). The RMS values for the vertical direction were 6.7, 8.9 and 8.5 µm and the RMS values for the horizontal direction were 4.9, 5.8 and 5.4 µm for the grinding wheel scanner, Nanovea PS50 profiler and SEM, respectively. These test results demonstrate that the performance of the proposed grinding wheel scanner is comparable to both the Nanovea PS50 profiler and the SEM for measuring features of this size.

$$x_{RMS} = \frac{\sqrt{\sum_{i=1}^{n} {x_i}^2}}{n} \tag{6.4}$$

Table 6.1 2D profile measurement for number 24 in *x*-direction using three different methods.

Points in horizontal direction	Resulting measurements			Mean $[\mu m]$	Differences from the mean		
	Grinding wheel scanner $[\mu m]$	Nanovea PS50 profiler $[\mu m]$	Scanning electronic microscope $[\mu m]$		Diff. Grinding wheel scanner $[\mu m]$	Diff. Nanovea PS50 profiler $[\mu m]$	Diff. Scanning electronic microscope $[\mu m]$
x_1	221	205	221	215.7	−9	14	−4
x_2	1203	1185	1245	1210.9	4	13	−18
x_3	1398	1381	1388	1388.9	8	5	−13
x_4	2390	2366	2385	2380.3	9	10	−19
x_5	2567	2554	2531	2550.6	6	5	−12
x_6	2813	2823	2793	2809.7	−3	3	0
x_7	2961	2966	2918	2948.4	6	−1	−5
x_8	3197	3191	3154	3180.8	2	0	−1
x_9	3355	3330	3279	3321.4	5	5	−10
x_{10}	3508	3527	3471	3502	−6	2	4
x_{11}	3627	3654	3572	3617.8	5	−4	−1
x_{12}	3863	3862	3806	3843.6	−6	4	1
x_{13}	4033	4017	3938	3995.9	0	−1	0
x_{14}	4224	4227	4157	4202.7	0	−2	2
x_{15}	4672	4681	4570	4640.9	3	−3	−1
x_{16}	4812	4843	4747	4800.8	−1	−3	5
x_{17}	4980	4998	4879	4952.4	1	−4	2
x_{18}	5471	5455	5363	5429.6	−8	12	−4
x_{19}	5640	5626	5497	5587.8	1	−3	2
x_{20}	5804	5795	5695	5764.5	−3	−2	4
x_{21}	5978	5974	5831	5927.6	0	−1	1
x_{22}	6445	6439	6325	6403.1	−3	1	3
x_{23}	6619	6624	6445	6562.5	−6	−3	9
x_{24}	7667	7637	7519	7606.9	−2	3	−2
RMS					4.9	5.8	7.4

Table 6.2 2D profile measurement for number 8 in *y*-direction using three different methods.

Points in vertical direction	Resulting measurements			Mean $[\mu m]$	Differences from the mean		
	Grinding wheel scanner $[\mu m]$	Nanovea PS50 profiler $[\mu m]$	Scanning electronic microscope $[\mu m]$		Diff. Grinding wheel scanner $[\mu m]$	Diff. Nanovea PS50 profiler $[\mu m]$	Diff. Scanning electronic microscope $[\mu m]$
x_1	54	63	72	63	9	0	-9
x_2	467	462	471	467	0	5	-4
x_3	578	575	575	576	-2	1	1
x_4	973	966	971	970	-3	4	-1
x_5	1083	1083	1083	1083	0	0	0
x_6	1608	1634	1597	1613	5	-21	16
x_7	1697	1719	1705	1707	10	-12	2
x_8	2112	2102	2085	2100	-12	-2	15
RMS					6.7	8.9	8.5

A repeatability test was also conducted to ensure that the wheel measuring system provides the same results for the same profile using different scanning parameters such as scan speed, scan sampling rate, scan averaging operation, and scan working distance. A new test surface was prepared by scribing 18 fine scratches on a cylindrical surface as shown in Figure 6.13 (a). The scratches had a depth of 5 µm and were spaced 0.25 mm apart (except for the first two scratches which were spaced 0.5 mm apart). Two additional scratches were made which were perpendicular to the other 18 scratches and spaced 0.5 mm apart. Figure 6.13 (b) shows a 3D scanned surface of the scratches measured using the grinding wheel scanner.

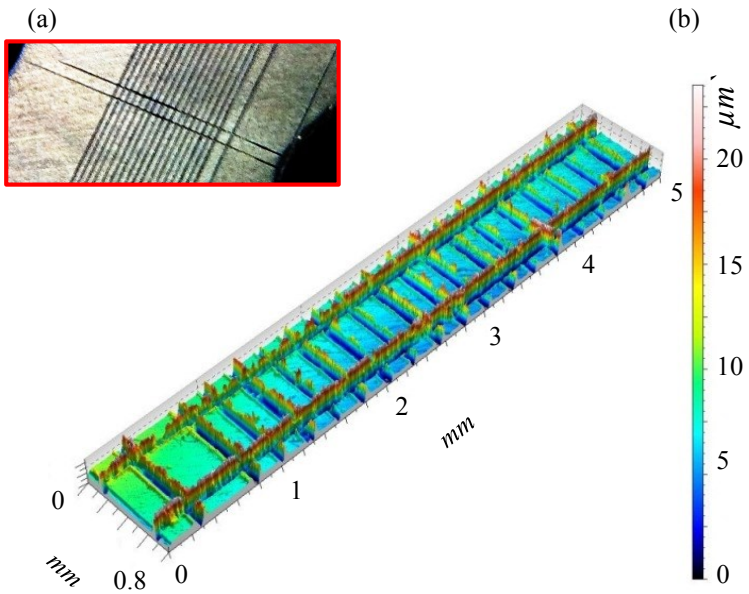

Figure 6.13 (a) The test part with fine scratches, and (b) 3D scanned surface of the fine scratches on the test part.

Figure 6.14 plots three profiles of the scratches while keeping the vertical stage at the same location. The wheel peripheral speed was set to $1.0\,mm/sec$, $0.3\,mm/sec$ and $0.1\,mm/sec$ while the sampling rate of the measuring pen was set as $1000\,Hz$, $300\,Hz$ and $100\,Hz$, respectively, in order to maintain a constant sampling interval of $1\,\mu m$. Each profile was measured with different working distances, which is the distance between the optical pen lens and the measured object (see Figure 6.1). The three profiles in Figure 6.14 appear identical not only in profile length but also in profile height – including the subtle details captured in the peak of first scratch and in the valley of the last scratch. Furthermore, the distances between the scratches were measured for each profile and the average standard deviation was only $1.1\,\mu m$ indicating excellent repeatability.

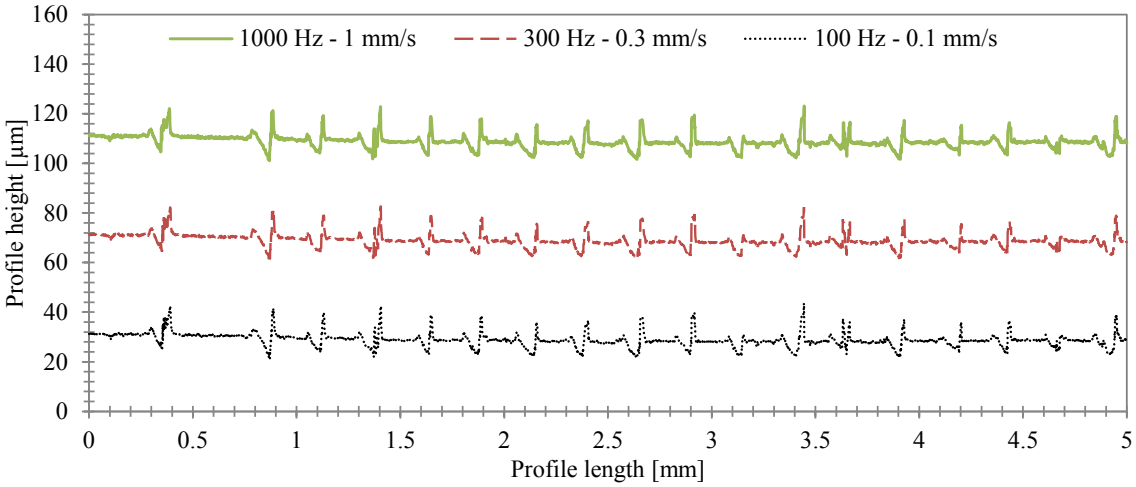

Figure 6.14 Speed test.

6.6 Sampling rate and sample size

The grinding wheel scanning system was then used to determine the surface topography characteristics of a Radiac Abrasives WR-A-60-J5-V1 aluminum oxide grinding wheel. This grinding wheel was dressed with a single-point diamond dressing tool with a dressing depth of $0.02\,mm$ and dressing feeds of 0.04, 0.08 and $0.25\,mm/rev$ which correspond to fine, medium and coarse dressing conditions, respectively. The grinding wheel was subsequently mounted on the wheel scanning system to characterize its topography.

The sampling interval of the measurement process, which is the distance between each successive measured point, can significantly influence the result. Smaller sampling intervals will reveal more detail of the wheel topography but will also increase the time required to complete the measurement process. Blunt [39] proposed that the optimum sampling interval is between one forth to one third of the average grain size. The average grain size d_g can be calculated using the following equation [2]:

$$d_g = 15.2\,M^{-1} \tag{6.5}$$

where M is the grit size. The sampling interval proposed by Blunt [39] ensures a maximum of three measurements of an average-sized grain; however, it does not account for the distribution of the grain size or the fact that one grain may have multiple cutting edges. The optimum sampling interval proposed by Blunt for the 60 grit aluminum oxide wheel to be studied in the present research would be $63\ \mu m$. Yan [48] carried out research using the same grit size used in the present work and noted that, as the sampling interval decreases, the detection of the cutting edges rapidly increases – until the sampling interval reaches $8\ \mu m$ at which point no more cutting edges can be detected. In the present work, a sampling interval of $5\ \mu m$ was used to ensure that all cutting edges were detected. To achieve this sampling interval in the x- and y- directions, the sampling rate of the measuring pen was set to $1000\ Hz$, the grinding wheel peripheral speed (x-direction) was set to $5\ mm/sec$ and the linear actuator (y-direction) intermittently moved the pen by $5\ \mu m$. Using this setup, the measured surface resolution achieved was $40{,}000\ pixels/mm^2$.

Since grinding wheel topography is stochastic, it is also necessary to measure a statistically significant portion of the grinding wheel. In order to determine the minimum patch size needed to be measured, a freshly-dressed grinding wheel was scanned at four locations spaced 90^o around the wheel using different patch sizes. For each patch size, the cutting edge density (which is the number of cutting edge per unit area) was calculated and the standard deviation between the four measurements was determined. As shown in Figure 6.15, the standard deviation of the cutting edge density declines rapidly as the patch size increases from $1\ mm^2$ to $10\ mm^2$ and seems to asymptotically approach a value of approximately $0.6\ \text{cutting edges}/mm^2$. These results suggest that a patch size greater than $10\ mm^2$ should be used for the grinding wheel used in this research. To ensure statistically significant and consistent results, a patch size of $75\ mm^2$ was used in the present work.

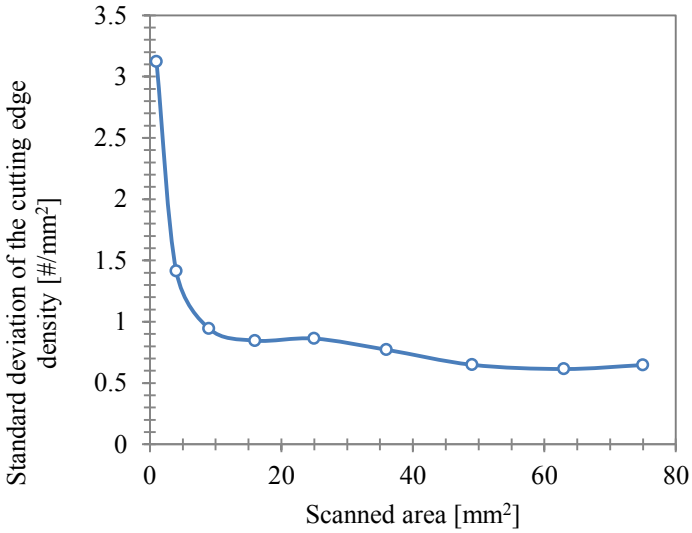

Figure 6.15 Standard deviation of the cutting edge density vs. the scanned area.

6.7 Results

Having established the desired sampling interval, resolution and patch size, the wheel scanning system was used to measure the surface topography of the Radiac Abrasives WR-A-60-J5-V1 aluminum oxide grinding wheel after fine, medium and coarse dressing conditions in order to better quantify the effects of dressing on the grinding wheel surface topography as well as to aid in the development of accurate grinding wheel computer models. The experiments were carried out on a Blohm Planomat 408 CNC grinding machine.

Figure 6.16 shows the grinding wheel topography of a 4×4 mm patch of the grinding wheel for dressing feeds of $0.04\,mm/rev$ (fine dressing), $0.08\,mm/rev$ (medium dressing) and $0.25\,mm/rev$ (coarse dressing). The white color in the plotted topography indicates the exposed cutting edges. It appears from these images that, as the dressing feed increases, the size and number of cutting edges decreases. In order to quantify the differences between these surfaces, novel methods were developed in this research to extract cutting edge density, size, protrusion height and spacing information from these measurements.

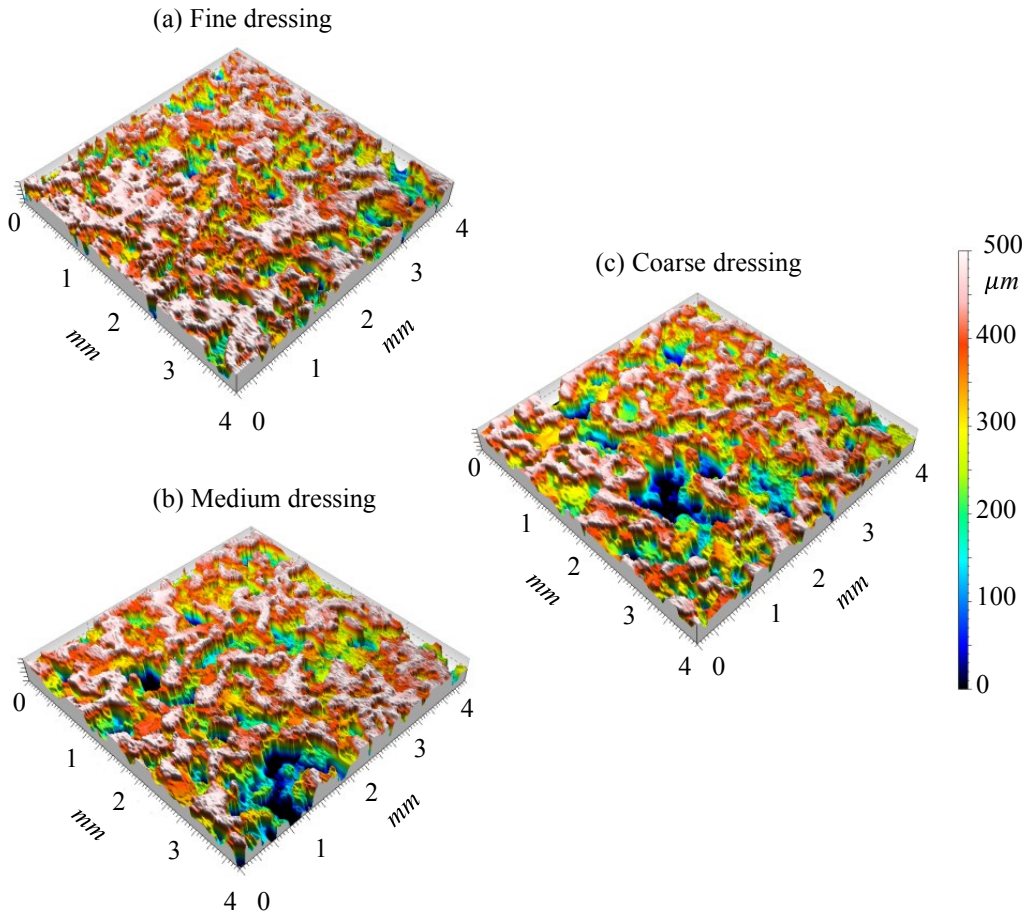

Figure 6.16 3D Grinding wheel topography in (a) find dressing, (b) medium dressing and (c) coarse dressing.

While other researchers have employed various methods to detect the cutting edges on a grinding wheel including visual inspection [40], eight nearest neighbor detection [39], autocorrelation detection [40], corner detection [49] and closed boundary [46]. Figure 6.17 illustrates the novel cutting edge detection method used in this work. In the illustration, a threshold plane cuts through a grain at different threshold depths. The areas of intersection between the grain and the threshold plane are colored black and are referred to as particles. It is evident from this illustration that the threshold depth will influence both the size and distribution of the cutting edges. Each threshold plane was analyzed in LabView's ImageStudio image processing software using a technique called

particle analysis – commonly referred to as "blob" analysis. A simple definition of a blob is a group of contiguous connected pixels that have the same intensity (height in this case) and are surrounded by pixels with different intensity (height values). In order to use blob analysis, the threshold plane was converted into a binary image. Then, the imaging processing software operated on the binary image to count and measure the blobs (cutting edges).

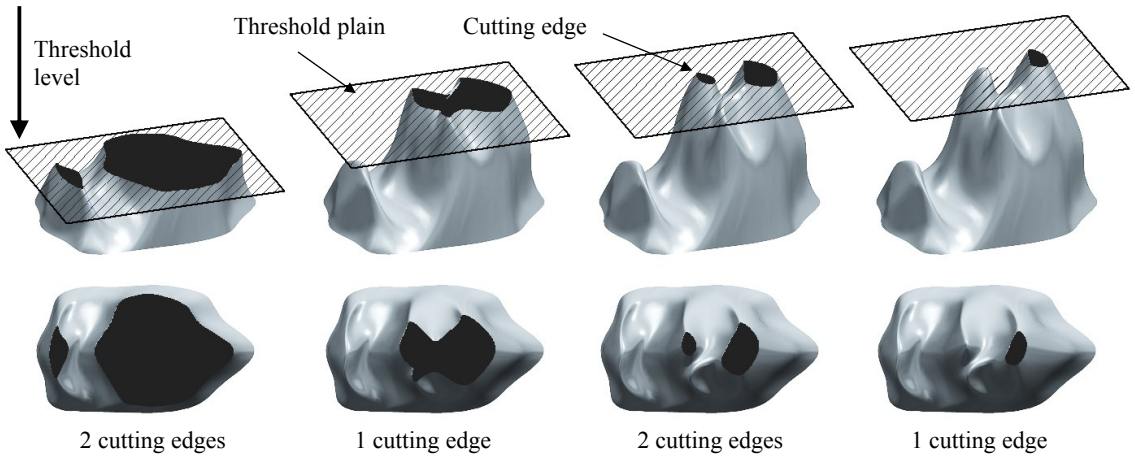

Figure 6.17 Cutting edge detection.

An example of the resulting binary images for $5, 30$ and $80\ \mu m$ threshold planes for each dressing condition is shown in Figure 6.18. To provide a sense of scale, a circle with the same diameter as an average grain has been placed in the figure. Some of the blobs in the image are significantly larger than the average grain size and are likely amalgamations of several grains joined by bond material. These images confirm that coarse dressing conditions produce fewer and smaller cutting edges than fine dressing conditions.

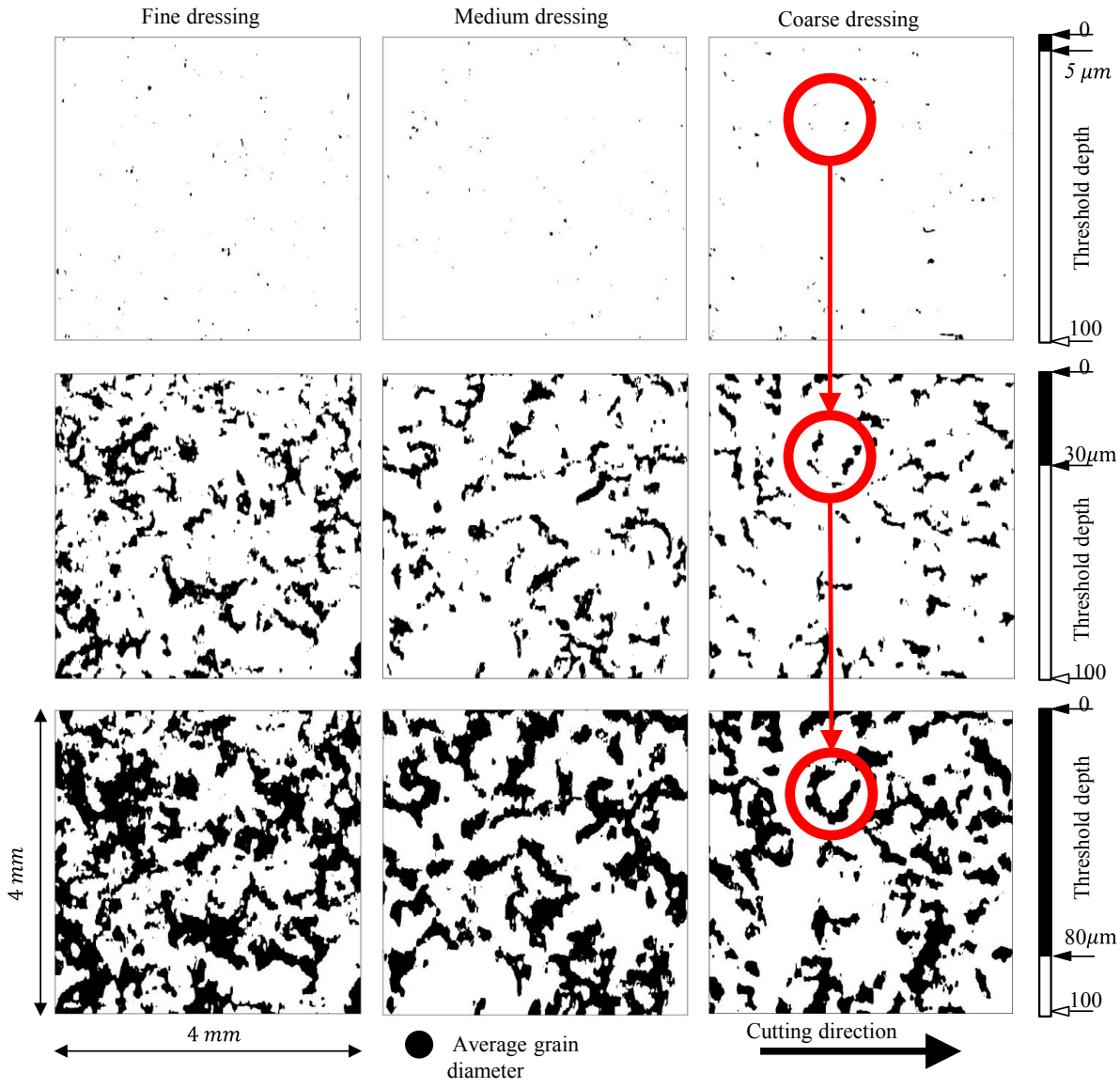

Figure 6.18 The cutting edges at threshold depth of 5, 30 and 80 $m\mu$.

The images also show that, as the threshold depth increases, the number and size of cutting edges increases. For instance, in Figure 6.18 (coarse dressing) there are only a few small cutting edges exposed in the circle at a threshold depth of 5 μm. Then, at a threshold depth of 30 μm, new cutting edges are exposed in the circle while others grow and/or join together. Finally, at threshold depths beyond 80 μm, all cutting edges become compounded into one large cutting edge. To quantify these relationships, the average

cutting edge density and the average cutting edge were plotted as a function of threshold depth as shown in Figure 6.19, and Figure 6.20.

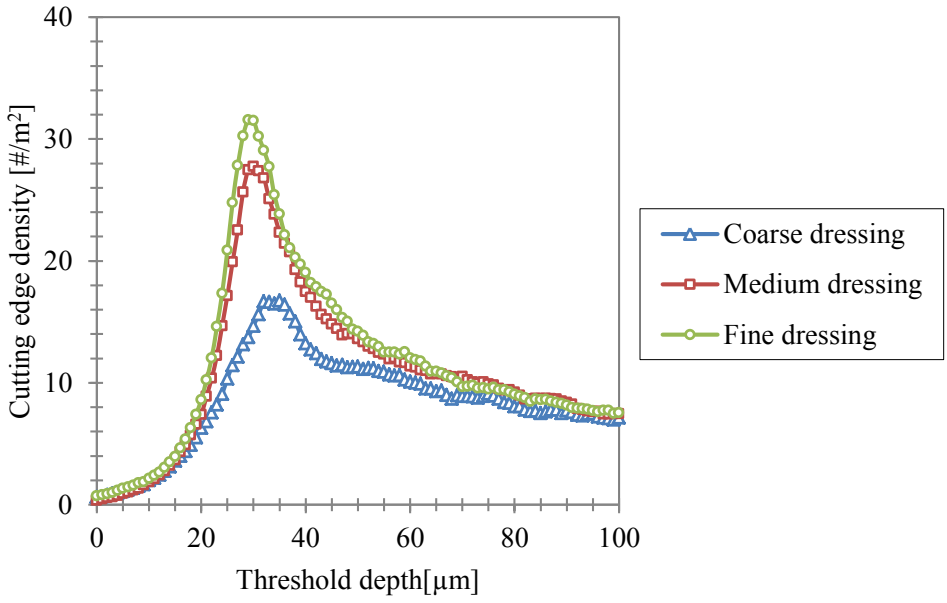

Figure 6.19 Cutting edge density vs. threshold depth.

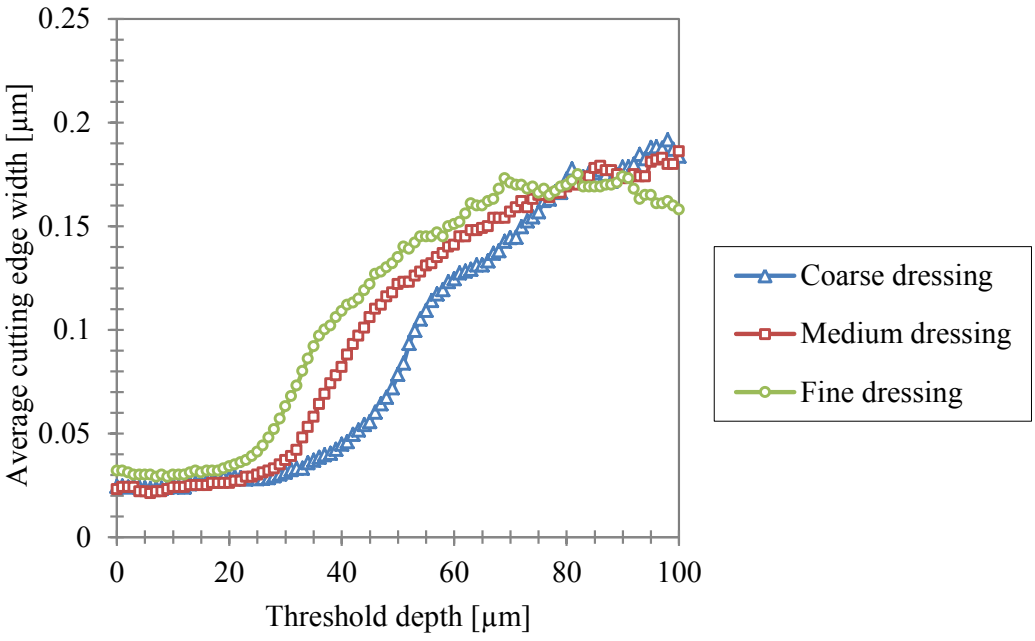

Figure 6.20 Average of cutting edge width vs. threshold depth.

It can be seen in this figure that, as the threshold depth increases, the cutting edge density rapidly increases up to a maximum and then slowly decreases. The maximum cutting edge density for fine dressing is about twice that observed for coarse dressing and occurs at a slightly shallower threshold depth ($29\ \mu m$ versus $34\ \mu m$). At threshold depths beyond $80\ \mu m$ the cutting edge densities for all dressing conditions seem to converge to the same value. Unlike the cutting edge density, the average cutting edge width curves do not exhibit a peak as the threshold depth increases. Rather, the average size of the cutting edges increases continuously with threshold depth for all dressing conditions – with the cutting edges produced by fine dressing being larger than the cutting edges produced by coarse dressing. For example, at a threshold depth of $40\ \mu m$ the average cutting edge width is 0.11 and $0.04\ mm$ for the fine and coarse dressing conditions, respectively. The average cutting edge width also appears to converge to a value of approximately 200 μm at a threshold depth of $80\ \mu m$ which is close to the estimated average grain size of 253 μm.

Blob analysis can also be used to determine the protrusion height distribution of the cutting edges by employing an upper and lower threshold. A cutting edge peak occurs, for example, when a cutting edge protrudes past the lower threshold but does not protrude past the upper threshold. For this analysis, the upper and lower thresholds were spaced $4\ \mu m$ apart. Figure 6.21 plots the corresponding cutting edge protrusion height histogram. Researchers are somewhat divided on whether the cutting edge protrusion height is a normal distribution or a uniform distribution [13]. It is evident from the histogram in Figure 6.21, however, that a normal distribution would be more appropriate than a uniform distribution for the grinding wheel and dressing conditions used in this research. From this figure it is also evident that the peak number of cutting edges occurs at about the same depth regardless of the dressing condition, while the coarse dressing condition results in a wider distribution of cutting edges than the medium and fine dressing conditions.

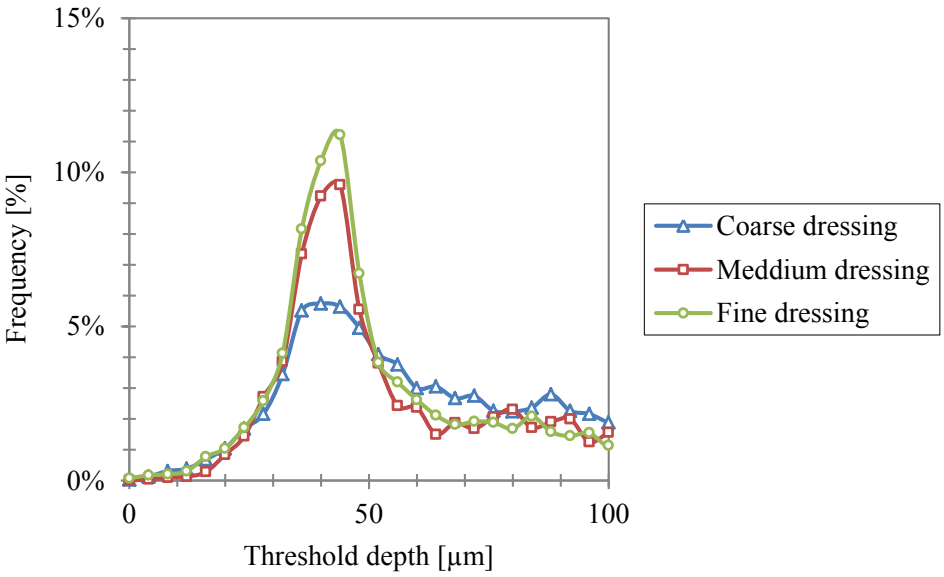

Figure 6.21 Cutting edge protrusion height histogram.

The average cutting edge spacing as a function of threshold depth was determined by measuring the distance between the blobs in the direction of cutting (*x*-axis). Figure 6.22 plots the average cutting edge spacing versus the threshold depth for the fine, medium and coarse dressing conditions. From this figure it can be seen that the average cutting edge spacing decreases exponentially as the threshold depths increases and that the average spacing between cutting edges for the coarse dressing condition is always larger than for the medium and fine dressing conditions.

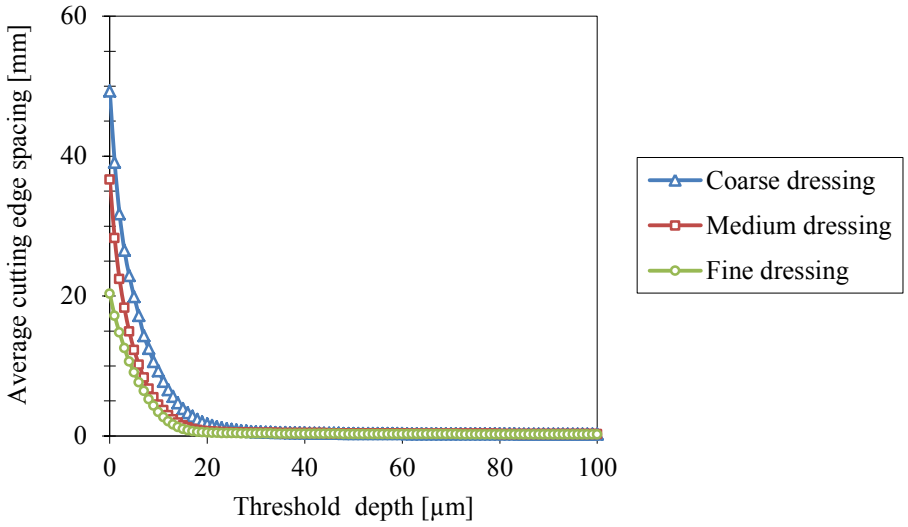

Figure 6.22 Average cutting edge spacing vs. threshold depth.

Given a cutting edge density and cutting edge spacing as a function of threshold depth, it is possible to define the uncut chip thickness h_m as a function of threshold depth using the following equation [2]:

$$h_m = \left(\frac{2}{C\,\bar{b}_c}\right)\left(\frac{v_w}{v_s}\sqrt{\frac{a}{d_s}}\right) \tag{6.6}$$

where C is the cutting edge density, $\bar{b}_c$ is the average cutting edge width, v_w is the workpiece speed, v_s is the cutting speed, d_s is the grinding wheel diameter and a is the grinding depth of cut. An approximation method was reviewed in Chapter 2 (Equation (2.12) and Equation (2.13)) to determine the cutting edge density and the average of the cutting edge width [2]. Although, this method provides a quick estimation of the cutting edge density and width, it assumes one cutting edge per grain.

Figure 6.23 plots the uncut chip thickness versus threshold depth. The grinding wheel diameter was 355 mm. The workpiece speed, the cutting speed and the grinding depth of

cut were assumed to be $0.03\ mm/sec$, $20\ mm/sec$ and $0.03\ mm$, respectively. The maximum uncut chip thickness was found at a small threshold depth because, at a small threshold depth, there are small and few cutting edges. As the threshold depth increases, more and cutting edges are found causing in small uncut chip thickness.

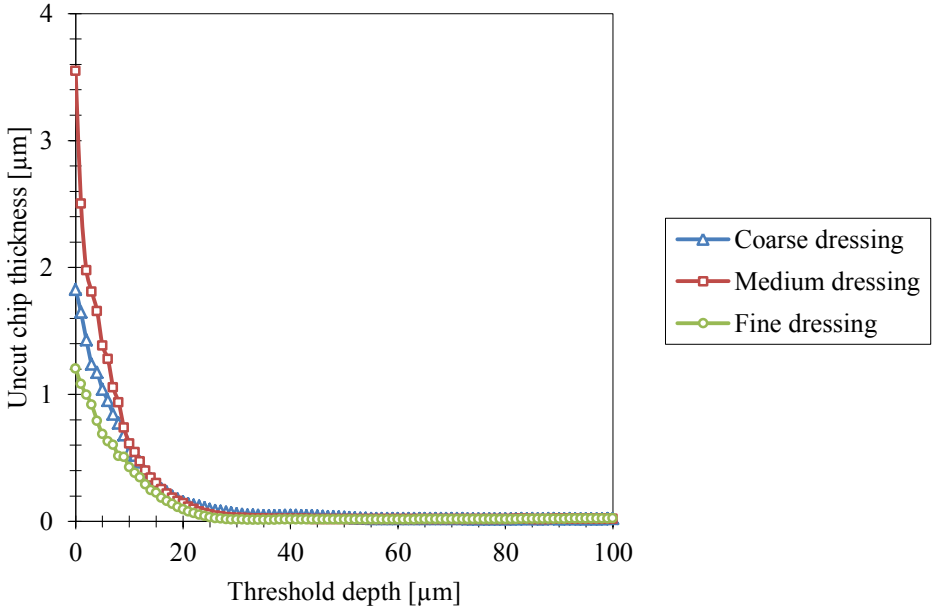

Figure 6.23 Uncut chip thickness vs. threshold depth.

It is also possible to extract the distributions of cutting edge spacing and cutting edge width for a particular threshold depth. For example the cutting edge spacing and width distributions for a depth of $8\ \mu m$ are shown in Figure 6.24 and Figure 6.25. Both the cutting edge spacing and width distributions are roughly exponential in shape and there is little variation in the distributions for different dressing parameters at this depth.

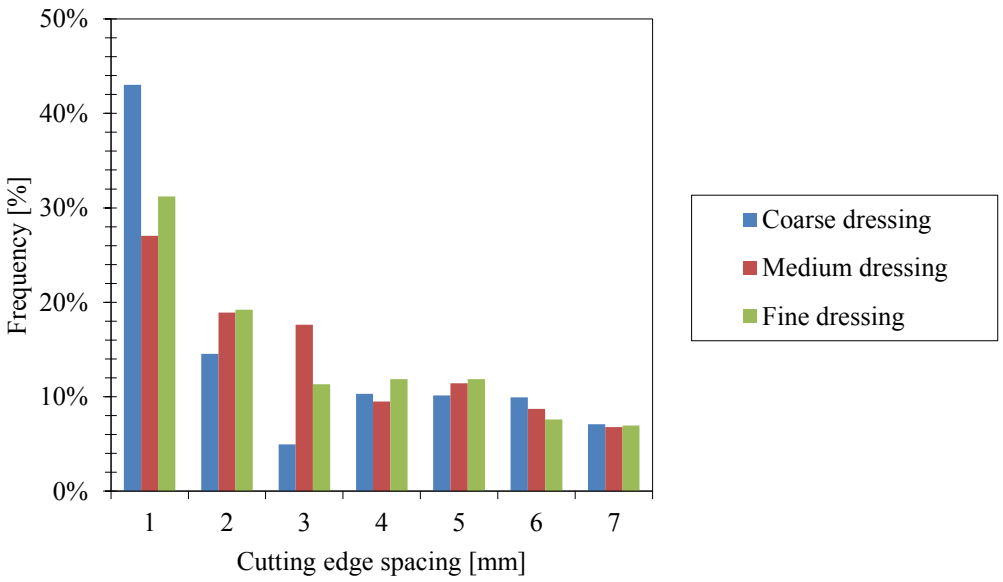

Figure 6.24 Cutting edge spacing histogram for a threshold depth of 8 μm.

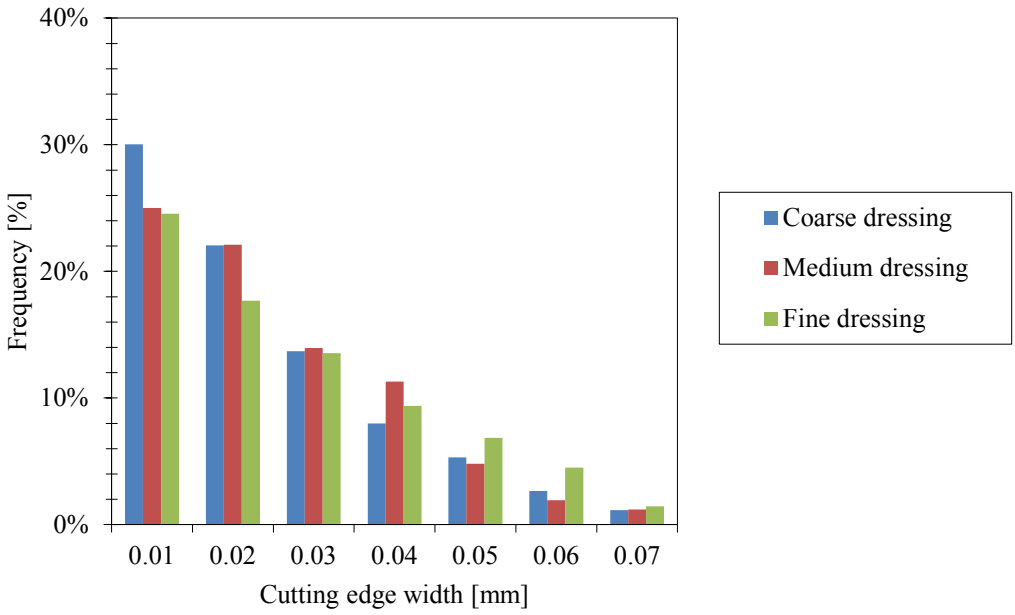

Figure 6.25 Cutting edge width histogram for a threshold depth of 8 μm.

6.8 Analysis

The preceding observations can be best explained using the three primary dressing actions: grain pull out, grain fracture, and ductile cutting. According to Chen and Rowe [11], when dressing a grinding wheel, the bond material that holds the grains together attempts to resist the dressing force (which tries to dislodge the grains from the grinding wheel surface). If the dressing force is high enough, the entire grain could be dislodged from the wheel surface or grain fracture may occur where a large fragment of the grain is removed. A small dressing force may, on the other hand, not be high enough for grain fracture to occur and, instead, cause ductile cutting of the grain or bond material. The degree of interaction between the dresser and the wheel can be quantified by considering the intersection area between the dressing tool and the grain as illustrated in Figure 6.26. For this work the maximum intersection area for fine, medium and coarse dressing was 0.001, 0.002 and $0.004\ mm^2$, respectively. Since the maximum intersection area was highest for coarse dressing, one would expect to see more grain pull out and larger grain fractures when compared with medium and fine dressing conditions resulting in fewer and smaller cutting edges (as observed in the data). Possible examples of grain pull out have been identified as dark blue and black holes in Figure 6.16 (c, b). The effect of grain fracture and grain pull out can also help explain the observed convergence of the cutting edge density, width, protrusion height, and spacing curves for different dressing conditions as threshold depth increases. In particular, as the threshold depth increases, the number of detected fractures and grains pulled out decreases and no longer affects the surface topography. Referring to Figure 6.19, Figure 6.20 and Figure 6.21, dressing noticeably affected the grinding wheel surface geometry up to a threshold depth of $80\ \mu m$.

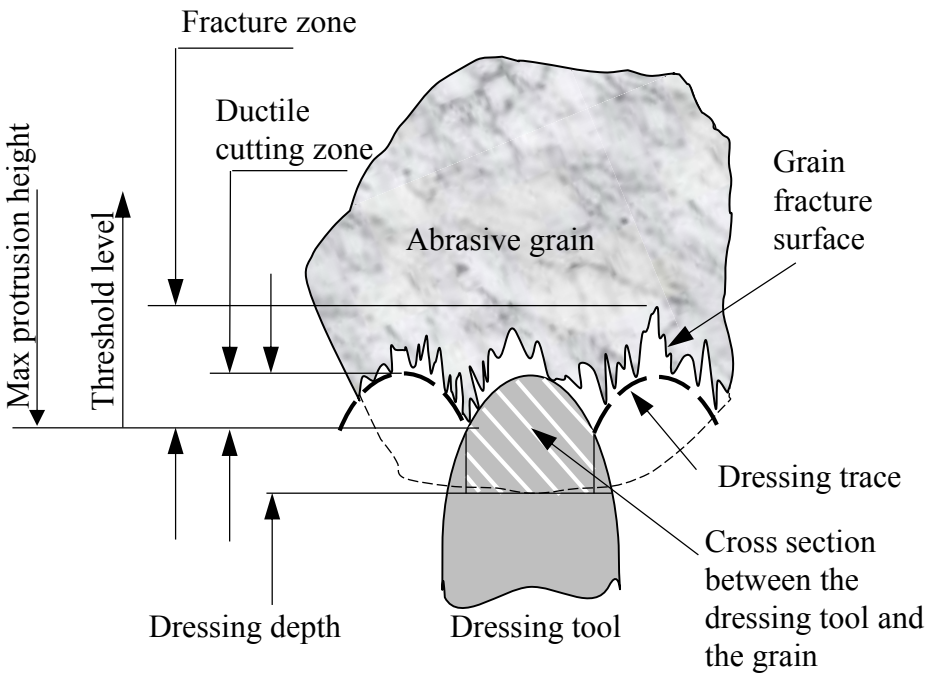

Figure 6.26 Illustration of grain fracture by single-point dressing tool.

There is also some evidence in the results of ductile cutting during dressing. Referring to Figure 6.26, the ductile cutting zone is the distance between bottom dead center on the dressing tool and the maximum cusp height on the grain fracture surface which, in the present case, is 20, 2.4 and 0.8 μm for coarse, medium and fine dressing, respectively. If pure ductile cutting was occurring it would appear as valleys between parallel ridges on the grinding wheel surface. It would be expected that the resulting spacing of these ridges and valleys to be 41.7, 83.3 and 250 μm for fine, medium and coarse dressing, respectively, which corresponds to the dressing feed per revolution. Although the measurements did not identify any pattern of ridge-type features (perhaps because these thin features would be easily fractured), rather than exhibiting a jagged surface the abrasive grains appeared to have relatively flat tops – especially with the fine dressing condition (see Figure 6.16) which is indicative of ductile cutting as suggested by Malkin and Murray [66].

The depth at which dressing induced grain fracture effects can be observed has been called the fracture zone, as illustrated in Figure 6.26. The number and size of fractures is likely proportional to the interaction area. Fractures can act to divide a single abrasive grain into multiple smaller cutting edges or they can remove large chunks of a grain effectively reducing the number and size of cutting edges. Evidence for the first type of fracture can be observed in Figure 6.18 where many small particles have a spacing of less than an average grain diameter. Likely a combination of both types of fractures is occurring. Since course dressing produces a smaller number of small cutting edges it is likely that the second type of fracture is more common. The effect of grain fracture and grain pull out can also explain the convergence of both the cutting edge density curves and the average cutting edge width curves as depth increases. As the depth increases, the number of fractures and grains pulled out decreases no longer affecting the surface topology.

6.9 Summary

In this chapter, a new grinding wheel scanning system capable of measuring the entire surface of an industrial-sized grinding wheel with a planer resolution of $1\ \mu m$ and a depth resolution of $25\ nm$ was developed using a white light chromatic sensor. This system was compared to measurements using a HITACHI S-4700 Scanning Electronic Microscope and a Nanovea PS50 profiler and was found to have comparable accuracy when measuring features with approximately the same abrasive grit size as a 60 grit aluminum oxide grinding wheel. Subsequently, novel methods for conditioning the resulting measurements and extracting cutting edge density, size, protrusion height, and spacing were presented based on the concepts of image segmentation and "blob" analysis. Also, the histogram of cutting edge width and spacing at a particular threshold depth were extracted. The result obtained in the present chapter will be used to develop a dressing model for grinding wheel.

CHAPTER 7. SIMULATION OF METAL REMOVAL WITH A DRESSED WHEEL MODEL

7.1 Introduction

In Chapter 5, a 3D wheel model was used in the metal removal simulation without dressing. In order to compare the simulation results with the experimental results, the grinding wheel was dressed in Chapter 5 by a rotary diamond roll with dressing ratio of 1.1. This value was selected to maximize bond fracture and minimize the grain fracture and ductile cutting of the dressing tool with the intent to minimizing the effect of the dressing process on grain shape and distribution [8, 9]. In the followed chapter, characteristics of dressed grinding wheel topography using different dressing conditions were obtained. It was found that the size of cutting edges exposed in the wheel surface is much smaller than the grain size. In this chapter a new simulation with a dressing model is presented to simulate grinding wheel topography in 3D. The characteristics of the simulated wheel topography will be compared with the experimental results obtained from Chapter 6. Subsequently, the dressed wheel model will be used by the 3D metal

removal model to generate a ground surface of a workpiece and calculate the uncut chip thickness and contact length.

7.2 Mechanics of dressing process

Many procedures have been developed to dress grinding wheels. This work will focus on single-point dressing as illustrated in Figure 7.1. In single-point dressing, a diamond dressing tool travels across the face of the grinding wheel with a cross-feed velocity of v_a and a dressing depth of a_d as the grinding wheel of diameter d_s rotates with a tangential velocity of v_s. This kind of dressing motion is analogous to the turning operation on a lathe.

The axial feed of the dressing tool per wheel revolution is called the dressing lead f_d, which can be calculated by the following equation [2]:

$$f_d = \frac{\pi\, d_s\, v_d}{v_s} \tag{7.1}$$

The overlap ratio U_d is the ratio of the active width b_d of the single-point diamond tip to the dressing lead f_d and can be expressed by the following equation [6]:

$$U_d = \frac{b_d}{f_d} \tag{7.2}$$

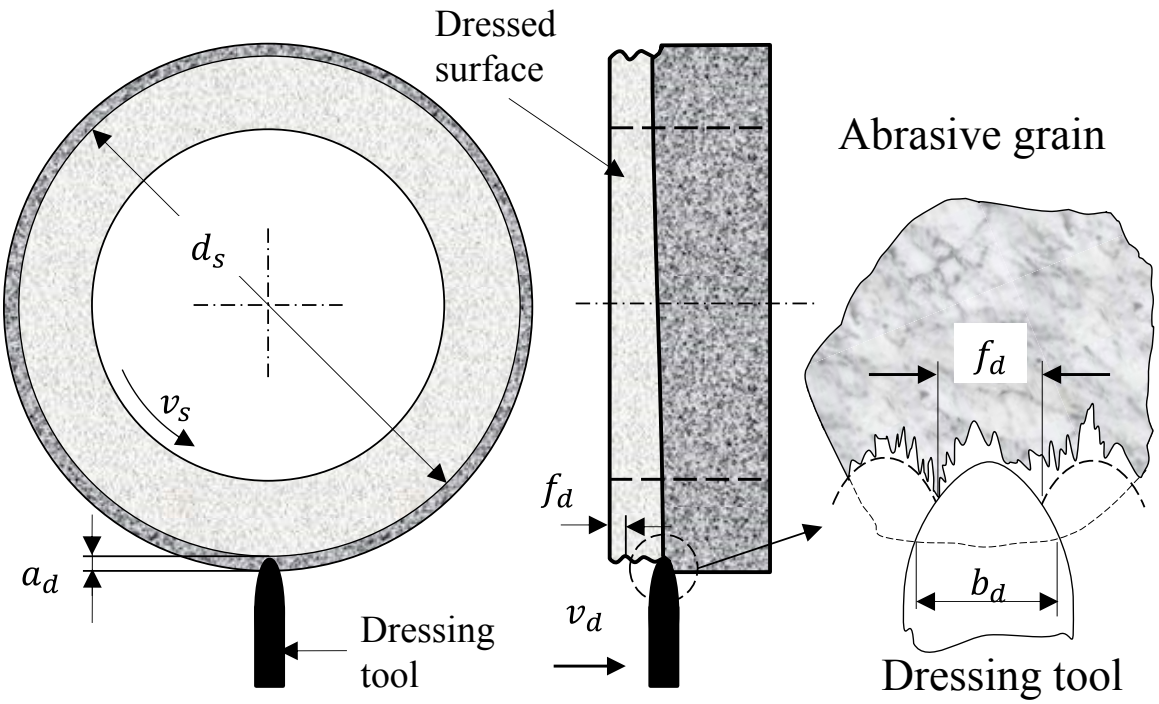

Figure 7.1 Single-point dressing of grinding wheel.

The active width is the width of the dressing tool at the dressing depth of cut. The overlap ratio provides a good indication of the type of dressing operation. A fine dressing operation has an overlap ratio of $6-9$ while course dressing operations have overlap ratios approaching 1. Malkin and Cook [67] examined the particles of the fractured abrasive grains which were produced by a dressing operation and found that the size of the particles is larger than the dressing depth but is smaller than the original size of the abrasive grains. Malkin and Cook [67] concluded that the dressing process produces a large fragment of the abrasive grains or dislodges the whole abrasive from the grinding wheel surface and that the abrasive material is mostly removed by brittle fracture rather than ductile cutting to a depth greater than the dressing depth. The dislodgement of abrasive grains from the grinding wheel surface is caused by the fracture of bond material, which is used to hold the abrasive grains in the grinding wheel. Pande and Lal [68] assumed that, as the dressing depth increases or the dressing lead decreases, the bond

fracture increases. As the dressing process continues, wear in the dressing tool occurs and its tip radius becomes blunter. This wear will result in a rapid increase of the dressing force which causes more chance of bond fracture and more abrasive grains to be dislodged from the grinding wheel surface.

7.3 Extraction of grinding wheel surface from the 3D model

The proposed dressing model is intended to be applied to the 3D stochastic grinding wheel model that was presented in Chapter 5. Since the 3D stochastic grinding wheel model was provided in a form of a list of grain size and location (d_g, x_c, y_c, z_c), the grinding wheel surface was extracted from the 3D model in order to be compared with the measured grinding wheel surface. The extraction process was accomplished in the following manner: first the wheel model was sectioned by a cutting plane parallel to the xy plane with different values of z to generate 2D-slice models as shown in Figure 7.2 (a). For each 2D-slice, the exposed grains from the surface must satisfy the following condition:

$$R_g + \frac{d_g}{2} > H \tag{7.3}$$

where H is the minimum surface height, and R_g is the distance between the grain center (x_c, y_c) and the wheel center $(0,0)$ and can be calculated by the following equation.

$$R_g = \sqrt{{x_c}^2 + {y_c}^2} \tag{7.4}$$

The profile of the outmost surface is generated by the following equations.

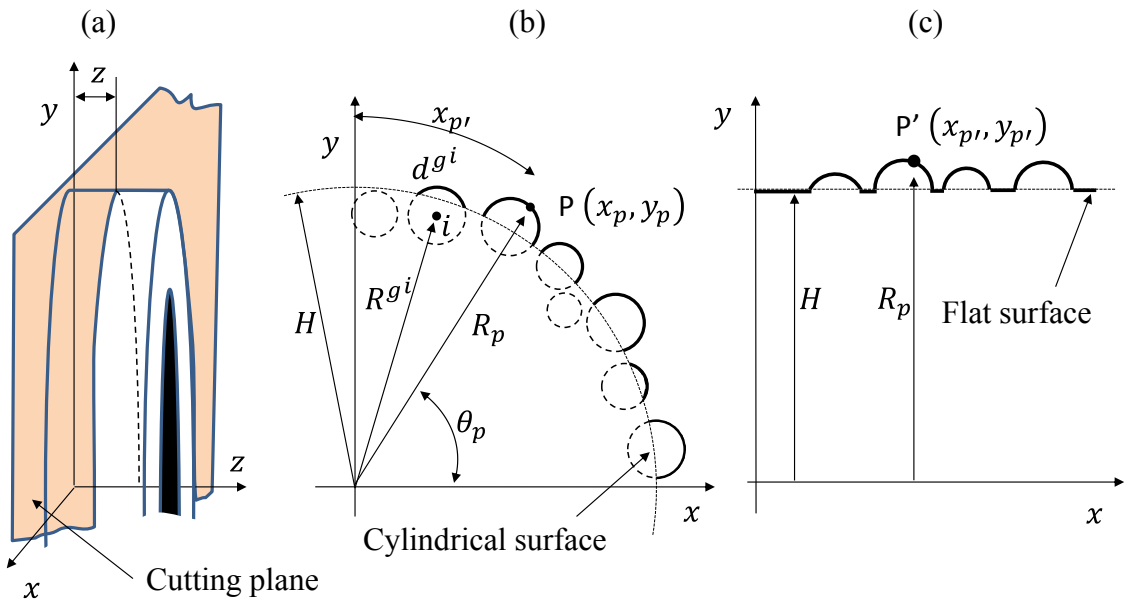

Figure 7.2 Converting from cylindrical surface to flat surface.

$$y = \max\left(\sqrt{H^2 - x^2} \quad , \quad {y_c}^i + \sqrt{\left({R_g}^i\right)^2 - (x - {x_c}^i)^2}\right) \tag{7.5}$$

where i is the exposed grain number. If the distance between the x value and the value of the x-component of the grain center ${x_c}^i$ is greater than the grain radius ${R_g}^i$, the term $\left\{{y_c}^i + \sqrt{\left({R_g}^i\right)^2 - (x - {x_c}^i)^2}\right\}$ will have a complex number. In such a case y in Equation (7.5) takes the value of $\sqrt{H^2 - x^2}$. The 2D profile will have a circular shape, thus, the final step is set to convert the circular profile into a straight profile, as shown in Figure 7.2 (c). This step will result in a protrusion height versus arc length graph. In Figure 7.2 (b) point P (x_p, y_p) has a polar coordinate of (R_p, θ_p). To generate a 3D flat wheel surface this point is converted into point P′$(x_{p'}, y_{p'})$ using the following equations:

$$x_{p'} = R_p \times \theta_p = \left(\sqrt{{x_p}^2 + {y_p}^2}\right) \tan^{-1}\left(\frac{x_p}{y_p}\right) \tag{7.6}$$

$$y_{p'} = R_p \tag{7.7}$$

The z component of all points in each cutting plane is the distance between the cutting plane and $x - y$ plane. Figure 7.3 shows an example of a $2\,mm$ by $2\,mm$ patch of the converted surface of the grinding wheel in 3D before the dressing operation.

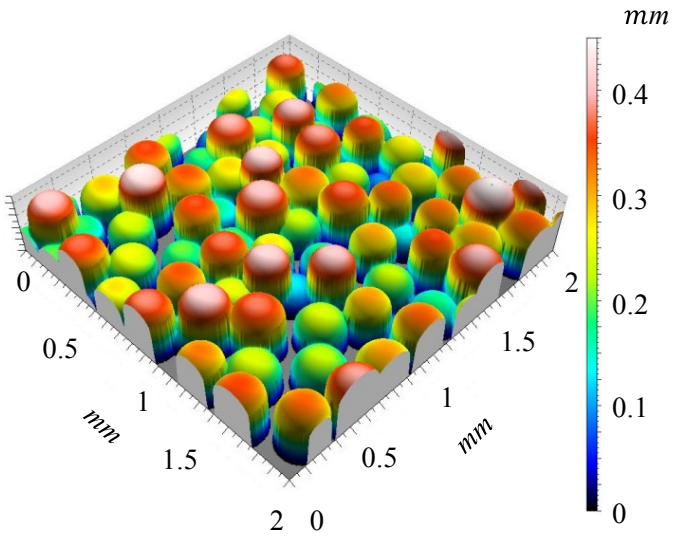

Figure 7.3 the grinding wheel model before dressing.

7.4 Review of dressing models

The models of Torrance and Badger [62] and of Chen and Rowe [11] were the only two dressing models found in the literature that can be used to dress a 3D grinding wheel model. In the Torrance and Badger [62] model uniform spherical grains are stochastically distributed in the bond material. Then grain and bond fracture on the wheel surface is represented by a series of angled line segments whose slopes are stochastically distributed between a maximum and minimum value.

In the Chen and Rowe [11] model, ductile cutting and grain fracture are considered separately. The resulting dressing trace and the fracture wave are then removed from each abrasive grain on the surface of the grinding wheel model as shown in Figure 7.4. This

model was developed for a 2D grinding wheel model. It can, however, be adapted to a 3D grinding wheel model by applying it across the width of a grain and ignoring the length.

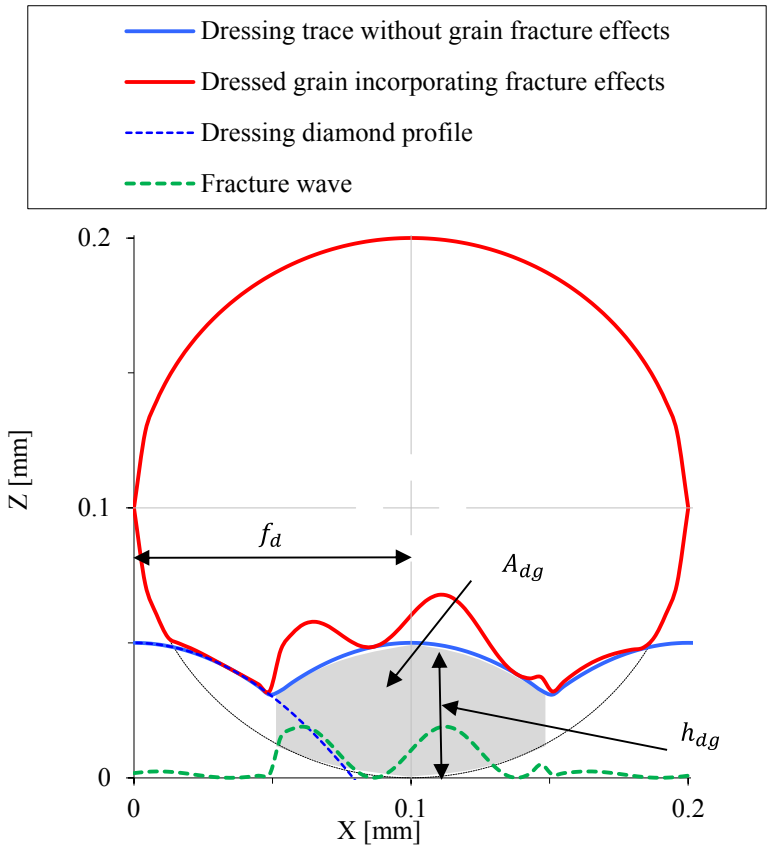

Figure 7.4 The dressing simulation by Chen and Rowe [11].

The dressing tool profile $z_d(x)$ used by Chen and Rowe [11] was approximated by a parabola defined by the height d_h and the width d_w using the following equation:

$$z_d(x) = 4\frac{d_h}{{d_w}^2}x^2 + a_d \tag{7.8}$$

Given a dressing tool model, the dressing tool trace $z_t(x)$ was defined by the following equation [11]:

$$z_t(x) = a_d - z_d\left(x - f_d\, int\left(\frac{x}{f_d}\right)\right) \tag{7.9}$$

where x is the position across the grinding wheel face. The function $int(x/f_d)$ is used to convert the number between brackets into an integer value. The fracture wave was used to account for the effects of grain fracture as shown in Figure 7.4 and defined by Equation (7.10) [11].

$$z(x) = z_t(x) + h(sin(\omega\, x + \alpha) + 1) \tag{7.10}$$

The fracture wave consists of a sine wave function with random frequency ω and random phase angle α. The random frequency ω is calculating by the following equation [11]:

$$\omega = \frac{4\pi\,(1 + \partial)}{f_d + d_w} \tag{7.11}$$

where ∂ is a random value ranging from 0-1. The amplitude of the sine wave h represents the extent of the grain fracture and was expressed as [11]:

$$h = k\frac{A_{dg}\, U_d}{f_d} \tag{7.12}$$

where k is a constant, which was found to be 0.25, and A_{dg} is the intersection area of the tool with the grain as shown in Figure 7.4.

7.5 The proposed model

The proposed model is based on the concept of a ductile cutting trace and a fracture wave as originally proposed by Chen and Rowe [11]. In the proposed model the kinematics of the ductile cutting and the shape of the dressing tool have been modified. Dressing tools are typically made by sintering a natural diamond onto a metal tool holder and typically do not have a symmetrical parabolic shape. Furthermore, as the dressing process

continues, wear causes the dressing tool to change shape. Thus, in the proposed model, it was decided to measure the dressing tool profile using a Nanovea PS50 profiler as shown in Figure 7.5. Subsequently, a 6th order polynomial (see Equation (7.13)) was used to define the best fit to the measured dressing tool profile:

$$z_d(x) = 2.74x^6 + 0.03x^5 - 2.71x^4 + 0.02x^3 - 1.7x^2 \tag{7.13}$$

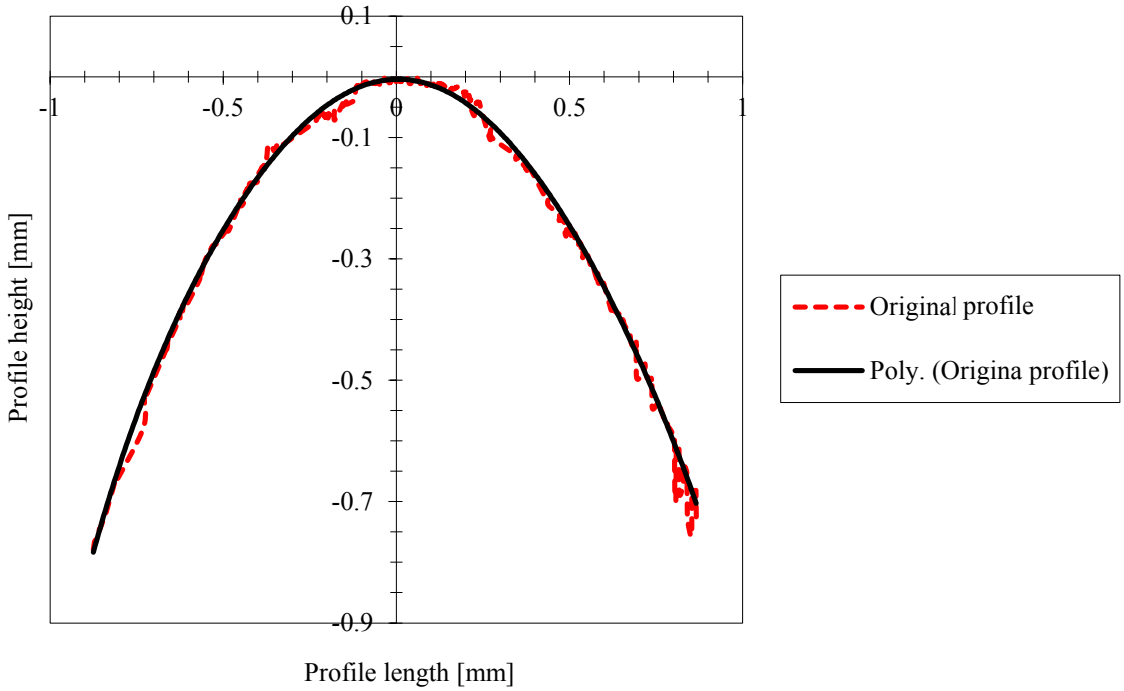

Figure 7.5 Dressing tool profile.

The dressing motion in grinding is analogous to the turning operation on a lathe. The dressing tool travels helically around the grinding wheel working surface. The pitch of the helical path of the dressing tool equals the dressing lead f_d. Equation (7.9) does not provide a helical path. Instead, it provides ring paths around the wheel working surface.

Equation (7.14) and Equation (7.15), therefore, provide a helical path for the dressing tool.

$$z_t(x') = a_d - z_d\left(x' - f_d\, int\left(\frac{x'}{f_d}\right)\right) \tag{7.14}$$

where

$$x' = x + f_d\left(\frac{\beta}{2\pi}\right) \tag{7.15}$$

and β is the grain angle.

The polynomial equation was also used to define the relationship between the dressing depth a_d and the dressing active width b_d as shown in Figure 7.6. The dressing tool active width was used to define the overlap ratio as expressed in Equation (7.2).

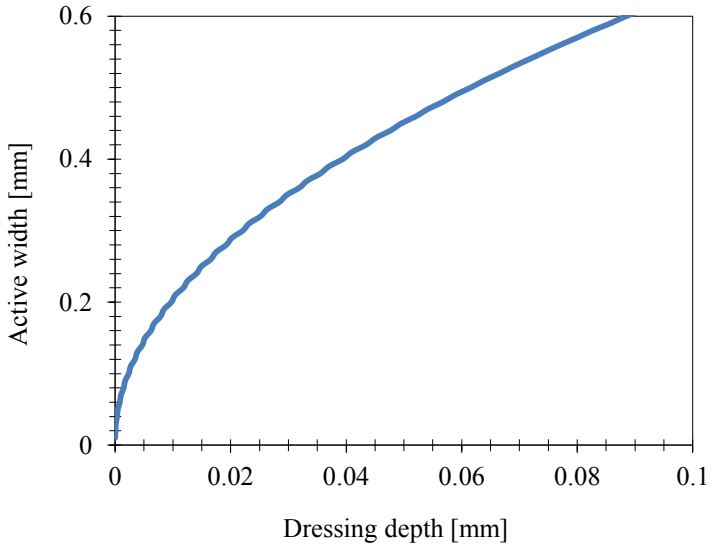

Figure 7.6 Dressing depth vs. Dressing tool active width.

In the proposed model, the methods used to calculate both the amplitude and the frequency of the fracture wave proposed by Chen and Rowe [11] have been modified. As can be seen in Equation (7.16) and illustrated in Figure 7.4, the amplitude of the fracture

wave h is proportional to the instantaneous depth of cut h_{dg} and inversely proportional to the overlap ratio U_d because it is well known that, as the dressing depth of cut increases and the overlap ratio decreases, the workpiece surface roughness increases – presumably because the grinding wheel surface has also become rougher due to more grain fracture.

$$h = k \frac{{h_{dg}}^{n_1}}{{U_d}^{n_2}} \tag{7.16}$$

In the new model, the fractured wave frequency proposed by Chen and Rowe was modified to increase the fracture frequency as the instantaneous dressing depth h_{dg} decreases as shown in Equation (7.17) and Figure 7.4 since a larger depth of cut will likely remove larger portions from an abrasive grain.

$$\omega = \frac{\pi\,(1+\partial)}{f_d + d_w} \left(\frac{1}{{h_{dg}}^{n_1}} \right) \tag{7.17}$$

Table 7.1 summarizes the changes in Chen and Rowe model equations. The proposed model has three fitted parameters: k, n_1 and n_2. The values of these parameters were selected by comparing characteristics of the simulated surface as well as the simulated ground surface roughness values with experimentally determined values. Values of 6.0, 0.5 and 1.3 for k, n_1 and n_2, respectively, were found to give reasonable simulation results. Figure 7.7 shows the effect of changing the dressing lead on the fracture surface of a single grain. It can be clearly seen that, as the dressing lead gets larger, the number of fractures and the amplitude of the fractures increase. Intuitively this observation makes senses because a larger dressing lead will result in a rougher workpiece so it should also result in a rougher surface on the abrasive grains. The effect of changing the dressing depth on the fracture surface of a single grain is shown in Figure 7.8. This figure shows that the area of removed grain is rapidly increased with dressing depth of cut.

Table 7.1 Chen and Rowe model equations versus the proposed model equations.

Dressing tool profile	Chen and Rowe	$z_d(x) = 4\frac{d_h}{{d_w}^2}x^2$
	Proposed	$z_d(x) = a_0 + a_1x + a_2x^2 + a_3x^3 + a_4x^4 + a_5x^5 + a_6x^6$
Dressing tool trace	Chen and Rowe	$z_t(x) = a_d - z_d\left(x - f_d\, int\left(\frac{x}{f_d}\right)\right)$
	Proposed	$z_t(x) = a_d - z_d\left(x + f_d\left(\frac{\beta}{2\pi}\right) - f_d\, int\left(\frac{x + f_d\left(\frac{\beta}{2\pi}\right)}{f_d}\right)\right)$
Dressed grain profile	Chen and Rowe	$z(x) = z_t(x) + h(sin(\omega\, x + \alpha) + 1)$
	Proposed	$z(x) = z_t(x) + h(sin(\omega\, x + \alpha) + 1)$
The amplitude of the sine wave	Chen and Rowe	$h = k\frac{A_{dg}\, U_d}{f_d}$
	Proposed	$h = k\frac{{h_{dg}}^{n_1}}{{U_d}^{n_2}}$
The random frequency of the sine wave	Chen and Rowe	$\omega = \frac{4\pi\,(1+\partial)}{f_d + d_w}$
	Proposed	$\omega = \frac{\pi\,(1+\partial)}{f_d + d_w}\left(\frac{1}{{h_{dg}}^{n_1}}\right)$

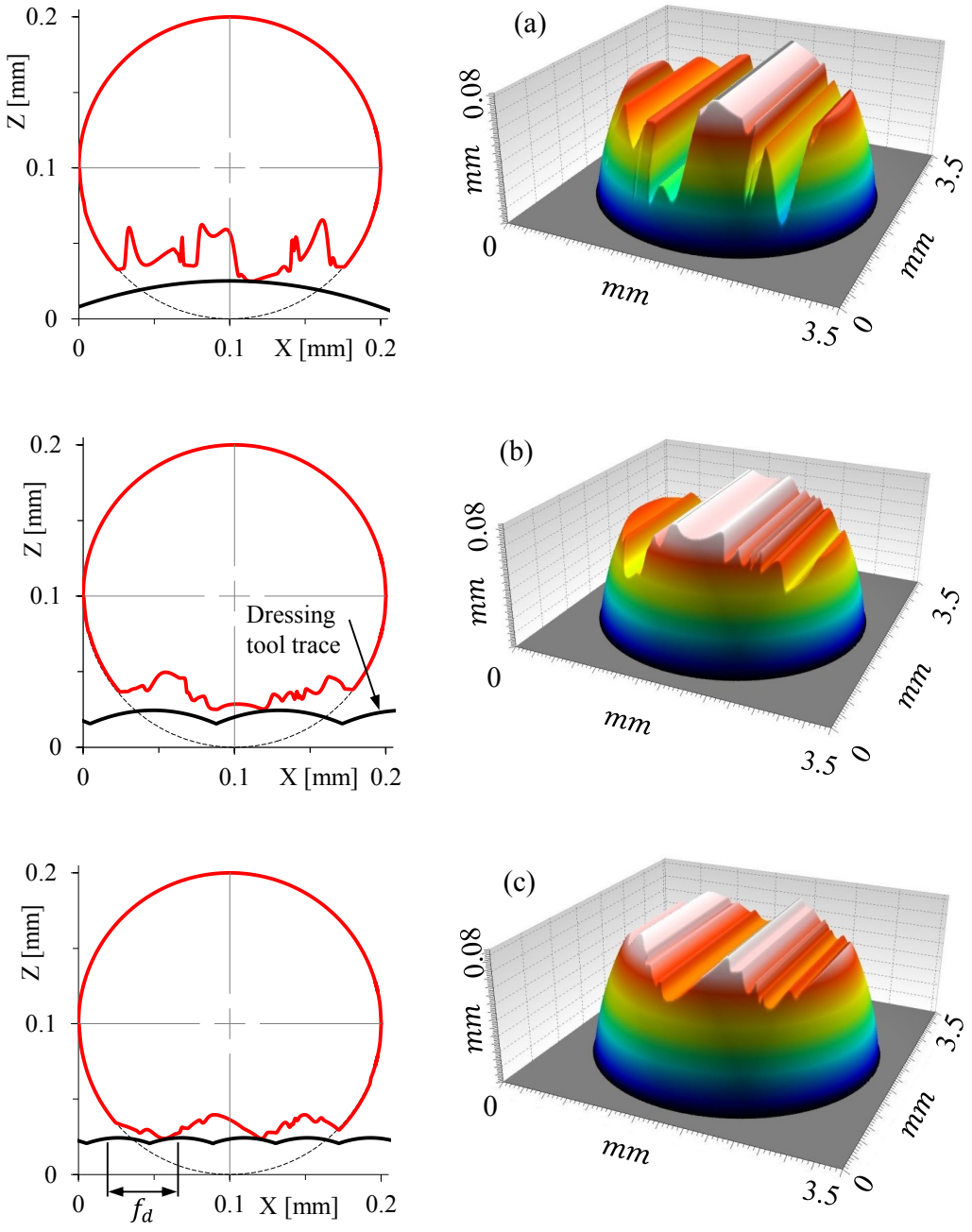

Figure 7.7 The dressing simulation for dressing depth of 0.02 *mm* and dressing feed of (a) 0.25, (b) 0.08 and (c) 0.04 *mm/rev*.

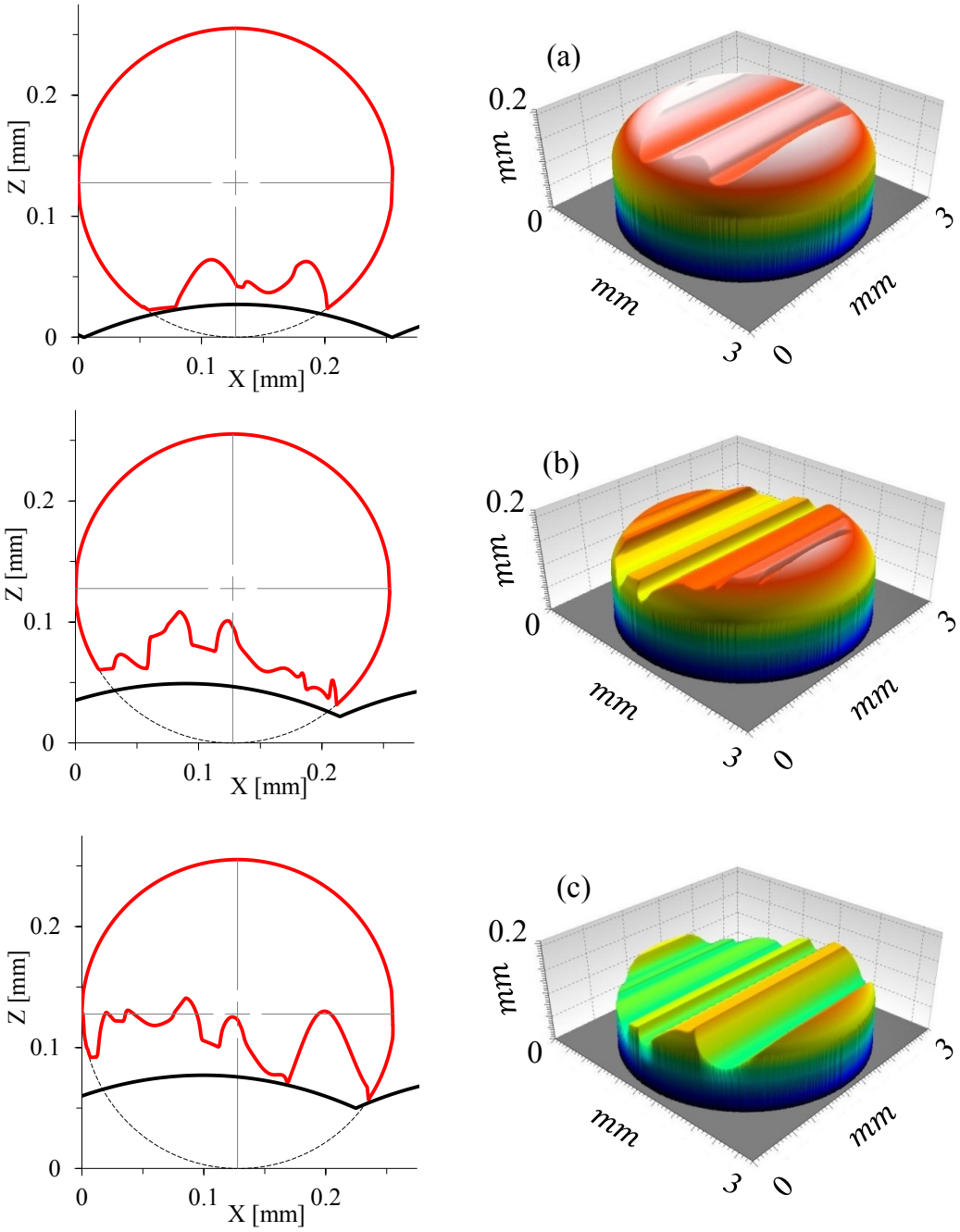

Figure 7.8 The dressing simulation for dressing lead of 0.25 *mm/rev* and dressing depth of (a) 0.02, (b) 0.025 and (c) 0.03 *mm*.

The new dressing model was applied to the 3D stochastic grinding wheel model. Subsequently, the dressed wheel model was used in the 3D metal removal simulation. In order to integrate the dressing effect in to the grinding simulation, some changes were made to the 3D metal removal model. When the 3D dressed wheel model is sectioned by a plane that is parallel to the x-y plane to generate 2D-slices, each dressed grain in the 3D wheel model will be sectioned as illustrated in Figure 7.9 (a), which shows the sectioned surface of the dressed grain in black. The cross section shape of the dressed grain is a truncated circle as shown in Figure 7.9 (b). The distance between the truncated circle center and the truncated circle side is defined by s_d. In the metal removal simulation the intersection point $f\ (x_i^f\ , y_i^f)$ between the line segment and the circle is defined (see Figure 7.9 (b)) and then it is substituted for the top point of the shortened line segment $(x_i^1\ , y_i^1)$ to simulate the cutting operation. Thus, in the modified model, the intersection point between the truncated circle and the line segment is the greater value of f and f', where the x and y components of f' are defined by the following equations:

$$x_i^{f'} = x_i^f \tag{7.18}$$

$$y_i^{f'} = y_c - s_g \tag{7.19}$$

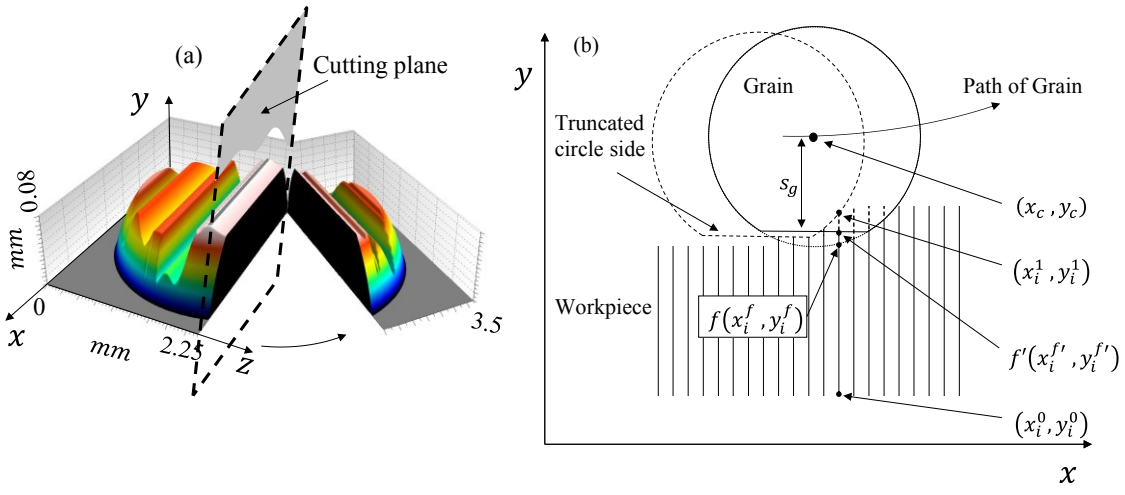

Figure 7.9 (a) Single dressed grain sectioned by the cutting plane, (b) the modified z-map with the truncated circle.

7.6 Wheel topography results

The proposed dressing model was applied to the 3D stochastic grinding wheel model of an aluminum oxide grinding wheel with a marking system of (WR-A-60-J5-V1). The dressing simulation was applied for 7 passes. For each pass the dressing depth a_d was increased by $0.02\,mm$. Dressing leads f_d of 0.04, 0.08 and 0.25 which corresponds to fine, medium and coarse dressing conditions, respectively, were used. Subsequently, the dressed 3D stochastic grinding wheel model was used for the 3D metal removal simulation to generate a machined workpiece surface. Figure 7.10 shows the grinding wheel surface before and after dressing for fine, medium and coarse dressing conditions. It can be observed from the figures that there are much more cutting edges exposed after dressing. The white color in the plotted topographies indicates the exposed cutting edges. It is clear that, as the dressing lead decreases (fine dressing condition), there are more and larger cutting edges exposed as can be noticed by the cutting edges with white color.

In order to evaluate the dressing model, the characteristics of the surface topography of the dressed wheel model were compared with the characteristics of surface topography of the wheel model before dressing and the experimental results obtained in Chapter 6. Subsequently, the surface roughness of the simulated and experimental workpiece ground surfaces were compared.

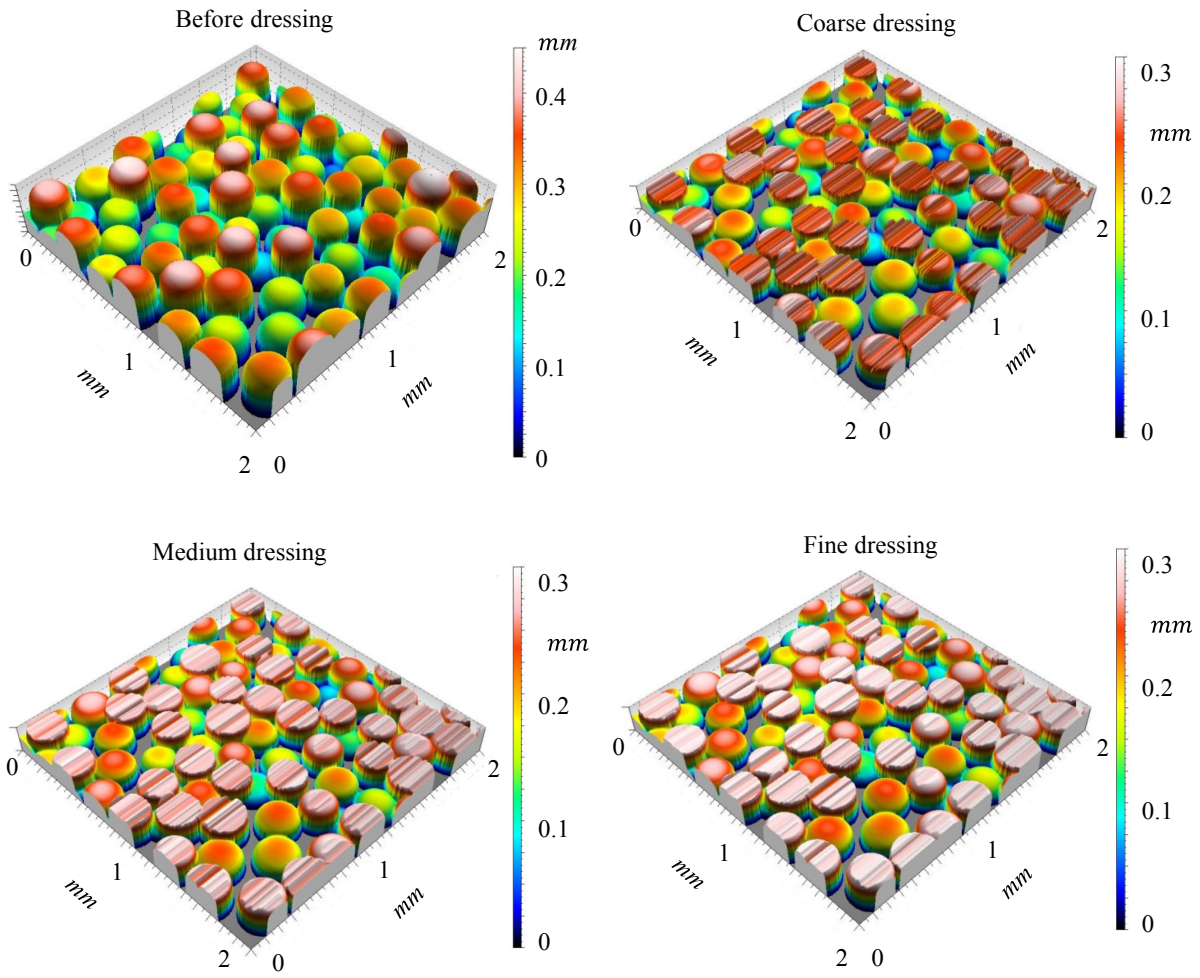

Figure 7.10 Grinding wheel surface before and after dressing.

Figure 7.11 shows the resulting binary images for 5, 30 and 80 μm threshold planes, which were applied to each dressed wheel model. These images confirm that coarse dressing conditions produce fewer and smaller cutting edges than fine dressing conditions. These images also show that, as the threshold increases, more cutting edges appear, grow, and combine with other cutting edges. At a threshold depth of 80 μm, most of the cutting edges have combined into larger cutting edges – especially for the fine dressing condition. The images show that, at small threshold depths, the cutting edges have the form of line segments that are parallel to the cutting direction because the 2D dressing model neglects grain fracture in the cutting direction. Blob analysis was utilized to extract the cutting edge density, size, protrusion height and spacing information from

the binary images of the dressed wheel models in the same manner as for the experimental results.

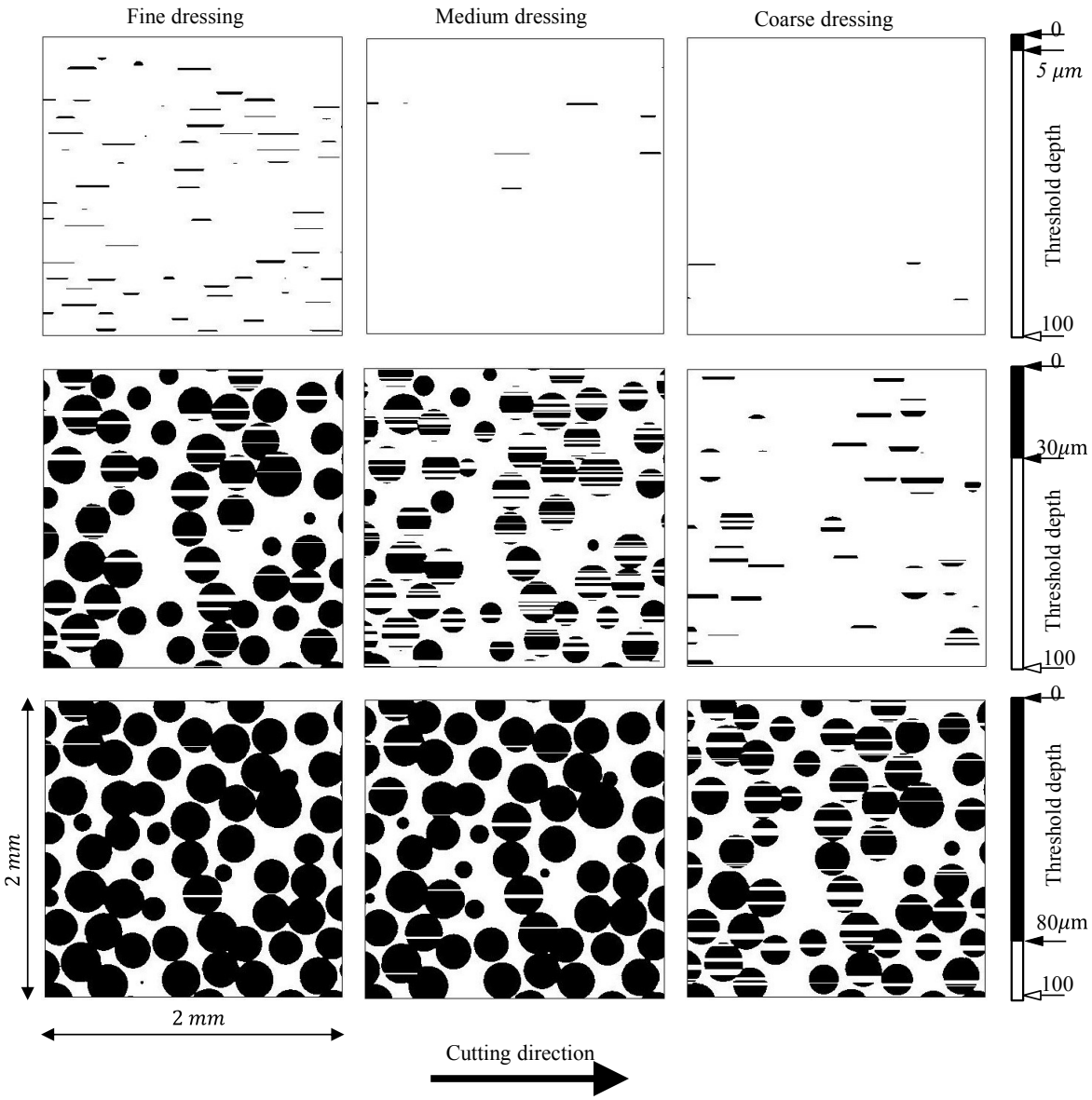

Figure 7.11 The cutting edges at threshold depth of 5, 30 and 80 μm.

In Figure 7.11 some grains seem to be overlapping, especially for the 80 μm threshold plane and for fine dressing. In fact these grains are not overlapping because they have been distributed in the wheel volume under a condition that the grains cannot overlap (refer to Section 5.2.5.2). To explain why the sectioned grains appear overlapping in the

threshold planes, 7 grains were stochastically distributed as shown in Figure 7.12 (a). As can be seen there is no interfering between the grains. However, when the upper surfaces of the grains were extracted (Figure 7.12 (b)) and sectioned by threshold plane A-A, some sectioned surfaces of the grains were overlapping, as shown in Figure 7.12 (c). For comparison the actual cross section of the grains is shown in Figure 7.12 (d). The reason for this discrepancy is due to the fact that in the extraction process only the upper surfaces of the grains can be obtained, because the lower surfaces are not visible from above. Some grains cannot be extracted because they are located underneath other grains. For example, a part of grain #2 is located underneath grain #1. As a result, grain #1 and grain #2 will appear to be overlapping. Although this problem may affect the analysis of the wheel topography, the effect will be only at high threshold depth. It should also be noted that this problem also exists with the measurements which are taken in the vertical direction.

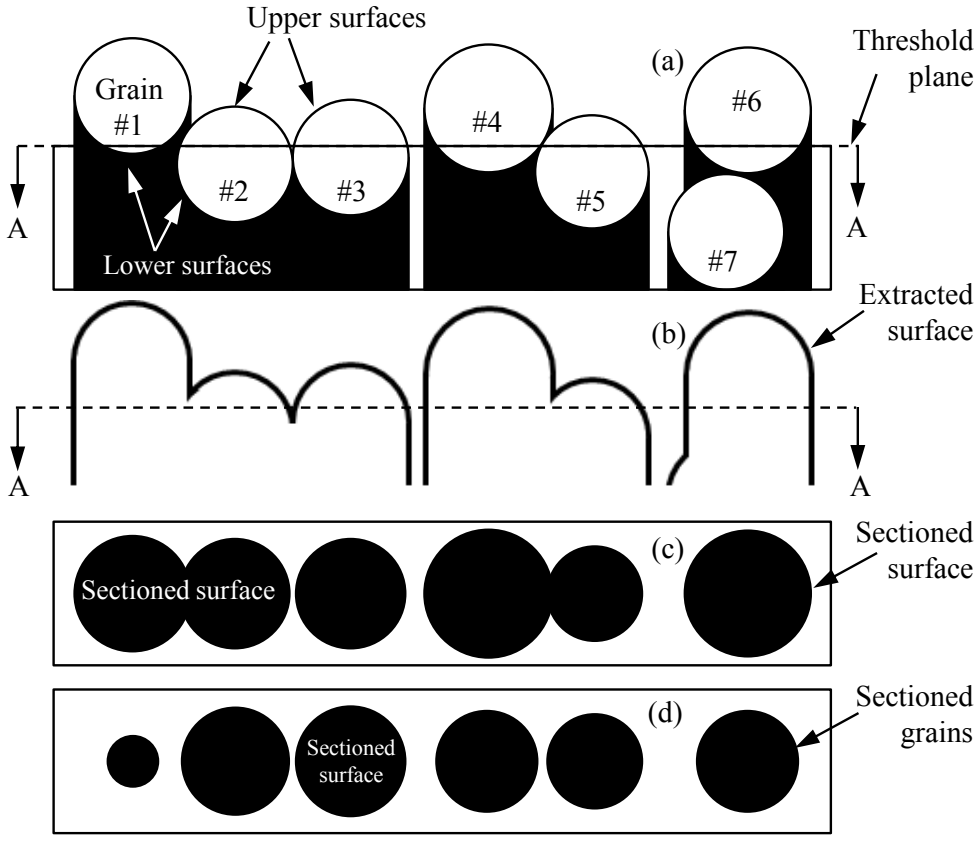

Figure 7.12 Illustration of thresholding process for extracted grains surfaces.

Figure 7.13 plots the cutting edge density, average width and average spacing versus the threshold depth for the simulated and experimental grinding wheel topography for coarse, medium and fine dressing conditions. The figure also plots the cutting edge density, average width and average spacing versus the threshold depth for the simulated and measured grinding wheel topography before dressing. In the case of the measured grinding wheel, before dressing refers to a grinding wheel that has been roll dressed with a dressing ratio of 1.1 in order to minimize the effect of ductile cutting on the wheel topography. Note that, in this discussion, the before dressing case will be discussed first, followed by the dressing cases, followed by a discussion of some possible reasons for the differences in the measured and simulated results.

Before dressing the cutting edge density, the average width and the average spacing behave in a similar manner (the curves have similar shape); however, their values have some differences. The cutting edge density and average width slowly increase with the threshold depth while the average spacing decreases in an exponential fashion. The reason for some of the differences between the simulated and experimental results for the undressed case may be because roll dressing does not completely prevent grain fracture, which means the abrasive grains will have multiple cutting edges. Whereas, in the simulated undressed wheel model there is just one cutting edge per grain as shown in Figure 7.10. Furthermore, the roll dressing process may have caused some grain dislodgement which most likely affected the results as well.

Although, the simulated and experimental results after dressing are not identical, the dressing model has significantly improved the match between the experimental and simulated grinding wheel surface, as shown in Figure 7.13. After dressing, the simulated and experimental results still behave in the same manner as the threshold depth increases. The dressing operation has increased the cutting edge density for both the simulated and experimental wheels topographies, especially when dressing conditions get finer. The simulated and experimental maximum cutting edge densities after dressing are listed in Table 7.2. The dressing operation also decreased the average cutting edge spacing in both the simulated and experimental results. The simulated and experimental average cutting

edge spacing decreases when the threshold became larger and/or the dressing condition became finer. For the average cutting edge width the simulated and experimental results show that, as the threshold depth increases, the average cutting edge width slowly increases and then rapidly increases, as shown in Figure 7.13. At small threshold depths (less than 20 μm), the simulation and experimental results have good agreement, which is important because the vast majority of generated chips have thicknesses that are smaller than this level, as will be shown in Section 7.8. In Figure 7.13 the simulated cutting edge width increases up to around 0.3 mm, which is greater than the average of the grain diameter. The reason the cutting edge width in the simulated results exceeds the average of the grain diameter is because some sectioned grains in the threshold plane were overlapping and joined into one large cutting edge, as shown in Figure 7.12. Another reason is due to the fact that the dressing simulation did not take the bond fracture and grain dislodgement into account.

Table 7.2 Maximum cutting edge density for experimental and simulated result.

	Experimental result	Simulated result
Cutting edge density for coarse dressing [$\#/mm^2$]	16.7	29.4
Cutting edge density for medium dressing [$\#/mm^2$]	27.7	34
Cutting edge density for fine dressing [$\#/mm^2$]	35.5	31.5

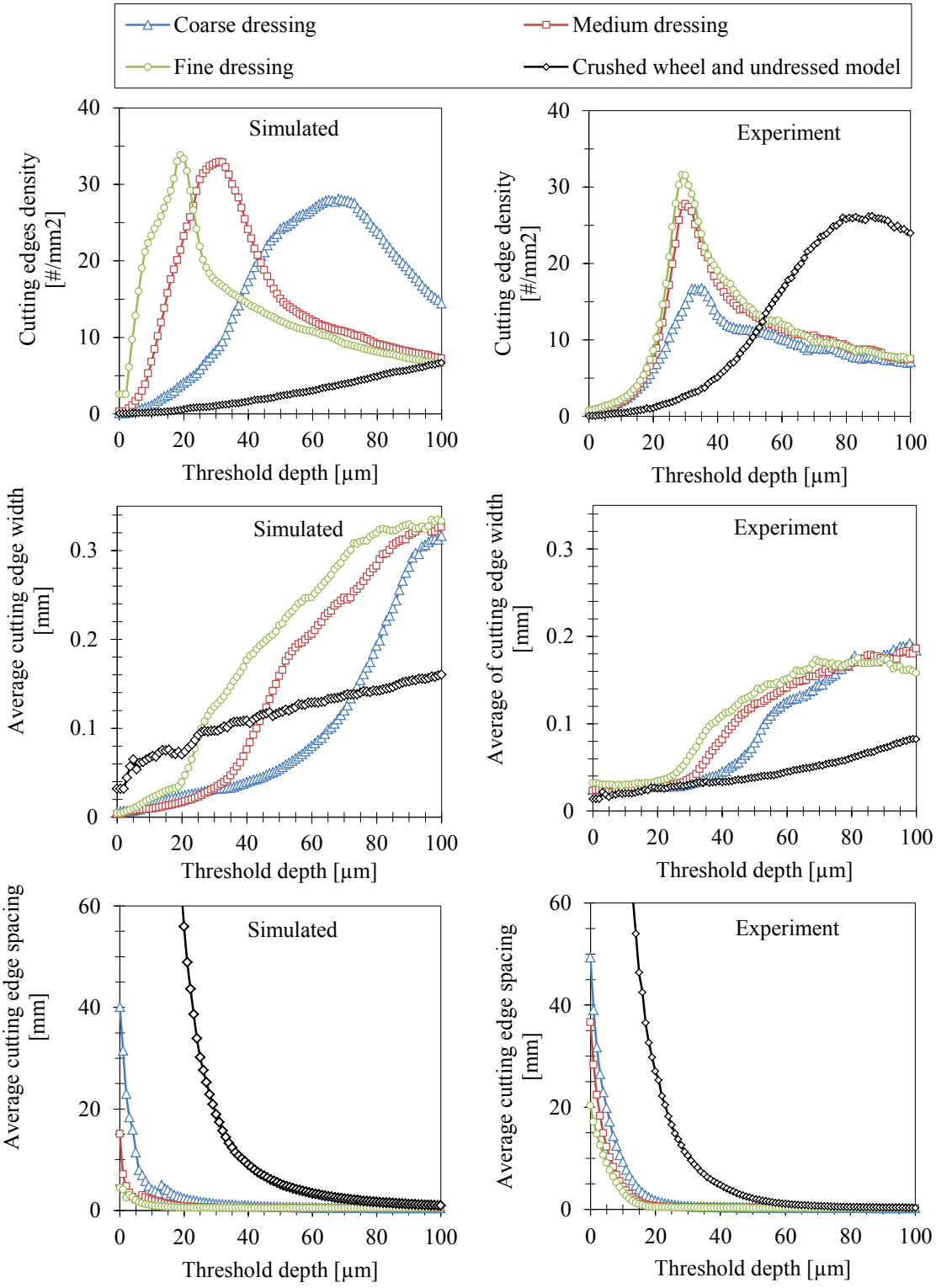

Figure 7.13 Simulated and experimental cutting edge density, average cutting edge width and average cutting edge spacing vs. threshold depth.

Although there were significant improvements in the grinding wheel topography after dressing, there were some differences. The maximum cutting edge densities are different and occur at different threshold depth – especially in coarse and fine dressing conditions. Also, the values of the cutting edge width and spacing have some differences. These differences may be due to the fact that the dressing model did not take the grain dislodgement (bound fracture) into account, or because the dressing model was developed for a 2D grinding wheel model. Figure 7.14 plots the simulated and experimental grinding wheel profiles in the cutting direction (x-direction) and in the axial direction of the grinding wheel (z-direction) for the coarse dressing conditions. The profiles in the axial direction are similar in shape; however, the simulated profile appears to have more cutting edges than the experimental profile (36 versus 22 cutting edges). Conversely, fewer cutting edges appear in the simulated profile than in the experimental profile (10 versus 25 cutting edges) for the direction of cutting. These results probably mean that the simulated chips are a little narrower and longer than they should be. The reason why there were few cutting edges in the simulated profile in the cutting direction is that the dressing model neglects the grain fracture in the cutting direction.

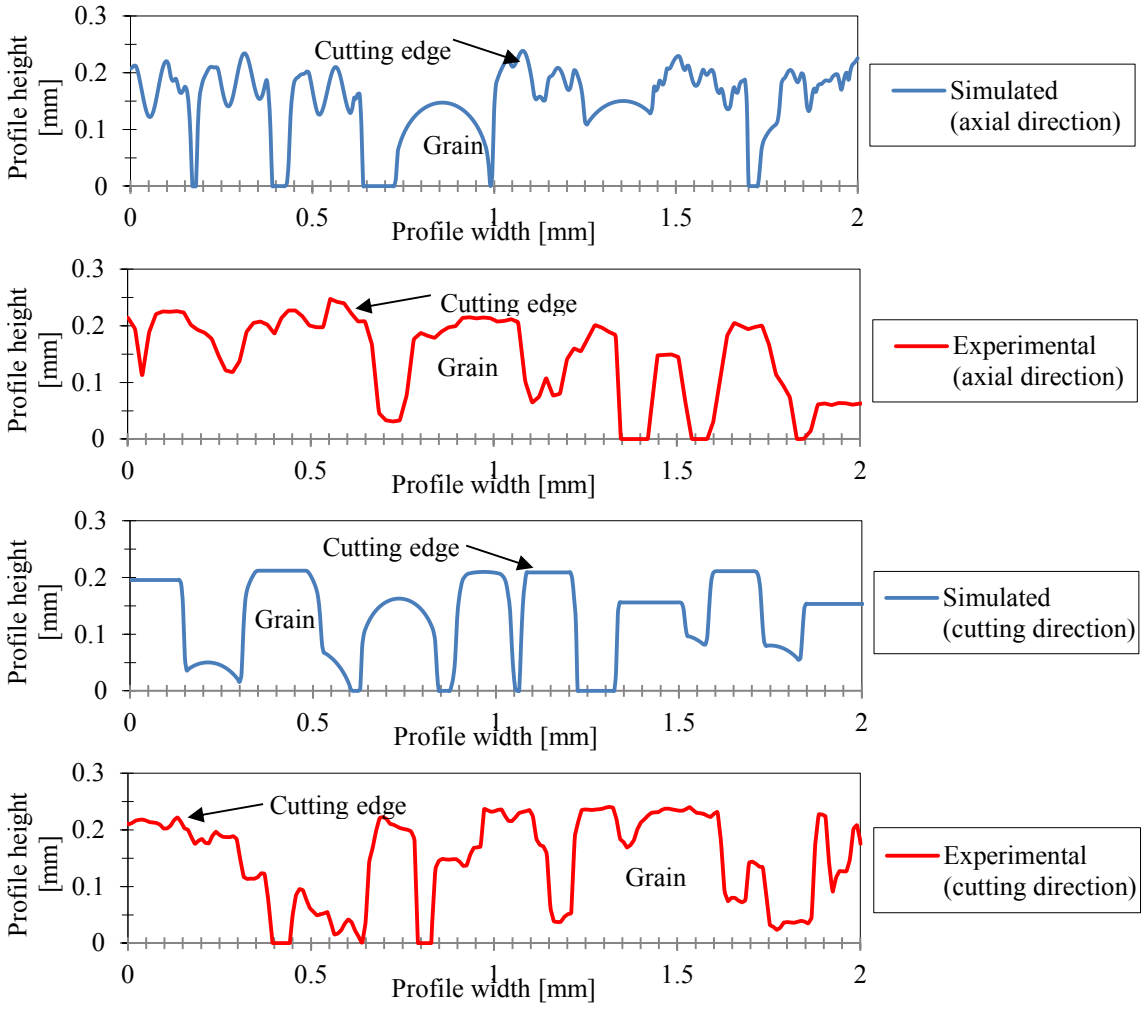

Figure 7.14 The cross-section of the simulated and experimental 3D grinding wheel topography for the dressing lead of 0.25 *mm/rev* in the cutting and axial directions.

7.7 Ground surface result

Simulated ground surface topologies were compared to experimental results to validate the proposed model. The dressing depth was 0.02 mm and the dressing leads were 0.25, 0.08, and 0.04 mm/rev. The grinding wheel diameter was 354.057 mm, the depth of cut was 0.03 mm, the cutting speed was 20 m/s and the workpiece speed was 0.03 m/s. The ground surface was also generated for the undressed wheel model using the same grinding parameters. Figure 7.15 plots the simulated and experimental profiles of the

ground surfaces of the workpiece. After dressing the surfaces roughness of the ground surfaces were significantly improved. The profiles are remarkably similar in both amplitude and frequency content for all dressing conditions. For instance, the frequencies of the simulated and experimental profiles for the dressing lead of $0.25\ mm/rev$ were 39.5 and 37 $peak/mm$ and the amplitudes were 8.9 and 7.2. As shown in Table 7.3, the surfaces roughness of the simulated profiles were improved after dressing and have an excellent agreement with the experimental profiles.

Table 7.3 Experimental and simulated surface results.

Dressing lead f_d		0.25	0.08	0.04	Before dressing
Surface Roughness R_a $[\mu m]$	Simulation	1.1	0.7	0.29	2.26
	Experimental	0.97	0.43	0.27	--
Frequency $[peak/mm]$	Simulation	39.5	37.5	40.5	21
	Experimental	37	30.5	32	--
Amplitude $[\mu m]$	Simulation	8.9	7.9	3.3	19.9
	Experimental	7.2	5.5	2.9	--

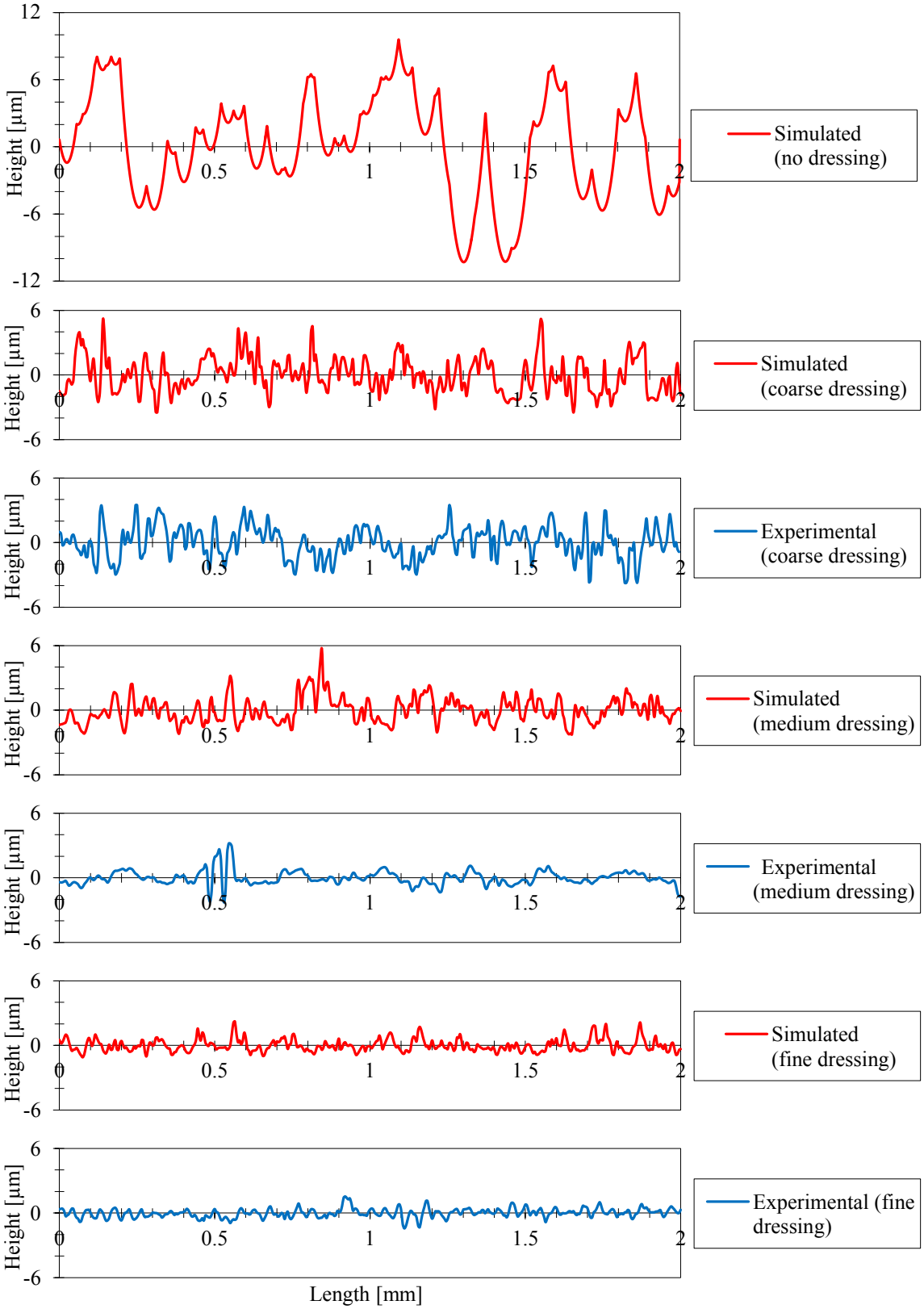

Figure 7.15 The simulated and experimental profiles of the ground surfaces.

7.8 Uncut chip thickness and contact length result

Simulations of metal removal were also carried out using different grinding depths of cut (from 0.01 to $0.1\,mm$) to calculate the uncut chip thickness and contact length for a grinding wheel model with coarse dressing conditions. The undressed wheel model was also simulated for comparison. The grinding parameters used in the simulations were as follows: wheel diameter was $354.04\,mm$, cutting speed was $20.0\,m/s$ and workpiece speed was $0.03\,m/s$.

The average uncut chip thickness and contact length for grinding wheel models before and after dressing versus depth of cut are plotted in Figure 7.16 and Figure 7.17. The figures also plot the uncut chip thickness and contact length that were determined by the analytical models using Equation (5.23) and Equation (5.24) versus depth of cut. The differences between the simulated and analytical results for the uncut chip thickness significantly increased when using the dressed wheel model. For the contact length the differences in the simulated result before and after dressing were small. However, there were still significant differences between the simulated and analytical results. Table 7.4 lists the chip geometry produced by the wheel models before and after dressing for a depth of cut of $0.1\,mm$. The simulated result shows that, for the depth of cut of $0.1\,mm$, the average uncut chip thickness has increased from $3.4\,\mu m$ before dressing to $7.9\,\mu m$ after dressing, whereas the uncut chip thickness determined by the analytical model was just $0.21\,\mu m$. Also, at a depth of cut of 0.1 the analytical contact length was $5.6\,mm$, whereas the simulated contact length using the wheel model before and after dressing was 2.7 and $3.0\,mm$, respectively. It is also important to note that the dressed wheel model produced more chips that are thicker and longer; however, the wheel model before dressing produced chips that are much wider (50.3 versus $3.1\,\mu m$).

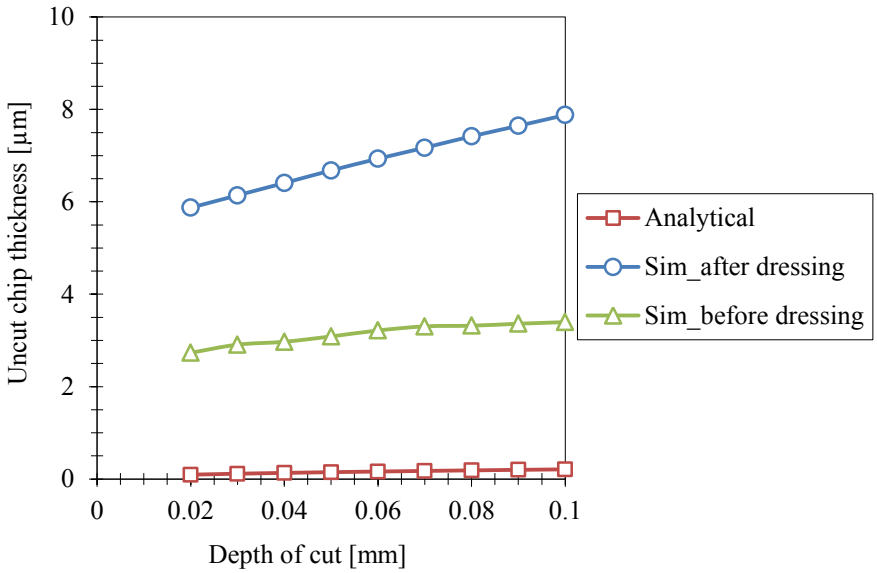

Figure 7.16 The Simulated and Analytical uncut chip thickness vs. the depth of cut.

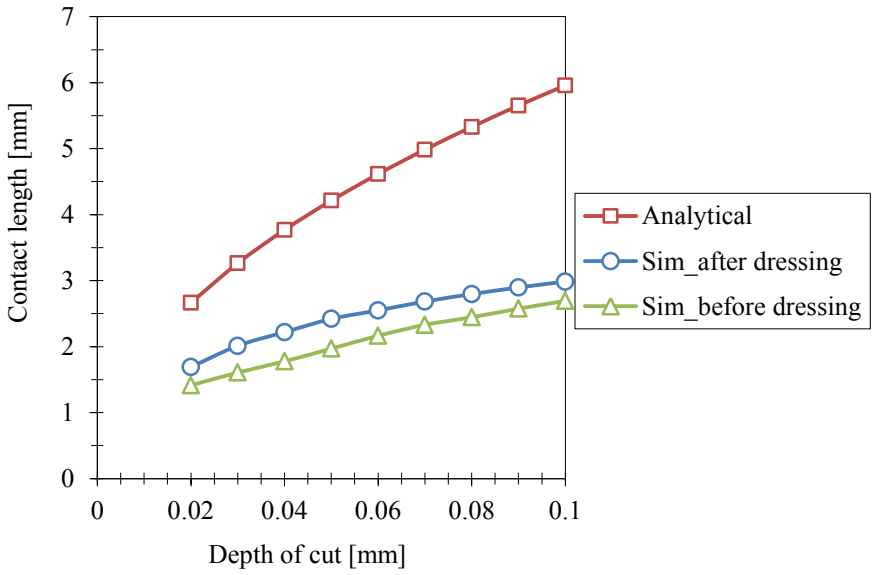

Figure 7.17 The Simulated and Analytical contact length vs. the depth of cut.

Table 7.4 Chips information for depth of cut of 0.1 mm.

	Before dressing	After dressing	Analytical
Average uncut chip thickness [μm]	3.4	7.9	0.2
Average contact length [mm]	2.7	3.0	6.0
Average chip width [mm]	50.3	3.1	--
Number of chips	425	17973	--

Figure 7.18 plots the percentage of active cutting edges versus the depth of cut for the wheel model before and after dressing. The percentage of active cutting edges increased when the dressed wheel model was used, perhaps because the dressed wheel model has more cutting edges than the undressed wheel model. However, the number of active cutting edges is still small, only 27 % of the cutting edges were active at the depth of cut of 0.1 mm.

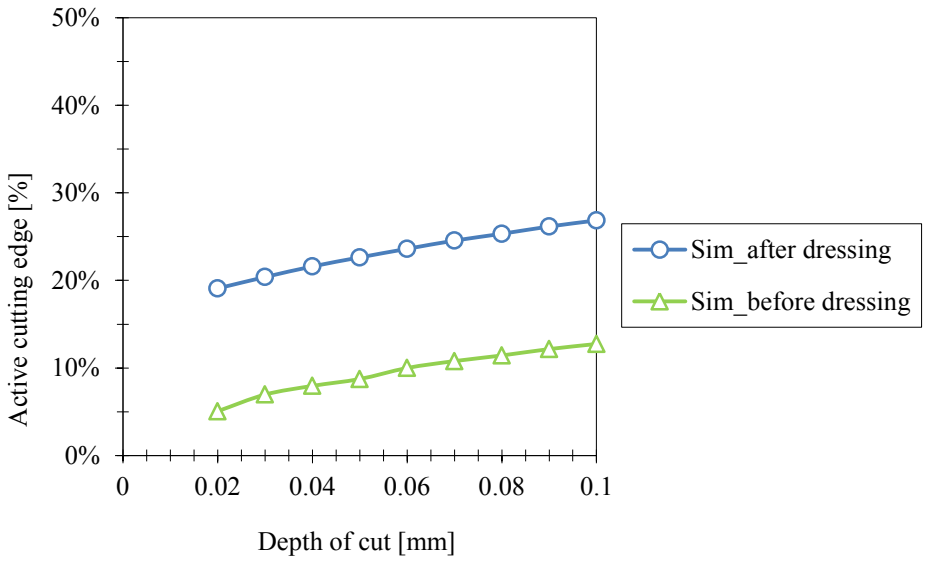

Figure 7.18 Active cutting edge vs. depth of cut.

Figure 7.19 and Figure 7.20 show the distributions of the uncut chip thickness and contact length for the chips that were produced at a depth of cut of $0.1\ mm$ using the wheel models before and after dressing. The distribution of the uncut chip thickness has changed from the gamma distribution to a normal distribution after dressing. This change may also explain why the uncut chip thickness has increased after dressing, because before dressing the uncut chip thickness for more than 70% of the chips was less than $4\ \mu m$ while more than 60% were between 8 and $10\ \mu m$ after dressing. For the contact length histogram, a uniform distribution would be most appropriate for both the chips produced by the dressed wheel model and the wheel model before dressing.

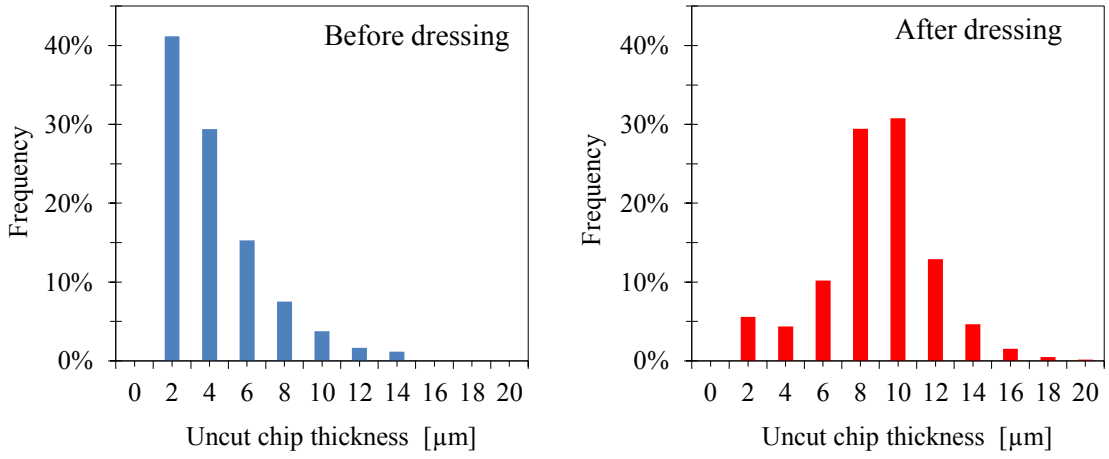

Figure 7.19 The distribution of the uncut chip thickness.

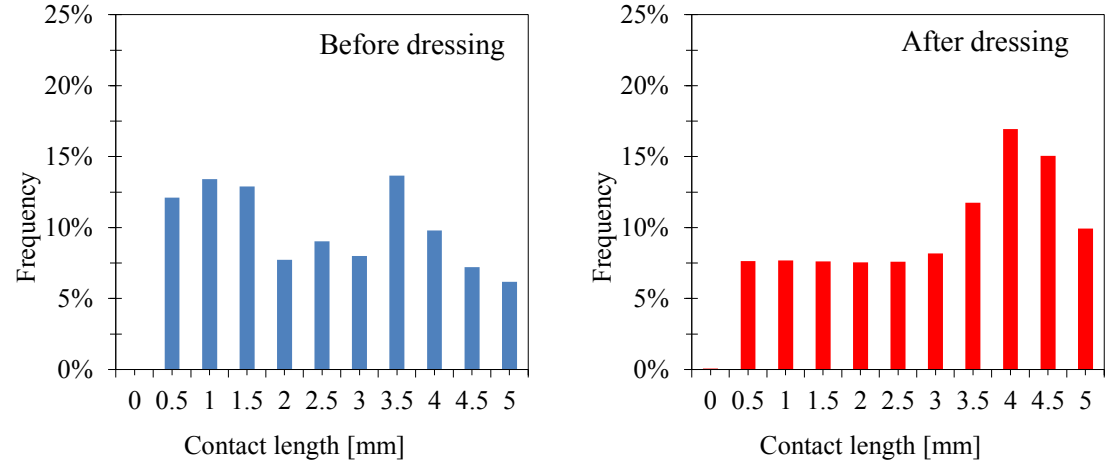

Figure 7.20 The distribution of contact length.

The reasons for the differences between the undressed and the dressed models can be explained using Figure 7.21, which shows an active grain from the undressed wheel model and another active grain from the dressed wheel model. The figure shows multiple cutting edges for the dressed grain and just one cutting edge for the undressed grain. The figure also plots the maximum uncut chip thickness and contact length produced by the active cutting edges on the grains as a function of the grain width. As can be seen, the cutting edges on the dressed grain produced three chips, while one chip was produced by the undressed grain. Due to the surface condition of the workpiece before cut, the chip that was produced by the undressed grain is not symmetrical around the grain center. The average uncut chip thickness, contact length and chip width are listed in Table 7.5. The average uncut chip thickness and contact length for the chips produced by the dressed grain are larger than the average uncut chip thickness and contact length produced by undressed grain; however, the width of the chip produced by the undressed grain is wider than the average width of the chips produced by the dressed grain.

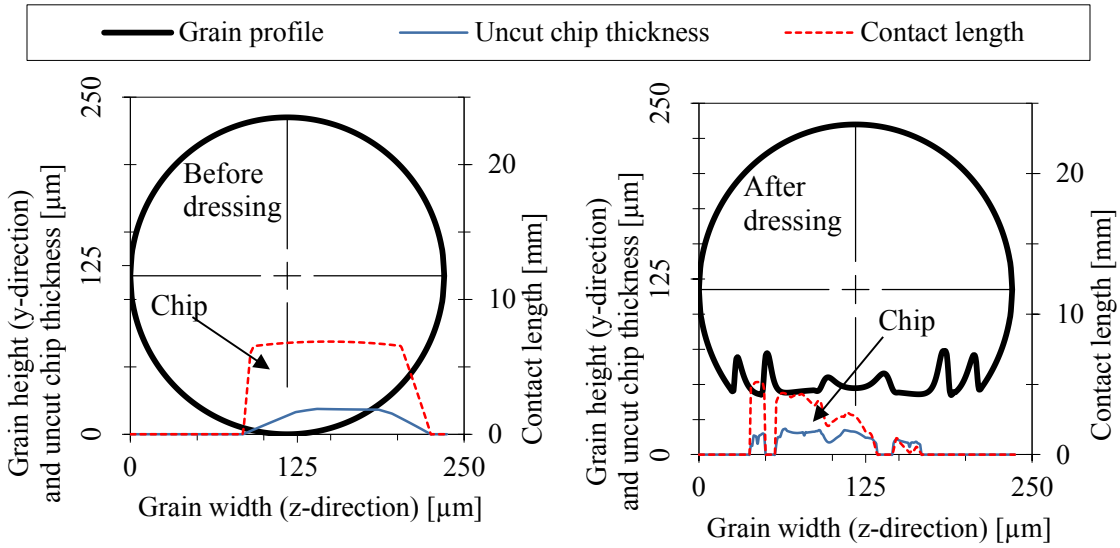

Figure 7.21 Active dressed grain with muliple chips.

Table 7.5 The uncut chip thickness, contact length and chip width produced by dressed and undressed active grain.

		Uncut chip thickness $[\mu m]$	Contact length $[mm]$	Chip width $[mm]$
Dressed grain	Chip 1	11.9	5.0	11
	Chip 2	14.2	3.1	76
	Chip 3	8.8	0.5	21
	Average	11.6	2.9	36
Undressed grain		7.9	2.8	140

7.9 Summary

A novel simulation of the dressing operation using a single-point dressing tool in grinding was presented. The dressing model was applied to the grinding wheel model using coarse, medium and fine dressing conditions. The surface roughness of the simulated ground surface was also compared with experimental ground surface under different dressing conditions and excellent agreement was obtained. The dressed grinding wheels topographies were compared with experimentally measured grinding wheels topographies. The dressing model improved the correspondence between the grinding wheel model and the measurements but it is evident that improvements in the dressing model are required. The dressed wheel model under coarse dressing conditions and the undressed wheel model were then used in the metal removal simulation to investigate the effect of the dressing model on the uncut chip thickness, contact length and the percentage of the active cutting edge for different grinding depth of cut. The distributions of the uncut chip thickness and contact were also defined for both the undressed and dressed wheel models.

CHAPTER 8. CONCLUSION

8.1 Conclusion

The objectives of this work were to develop a method to accurately measure the entire surface of the grinding wheel in 3D, to develop a method to model the surface topography of grinding wheel in 3D with and without dressing, to develop a metal removal simulation to determine the uncut chip geometry for each cutting edge on the wheel surface and to predict the surface finish of the workpiece and to study the effects of dressing on the surface topography of grinding wheels and the geometric aspect of grinding in 3D. All these objectives were achieved as will be addressed in the following sections.

8.1.1 The 3D grinding wheel measuring system

A new measurement system of grinding wheel topography was developed. It could measure the entire surface of a grinding wheel in a non-destructive manner. The new system utilized the axial chromatic technique to provide non-contact measuring system. The system achieved planer resolution of $1\,\mu m$ and a depth resolution of $25\,nm$. The

capabilities of this system surpass any other grinding wheel measurement technology reported in the literature.

8.1.2 3D grinding wheel model

A 3D grinding wheel model was built based solely on the information obtained from the wheel marking system, subsequently; the model was subjected to a dressing simulation to generate cutting edges on the grinding wheel surface. The results obtained from the grinding wheel measuring system were used to improve the proposed dressing model. These models were used in conjunction with the metal removal simulation to study the effects of wheel topology on the geometric aspects of grinding metal removal. The 3D grinding wheel model after dressing is a unique model because it model the grinding wheel by modeling every grain in a grinding wheel.

8.1.3 Metal removal simulation

A 2D simulation of metal removal in grinding was developed to investigate the effect of the stochastic distributions of the grain size, spacing and protrusion height on the calculation of the uncut chip thickness and contact length and it was found that the protrusion height had the greatest influence on the results. The metal removal simulation was also used to determine the uncut chip thickness, contact length and surface finish using the 3D grinding wheel model before and after dressing. The dressed model significantly improved the result of the uncut chip thickness, contact length and surface finish. The simulations suggest that the average uncut chip thickness may be forty times larger than that calculated using conventional analytical models, while the chip length may be half the calculated using conventional analytical models. The uncut chip thickness conforms to a normal distribution, whereas uniform distribution was the most appropriate for the contact length. The simulation also predicted that the number of active cutting edges was between 19 and 27 % of the total cutting edges on the surface of the grinding wheel. It was found that as the depth of cut increases more cutting edges are involved in the cutting process. Furthermore, the 3D model was able to calculate instantaneous material removal, which was one of the chief advantages of this approach

as it opens the door to better force and power models for grinding. The 3D model was also able to map the uncut chip geometry information to individual cutting edges that were exposed on the grinding wheel surface. The grinding experiments were carried out to demonstrate that this novel approach was able to accurately predict the workpiece surface roughness. The comparison between the characteristics of the simulated and experimental workpiece surfaces had an excellent agreement.

8.1.4 The effect of dressing on the grinding wheels topography

The grinding wheel measuring system was used to study the effect of dressing on the grinding wheel topography under different dressing conditions. The number, width and spacing of cutting edges as a function of depth into the grinding wheel were quantified. Cutting edge protrusion height was found to be normally distributed, while cutting edge width and spacing were found to be exponentially distributed regardless of the dressing condition. The coarse dressing condition produced smaller, fewer and more widely-spaced cutting edges than the medium or fine dressing conditions. Furthermore, dressing was found to noticeably affect the grinding wheel surface down to a depth of 80 μm. It was suggested that at small threshold depth the dressing conditions dominate the grinding wheel topography, whereas it is the grain size and grain distribution that dominate the grinding wheel topography for large threshold.

8.2 Recommendations

The measurement and simulation tools developed in this work have significant future scientific applications. The grinding wheel measuring system can be used to examine the links between grinding wheel topology, grinding mechanics and grinding process outputs such as surface finish and workpiece burn for different types of wheels. In terms of improving the technology of the scanner two improvements could be made relatively easily. First, encoder feedback on the spindle drive would improve velocity regulation which would improve accuracy in the circumferential direction. Second, a chromatic sensor with greater light sensitivity and resolution would be an asset since it would allow for the scanning of individual grains.

The basic grinding wheel model worked extremely well for the wheel studied. It is suggested that further validation using grinding wheels of different grain size would be advisable. The 2D nature of the dressing model was somewhat problematic. A 3D dressing model would do a better job of capturing the topographic features of a grinding wheel. Two approaches could be used. The first approach would involve using a fracture surface based on randomized mathematical functions. The second approach would involve measuring the entire grinding wheel surface and converting the measurements into a surface that would replace the entire wheel model.

The metal removal simulation appears to perform flawlessly. Given the same assumption used in the classical methods of estimating uncut chip thickness and contact length it has produced exactly the same results. However, the experimental validation of the simulation is limited. It can replicate the surface finish produced experimentally but there is no other experimental evidence that the chip geometry predicted is accurate. Ideally further work validate the simulation would be conducted. A natural extension of the metal removal simulation is to add a force and power prediction capability to it. Numerous examples of accomplishing this can be found in the conventional literature for converting chip measurements into force estimate the simplest is to multiply the instantaneous metal removed by an appropriate specific force value. A more sophisticated approach might be to combine the uncut chip thickness measurements with a finite element simulation.

REFERENCES

1. Komanduri, R., (1993), *Machining and Grinding: a Historical Review of the Classical Papers*. Applied Mechanics Reviews. (46) 80-132.
2. Malkin, S. and Guo, C., (2008), *Grinding Technology: Theory and Applications of Machining with Abrasives*. Second edition. New York. Industrial Press.
3. Peklenik, J., (1957), *Ermittlung von Geometrischen und Physikahschen KenngróBen fur die Grundlagenforschung Beim Schleifen*. Dr Ing. Dissertation, RWTH Aachen, Germany.
4. Association Canadienne de Normalisation, (1977), *Markings for Identifying Grinding Wheels and other Bonded Abrasives*. American National Standard Institute, New York.
5. Malkin, S. and Anderson, R. B., (1972), *Active Grains and Dressing Particles in Grinding*. In Proceedings of the International Grinding Conference. 161.
6. Marinescu, I. D. Rowe, W. B. Dimitrov, B. and Inasaki, I., (2004), *Tribology of Abrasive Machining Processes*. Norwich, N. Y. William Andrew Pub.
7. Lal, G. K. and Shaw, M. C., (1972), *Wear of Single Abrasive Grains in Fine Grinding.* In Proceedings of the International Grinding Conference. 107.
8. Malkin, S., (1971), *Selection of Operating Parameters in Surface Grinding of Steels*. Journal of Engineering for Industry, Transactions of the ASME. (93) 1120-1128.
9. Shih, A. J., (2000), *An Experimental Investigation of Rotary Diamond Truing and Dressing of Vitreous Bond Wheels for Ceramic Grinding*. International Journal of Machine Tools and Manufacture. (40) 1755-1774.
10. Doman, D. A. Warkentin, A. and Bauer, R (2006). *A survey of Recent Grinding Wheel Topography Models*. International Journal of Machine Tools and Manufacture. (46) 343-352.
11. Chen, X. and Rowe, W. B., (1996), *Analysis and Simulation of the Grinding Process. part I: Generation of the Grinding Wheel Surface*. International Journal of Machine Tools and Manufacture. (36) 871-882.

12. Koshy, P. Jain, V. K. and Lal, G. K., (1993), *A Model for the Topography of Diamond Grinding Wheels*. Wear. (169) 237-242.
13. Koshy, P. Jain, V. K. and Lal, G. K., (1997), *Stochastic Simulation Approach to Modelling Diamond Wheel Topography*. International Journal of Machine Tools and Manufacture. (37) 751-761.
14. Hegeman, J. B. J. W., (2000), *Fundamentals of Grinding: Surface Conditions of Ground Materials*. University of Groningen, Netherlands.
15. Xie, J. Xu, J. Tang, Y. and Tamaki, J., (2008), *3D Graphical Evaluation of Micron-scale Protrusion Topography of Diamond Grinding Wheel*. International Journal of Machine Tools and Manufacture. (48) 1254-1260.
16. Verkerk, J. Peters, J., (1977), *Final Report Concerning CIRP Cooperative Work in the Characterization of Grinding Wheel Topography*. Annals of the CIRP. (26) 385-395.
17. Backer, W. R. Marshall, E. R. Shaw, M. C., (1952), *The Size Effect in Metal Cutting*. Trans. ASME. (74) 61-72.
18. Tönshoff, H. K. Peters, J. Inasaki, I. and Paul, T., (1992), *Modelling and Simulation of Grinding Processes*. CIRP Annals Manufacturing Technology. (41) 677-688.
19. Kassen, G., (1969), *Beschreibung der Elementaren Kinematik des Schleifvorganges*. Dr Ong. Dissertation, TH Aacahen, Germany.
20. Werner, G., (1971), *Kinematik und Mechanik des Schleifprozesses*. Dr Ing. Dissertation, TH Aachen, Germany.
21. Lortz, W., (1975), *Schleifscheibentopographie ung Spanbildungsmechanismus bein Schleifen*. Dr Ing. Dissertation, TH Aachen, Germany.
22. Triemel, J., (1975), *Untersuchungen zum Stirnschleifen von Schnellarbeitsstálen mit Bornitridwerkzeugen*. Dr Ing. Dissertation, TU Hannover, Germany.
23. Yegenoglu, K., (1986), *Berechnung von TopogrpahiekengróBen zur Auslegung von CBN-Schleifprozessen*. Du Ing. Dissertation, RWTH Aachen.

24. Brüttner, A., (1968), *Das Schleifen Sprödharter Werkstoffe mit Diamant-Topfscheiben Unter Besonderer Berücksichtigung des Tiefschleifens*. Dr. Ing. Dissertation TU Hannover.
25. Mandelbrot, B. B., (1975), *Les Objects Fractales*. Flammarion, France.
26. Shangping, L. Jie, L. Li, L. Shousheng, C. Wengui, S. and Huiqin, P., (2003), *Study of the Ground Workpiece Surface Topography in High-speed Precision Grinding using a Scanning Tunneling Microscopy*. Journal of Materials Processing Technology. (139) 263-266.
27. Zhang,Y. Luo,Y. Wang, J. F. and Li, Z., (2001), *Research on the Fractal of Surface Topography of Grinding*. International Journal of Machine Tools Manufacture. (41) 2045-2049.
28. Bigerelle, M. Najjar, D. and Iost, A., (2005), *Multiscale Functional Analysis of Wear a Fractal Model of the Grinding Process*. Wear (258) 232-239.
29. Warren, T. L., (1995), *Fractal and DDS Characterization of Diamond Wheel Profiles*. Journal of Materials Processing Technology. (53) 567-581.
30. Hou, Z. B. and Komanduri, R., (2003), *On the Mechanics of the Grinding process – part I. Stochastic Nature of the Grinding Process*. International Journal of Machine Tools Manufacture. (43) 1579-1593.
31. Yuhta, T. Igarashi, S. Okuma, R. and Satoh, T., (1976), *On the Surface Nature of Diamond Wheel in the Process of Grinding Carbon Steel*. Ann. CIRP. (27) 255-1976.
32. Syoji, K. Zhou, L. and Matsui, S., (1990), *Studies on Truing and Dressing of Diamond Wheels*. Bulletin of the Japan Society of Precision Engineering. (27) 255.
33. Ohmori, H. and Nakagawa, T., (1990), *Mirror Surface Grinding of Silicon Wafers with Electrolytic In-process Dressing*. CIRP Annals Manufacturing Technology. (39) 329-332.
34. Uematsu, T. Suzuki, k. Yanase, T. and Nakagawa, T., (1995), *Recent Advancement in On-machine Trueing for Metal Bonded Diamond Wheels*. In Proceeding of the International Symposium for Electromachining. 409-418.

35. Davis, C. E., (1974), *The Dependence of Grinding Wheel Performance on Dressing Procedure*. International Journal of Machine Tool Design and Research. (14) 33-52.
36. Syoji, K. Zhou, L. and Matsui, S., (1990), *Studies on truing and dressing of diamond wheels (1st report). the measurement of protrusion height of abrasive grains by using a stereo pair and the influence of protrusion height on grinding performance*. Bulletin of the Japan Society of Precision Engineering. (24) 124.
37. Bakhtiarov, S. A., (1989), *Efficiency of Diamond Wheels after Contact-erosion Dressing*. Soviet Engineering Research. (9) 108-109.
38. Lonardo, P. M. Trumpold, H. and De Chiffre, L., (1996), *Progress in 3D Surface Microtopography Characterization*. CIRP Annals (45) 589-598.
39. Blunt, L. Ebdon, S., (1996), *The Application of Three-dimensional Surface Measurement Techniques to Characterizing Grinding Wheel Topography*. International Journal of Machine Tools Manufacture. (36) 1207-1226.
40. Nguyen, A. T. Butler, D. L., (2008), *Correlation of Grinding Wheel Topography and Grinding Performance: a Study from a Viewpoint of Three-dimensional Surface Characterisation*. Journal of Materials Processing Technology. (208) 14-23.
41. Yan, L. Zhou, Z. Jiang, F. Rong, Y., (2010), *The Application of Three-Dimensional Surface Parameters to Characterizing Grinding Wheel Topography*. Advanced materials research. (126) 603-608.
42. Matsuno, Y. Yamada, H. Harada, M. and Kobayashi, A., (1975), *Microtopography of the Grinding Wheel Surface with Sem*. Annals of the CIRP. (24) 237-242.
43. Weingaertner, W. L. L. and Boaron, A. L., (2011), *A Quick-Test Method to Determine the Grinding Wheel Topography Based on Acoustic Emission*. Advanced materials research. (325) 282-286.
44. Oliveira, G. J. F. Dornfeld, D. A., (1994), *Dimensional Characterization of Grinding Wheel Surface through Acoustic Emission*. CIRP Annals Manufacturing Technology. (43) 291-294.

45. LaChance, S. Warkentin, A. and Bauer, R., (2003), *Development of an Automated System for Measuring Grinding Wheel Wear Flats*. Journal of Manufacturing Systems. (22) 130-135.
46. Inasaki, I., (1996), *Grinding Process Simulation based on the Wheel Topography Measurement*. CIRP Annals Manufacturing Technology. (45) 347-350.
47. Xie, J. Wei, F. Zheng, J. H. Tamaki, J. and Kubo, A., (2011), *3D Laser Investigation on Micron-scale Grain Protrusion Topography of Truncated Diamond Grinding Wheel for Precision Grinding Performance*. International Journal of Machine Tools Manufacture (51) 411-419.
48. Yan, L. Rong, Y. M. Feng, J. and Zhi, X. Z., (2011), *Three-dimension Surface Characterization of Grinding Wheel using White Light Interferometer*. The International Journal of Advanced Manufacturing Technology. (55) 133-141.
49. Zhang, X. Xu, H. and Fu, Y., (2006), *Measurement Technique of Grinding Wheel Topography based on Binocular Stereo Vision*. Materials Science Forum. (532) 1132-1135.
50. Gong, Y. D. Wang, B. and Wang, W. S., (2002), *The Simulation of Grinding Wheels and Ground Surface Roughness based on Virtual Reality Technology*. Journal of Materials Processing Technology. (129) 123-126.
51. Nguyen, T. A. and Butler, D. L., (2005), *Simulation of Surface Grinding Process, part 2: Interaction of the Abrasive Grain with the Workpiece*. International Journal of Machine Tools and Manufacture. (45) 1329-1336.
52. Zhang, L. C. Suto, T. Noguchi, H. and Waida, T., (1993), *Applied Mechanics in Grinding-III. A New Formula for Contact Length Prediction and a Comparison of Available Models*. International Journal of Machine Tools and Manufacture. (33) 587-597.
53. Qi, H. S. Mills, B. and Xu, X. P., (2009), *Applications of Contact Length Models in Grinding Processes*. Key Engineering Materials. (404) 113-122.
54. Qi, H. S. Mills, B. and Rowe, W. B., (1994), *Analysis of Real Contact Length in Abrasive Machining Processes using Contact Mechanics*. Wear. (176) 137-141.

55. Pombo, I. Sanchez, J. A. Ortega, N. Marquinez, J. I. Izquierdo, B. and Plaza, S., (2011), *Contact Length Estimation in Grinding using Thermocouple Measurement and Numerical Simulation*. International Journal of Advanced Manufacturing Technology. (59) 83-91.
56. Brough, D. Bell, W. F. and Rowe, W. B., (1983), *A Re-examination of the Uncut Chip Model of Grinding and its Practical Implications*. In Proceedings of the Twenty Fourth International Machine Tool Design and Research Conference. 261.
57. Reichenbach, G. S. Mayer, J. E. Kalpakcioglu, S. and Shaw, M. C., (1956), *Role of Chip Thickness in Grinding*. American Society of Mechanical Engineers-Transactions. (78) 847-859.
58. Zhang, Y. Gao, Y. and You, J., (2010), *A Study of Uncut Chips Produced by CNT Grinding Wheel*. Advanced Materials Research. (126) 879-884.
59. Brecker, M. C. and Shaw, J. N., (1974), *Measurement of the Effective Number of Cutting Points in the Surface of a Grinding Wheel*. In: Proceedings of the International Conference on Production Engineering. 740-745.
60. Kim, C. Park, S. Yang, M. Y., (1995), *Verification of NC Tool Path and Manual and Automatic Editing of NC Code*. International Journal of Production Research. (33) 659-673.
61. Warkentin A., (1997), *Multi-Point Machining of Sculpture Surfaces*. Waterloo, Ontario, Canada.
62. Torrance, A. A. and Badger, J. A, (2000), *The Relation between the Traverse Dressing of vitrified Grinding Wheels and their Performance*. International Journal of Machine Tools and Manufacture. 40(12), pp. 1787-1811.
63. Cooper, W. L. Lavine, A. S., (2000), *Grinding Process Size Effect and Kinematics Numerical Analysis*. Journal of Manufacturing Science and Engineering. (122) 59-69.
64. Warnecke, G. and Zitt, U., (1998), *Kinematic Simulation for Analyzing and Predicting High-performance Grinding Processes*. CIRP Annals Manufacturing Technology. (47) 265-270.

65. Molesini, G. Pedrini, G. Poggi, P. and Quercioli, F., (1984), *Focus-Wavelength Encoded Optical Profilometer*. Optics Communications. (49) 229-233.
66. Malkin, S. and Murray, T., (1977), *Comparison of Single Point and Rotary Dressing of Grinding Wheels*. 5th North American Metalworking Research Conf. 278-283.
67. Malkin, S. and Cook, N. H., (1971), *The Wear of Grinding Wheels, part 2-Fracture Wear*. J. Engng Ind. Trans. ASME. (93) 1129-1133.
68. Pande, S. J. Lal, G. K., (1979), *Effect of Dressing on Grinding Wheel Performance*. International Journal of Machine Tool Design Research. (19) 171-179.